FINITE ELEMENT MODELING OF THE FRICTION STIR FORMING PROCESS

A DISSERTATION SUBMITTED TO THE DEPARTMENT OF MECHANICAL ENGINEERING OF THE UNIVERSITY OF HAWAI‘I AT MĀNOA IN PARTIAL FULFILLMENT FOR DEGREE OF

DOCTOR OF PHILOSOPHY
IN
MECHANICAL ENGINEERING

July 25, 2016

By
Sladjan Lazarevic

Comprehensive Examination Committee:
Dr. Scott F. Miller,
Chairperson
Dr. Jingjing Li
Dr. Blair Carlson
Dr. Lloyd H. Hihara
Dr. Eric Hellebrand

Key words: Friction Stir Forming,
Dissimilar Materials, FEA Modeling

We certify that we have read this document and that, in our opinion, it is satisfactory in scope and quality as a comprehensive report of Doctor of Philosophy in mechanical engineering.

COMMITTEE

Chairperson:

DEDICATION

To My Parents

ACKNOWLEDGEMENTS

I would like to thank my family and my friends for their support in this endeavor. In particular, I would like to recognize my parents Nikola and Mirijana Lazarevic and my wife Monica for their unlimited love, kindness, patience, and sleepless nights.

I would like to thank Dr. Blair E. Carlson for his support and patience through this research at the University of Hawaii as well as at General Motors, Prof. Dr. Lloyd Hihara for his support and understanding, and Prof. Dr. Eric Hellebrand for his great academic support.

I would also like to thank the Institute for Astronomy at Manoa for giving me academic and working opportunities.

Finally, I would like to express my deepest appreciation to Dr. Scott F. Miller for his support, kindness, patience, and mentorship. Working with you all has been an ideal and most rewarding learning experience.

ABSTRACT

This research is focused on developing the process that joins lightweight dissimilar materials with the maximum strength conceivable and with a minimum brittle intermetallic-formed region. It is difficult to weld these materials together because the properties of the dissimilar materials are usually prominently different.

Friction Stir Forming process can achieve this objective, and it can overcome the current challenges that other processes are facing in a cheaper way without using rivets, bolts, fluids, substantial energy for heating, or additional mass additions. This process can achieve the objective by stir heating one sheet and forming it into a pre-punched or pre-drilled hole in the second sheet. The result is forming a mechanical interlocking joint with minimal mechanical force by using relatively simple machinery and simple techniques. The first part of this research was focused on exploring the feasibility of concept and finding the optimal values of the important parameters such as spindle and plunge speed, torque, geometrical dimensions of the tools, etc. This experimental step gathered necessary data in order to set up a foundation for the following finite element analysis (FEA) work.

For the rest of the research, Abaqus software was used to accomplish the FEA task together with a validation experiment. As a product of the modeling segment, predictions can be accurately and easily determined for different conditions, shapes, and materials. This will allow further understanding of the potentials of the technology, and it will facilitate an expansion of this new valuable technology.

The research outcomes highlighted materials behavior during the FSF process, the major challenges for an accurate FEA model, and temperature distribution of the work materials. The research also identified opportunities for further research.

TABLE OF CONTENTS

DEDICATION .... **iii**

ACKNOWLEDGEMENTS .... **iv**

ABSTRACT .... **v**

TABLE OF CONTENTS .... **vi**

LIST OF FIGURES .... **viii**

LIST OF TABLES .... **ix**

1. Introduction *1*
1.1. Friction stir forming process *1*
1.2. Motivation *2*
1.3. Literature Review *4*
1.4. Research Issues *7*
1.4.1. Experimental Analysis Challenges *7*
1.4.2. Modeling Challenges *7*
2. FSF Joints Elements and Experimental Setup *9*
2.1. Joint Design *10*
2.1.1. Single Pin Design *10*
2.1.2. Clinching Design *12*
3. Experimental Setup *14*
3.1. Machine Setup *14*
3.2. Tool and Anvil *15*
3.3. Thermocouples Temperature Measurement Setup *16*
3.4. Infrared Camera Temperature Measurement Setup *17*
3.5. Sample Preparation *18*
3.6. Clinching design and materials *19*
4. Experimental Outcomes *20*
4.1. Single Pin Depth Test *20*
4.2. Clinching Experimental Results *23*
4.3. Special Interest Areas *25*
4.3.1. Head *25*
4.3.2. Neck *26*
4.3.3. Aluminum Separation and Brazed Joint *26*
4.3.4. Thermo-mechanically affected zone *28*
4.3.5. Aluminum Cavity Edge *29*
4.3.6. Flash *29*
4.4. Temperature Analysis *30*
4.4.1. Thermocouple Temperature Measurement Results *30*
5. Finite Element Analysis *32*
5.1. Background Information *32*
5.1.1. Johnson-Cook Plasticity Model and Heat Generation *33*
5.1.2. Stick - Slip Condition *36*
5.2. Two Dimensional Model and Submodels *37*
5.3. 2D Results *43*
5.3.1. Global Model Results *43*
5.3.1.1. Temperature *44*
5.3.1.2. Heat Flux *45*
5.3.1.3. Stress *46*

5.3.2. Submodels 47
5.3.2.1. Aluminum Detachment 48
5.3.2.2. Thermo-Mechanically Affected Zone and Heat-Affected Deformation Zone 49
5.3.2.3. Temperature Results from the Submodels 50
5.3.2.4. Stress 52
5.3.3. Conclusions 53
5.4. 3D Model 55
5.5. Boundary Conditions and Interactions of the 3D Model 58
5.6. 3D Results 61
5.6.1. Global Model Results 61
5.6.1.1. Head and Neck 61
5.6.1.2. Flash and Aluminum Detachment 62
5.6.1.3. Separation after the Contact 63
5.6.1.4. Steel Behavior 65
5.6.1.5. Temperature and Plastic Strain Distribution 67
5.6.2. 3D Submodels 70
5.6.2.1. 3D Submodel I 70
5.6.2.2. 3D Submodel II 72
5.6.3. 3D Modeling Conclusions 74
5.7. Modeling Improvements 77
5.7.1. Meshing Improvements 77
5.7.2. Zinc Layer 78
5.7.3. Deformable Domains 78
5.7.4. Parameters to Improve 79
6. Experimental Validation 80
6.1. Infrared Camera Test 80
7. Conclusions and Future Work 83
7.1. Conclusions 83
7.1.1. Thermal analysis 83
7.1.2. Depth Tests 84
7.1.3. 2D Model 85
7.1.4. 3D Model 85
7.1.5. Validation Experiments 87
7.2. Future work 87
7.2.1. Modeling Improvements 87
7.2.2. Tensile test 88
7.2.3. Clinching Model 88
8. Contributions of this research 91
9. Acknowledgment 92
10. Works Cited 93

LIST OF FIGURES

FIGURE 1: THE FSF SINGLE PIN STAGES ... 9
FIGURE 2: FSF JOINT ELEMENTS ... 10
FIGURE 3: THE FSF CLINCHING STAGES. ... 12
FIGURE 4: SET-UP OF FSF EXPERIMENTS ... 14
FIGURE 5: THE FRICTION STIR SPOT WELDING MACHINE ... 15
FIGURE 6: FSF COMPONENTS ... 15
FIGURE 7: THREE POINTS FOR THE THERMAL EXPERIMENTATION ... 16
FIGURE 8: INFRARED CAMERA SETUP ... 17
FIGURE 9: CLINCHING DESIGN ... 19
FIGURE 10: MATERIAL PROGRESSION AT THE DIFFERENT DEPTS. ... 21
FIGURE 11: ALUMINUM DETACHMENT FROM THE BOTTOM WORKPIECE AND ZINC ACCUMULATION (BSE IMAGES) ... 22
FIGURE 12: ZINC AND THE STEEL-ALUMINUM CONTACT IN A SINGLE PIN SAMPLE ... 22
FIGURE 13: OPTICAL AND SEM PICTURES OF A FSF SAMPLE THAT HAS STEEL AS TOP MATERIAL ... 24
FIGURE 14: A LINE-SCAN RESULT OF THE MIDDLE LAYER ... 24
FIGURE 15: MODELING SPECIAL INTEREST AREAS ... 25
FIGURE 16: ALUMINUM PEELING FAILURE ... 27
FIGURE 17: BOTTOM COIN SURFACE (THE BRAZED JOINT) ... 28
FIGURE 18: THERMAL PROFILE FOR THE 3 POINTS ... 30
FIGURE 19: ABAQUS NAMING CONVENTION ... 37
FIGURE 20: SCHEMATICS OF A SINGLE PIN FSF SAMPLE ... 38
FIGURE 21: 2D MODEL ... 40
FIGURE 22: ASSEMBLED 2D GLOBAL MODEL WITH BOUNDARY CONDITIONS AND SURFACE HEAT FLUX. 42
FIGURE 23: 2D SUBMODELS ... 42
FIGURE 24: TEMPERATURE DISTRIBUTION OF THE GLOBAL 2D MODEL ... 45
FIGURE 25: HEAT FLUX VECTORS ... 46
FIGURE 26: STRESS DISTRIBUTION IN THE GLOBAL 2D MODEL. ... 47
FIGURE 27: ALUMINUM DETACHMENT ... 48
FIGURE 28: THERMO-MECHANICALLY AFFECTED ZONE PREDICTION ... 49
FIGURE 29: TEMPERATURE PROFILE FOR THE FIRST SUBMODEL ... 50
FIGURE 30: TEMPERATURE PROFILE FOR THE FIRST SUBMODEL ... 51
FIGURE 31: STRESS PROFILE FOR THE FIRST SUBMODEL AT 0.3, 0.6, AND 0.9 MM OF PLUNGE DEPTH ... 52
FIGURE 32: STRESS PROFILE FOR THE SECOND SUBMODEL AT 0.3, 0.6, AND 0.9 MM OF PLUNGE DEPTH .. 53
FIGURE 33: 3D MODEL (A SCHEMATIC REPRESENTATION AND A CROSS-SECTION) ... 56
FIGURE 34: ALUMINUM DOMAIN MESHING ... 56
FIGURE 35: MESHING OF THE DOMAINS ... 57
FIGURE 36: BOUNDARY CONDITIONS AND A COUPLE OF CONTACT PAIRS ... 59
FIGURE 37: HEAD PROGRESSION ... 61
FIGURE 38: DISTORTION OF THE MESH IN THE NECK REGION ... 62
FIGURE 39: ALUMINUM DETACHMENT AND FLASH AT 0.8 MM PLUNGE DEPTH ... 62
FIGURE 40: SHAPE OF THE ALUMINUM DETACHMENT ... 63
FIGURE 41: TEMPERATURE DISTRIBUTION (NO SEPARATION AFTER THE CONTACT) ... 63
FIGURE 42: NECK AND HEAD (WITH NO CONTACT AFTER THE SEPARATION) ... 64
FIGURE 43: NECK AND HEAD AT 0.8 MM PLUNGE DEPTH (WITH "SEPARATION AFTER THE CONTACT") .. 64
FIGURE 44: STEEL DEFORMATION AND STRESS DISTRIBUTION AT 0.9 MM PLUNGE DEPTH ... 65
FIGURE 45: PRESSURE PROFILE FOR ALUMINUM AND STEEL ... 66
FIGURE 46: BOTTOM VIEW OF THE STEEL COLLAPSE AND THE ALUMINUM HEAD ... 66
FIGURE 47: TEMPERATURE DISTRIBUTION OF THE STEEL AND ALUMINUM (ENLARGED CONTACT CONDUCTIVITY) ... 67
FIGURE 48: TEMPERATURE DISTRIBUTION OF STEEL (ENLARGED CONTACT CONDUCTIVITY) ... 67
FIGURE 49: TEMPERATURE DISTRIBUTION OF THE ALUMINUM AND THE STEEL ... 68
FIGURE 50: PLASTIC STRAIN OF THE ALUMINUM AND THE STEEL ... 68

FIGURE 51: STRESS IN THE WORK MATERIALS AT 0.8 MM PLUNGE DEPTH 69
FIGURE 52: DISPLACEMENT IN STEEL AT 0.8 MM PLUNGE DEPTH 69
FIGURE 53: DISPLACEMENT IN ALUMINUM AT 0.8 MM PLUNGE DEPTH 70
FIGURE 54: 3D SUBMODEL I – A TOP VIEW (MATERIAL PROGRESSION AND TEMPERATURE DISTRIBUTION) 71
FIGURE 55: 3D SUBMODEL I – A BOTTOM VIEW AND A VIEW OF THE HEAD AT 0.8 MM PLUNGE DEPTH (TEMPERATURE DISTRIBUTION) 71
FIGURE 56: 3D SUBMODEL I – CROSS SECTION AT 0.8 MM DEPTH (HEAT FLUX AND PRINCIPLE PLASTIC STRAIN) 72
FIGURE 57: 3D SUBMODEL II – TOP SURFACE (TEMPERATURE DISTRIBUTION) 72
FIGURE 58: 3D SUBMODEL II – A BOTTOM AND A CROSS-SECTION VIEW (TEMPERATURE DISTRIBUTION) 73
FIGURE 59: 3D SUBMODEL II – CROSS-SECTION (HEAT FLUX AND PRINCIPLE PLASTIC STRAIN) 73
FIGURE 60: ALUMINUM MESH WITH ADDITIONAL SEGMENTATION 77
FIGURE 61: THERMAL PROFILE GIVEN BY THE INFRARED CAMERA 80
FIGURE 62: CLINCHING JOINT ASSEMBLY 89

LIST OF TABLES

TABLE 1: PARAMETERS FOR FRICTION STIR CLINCHING PROCESS 19
TABLE 2: JOHNSON-COOK PARAMETERS FOR AA6061-T6 [SELI 2012] 33
TABLE 3: TEMPERATURE-DEPENDENT MATERIAL PROPERTIES FOR AA 6061-T6 [SOUNDARARAJAN 2005] 34
TABLE 4: COEFFICIENT OF FRICTION DEPENDENCY ON TEMPERATURE [SELI 2012] 35
TABLE 5: 2D DOMAINS AND THEIR DIMENSIONS 39
TABLE 6: 3D DOMAINS AND THEIR DIMENSIONS 39
TABLE 7: STEEL PROPERTIES 39
TABLE 8: MESH CHARACTERISTICS OF THE 3D MODEL 57
TABLE 9: MESH CHARACTERISTICS OF THE 3D SUBMODEL 57
TABLE 10: MILD STEEL PROPERTIES USED IN THE 3D SIMULATION [MOUSAVI 2008] 58
TABLE 11: JOHNSON-COOK CONSTRAINS FOR MILD STEEL [MOUSAVI 2008] 65
TABLE 12: TEMPERATURE OF THE MODELS AND SUBMODELS AT 0.8 MM PLUNGE DEPTH 81

1. Introduction

Joining dissimilar materials represents a significant challenge, which is especially obvious in the transportation industry. For example, it is difficult to weld aluminum alloy and steel sheets together since their properties are significantly dissimilar. Aluminum alloys melt around 600-660ºC, but at that temperature, steel is not even in the austenite region. It is desirable in the industry to develop new joining processes for aluminum alloy and steel sheets [Mori et al., 2006]. The critical problem is that joint strength from traditional joining methods such as fusion processes is limited in dissimilar metal joint applications by the formation of brittle intermetallic compounds at the joint interface due to mutual diffusion during the joining procedure.

Traditionally, the joining was done by various types of fasteners such as rivets and bolts. This is less desirable because the fasteners increase the total mass, and consequently that means higher fuel consumption. On the other hand, there is also an impetus that the substitute joining process needs to be environmentally friendly with less or no chips, fumes, weld wire, additional fluid, or any other by-products. Friction Stir Forming (FSF) is a new and environmentally friendly process that was developed to satisfy those two criteria. In this process, a modified friction stir welding (FSW) tool is plunged into the top workpiece, simultaneously frictionally heating, stirring, and forming it into a new shape. Through heating one sheet and forming it into a prefabricated hole in the second sheet, the formation of unwanted brittle intermetallics could possibly be reduced, or completely avoided. Therefore, it saves on mass and cost. It is environmentally friendly because there are no unwanted fumes, unsightly soot, shielding gas, spatter, or ultraviolet light. Thus, there is no need for a fume exhaust system either, and it is a relatively quiet process.

1.1. Friction stir forming process

FSF is a new and environmentally friendly process for joining dissimilar materials. In the process, a modified FSW tool is plunged into the top workpiece, simultaneously frictionally heating, stirring, and forming it into a new shape. The new shape has many possible applications. Although this is possibly true for variety combinations such as a polymer and magnesium, the major application studied in this research is a mechanical joint between two common dissimilar workpieces, aluminum and steel.

There are significant differences between FSF and the other friction processes. In FSW, the tool plunges into two workpieces in butt joint configuration, and after the work material around and under the tool/shoulder is fully plasticized, the tool moves along the joint line of the work-pieces at a constant speed. The material that is in front of the rotating tool pin is plastically deformed and stirred back to the trailing edge of the tool pin. In friction stir spot welding, the tool stirs the top work material, and then the stirring phase mixes the materials. In friction stir drilling, as the tool plunges, the material is pushed out of the way of the stirring tool with the support of heat from friction in order to make a hole in the metal sheet. There are other significant differences between the methods such as tool geometry, tool size, etc. However, the fundamental principles of those friction stir processes are applicable for FSF.

Through heating one sheet and forming it into a prefabricated hole in the second sheet, the formation of brittle intermetallics can possibly be reduced. In addition, this process does not require rivets, bolts, weld wire, and additional fluid. Therefore, it saves on mass and cost. It is environmentally friendly because there are no fumes, unsightly soot, shielding gas, spatter, or ultraviolet light. There is no need for a fume exhaust system either, and it is a relatively quiet process.

1.2. Motivation

In this research the hypothesis is finite element analysis (FEA) modeling will give accurate prediction and information about the FSF process. Prior to this research, Nishihara et al., [2003] worked on a process for micro-forging and its application to mechanical fastening. They performed forming using different aluminum alloys in addition to cladding of a grooved steel plate with aluminum. Balakrishnan et al., [2007] successfully joined aluminum to nylon by a mechanical interlock formed by a FSW tool. Lazarevic et al., [2013] effectively joined lightweight dissimilar materials by FSF processes. The technical challenge centers on using friction stir processes to heat and form material instead of mixing it as in conventional FSW. There are numerous potential applications for the FSF process, especially in the transportation industry which employs lightweight aluminum structures. The trend in the industry is that the usage of aluminum and other dissimilar materials is increasing due to the forthcoming global environmental awareness and federal and state legislation. Therefore, the potential market is in the applications for automotive, aerospace, rail, and nautical vehicles.

In this study, the relationship between the process and joint structure for the new FSF process was measured and modeled. The nature of the work material forming at higher temperatures was characterized in the leading stage of this research. This solid state joining process was studied by experimental and material analyses. After the data collection, this research incorporated the modeling approach in order to improve further knowledge about how material forms and transforms during the joining procedure. This is useful and desirable since it can predict the behavior of different conditions and materials without expansive and time-consuming laboratory testing procedures. The FEA model was developed to predict the material progression and temperature distribution during the joining process based on tool progression.

Modeling is a required tool to understand the material flow, temperature distributions, stresses, and strains, which are difficult or even impossible to measure experimentally. The sudden temperature increase caused by the tooling changes material properties, as well as rapid cooling after the tool retracts. The thermo-mechanical FEA can give information that is impossible from the laboratory experiments. The depth test, temperature measurements, and spectroscopies (optical, energy-dispersive spectrometry, scanning electron microscope, and electron microprobe analysis) were done in order to collect the necessary data for the modeling step. The temperature measurements were necessary in order to have a temperature profile of the system. The depth test is an experiment that produces samples with different plunge depths. Upon metallurgical examination of the samples, researchers have the record of the material progression at the chosen tool stopping points. Previously, FEA has been applied to simulate similar processes such as FSW, friction stir spot welding (FSSW), and friction stir drilling. They rely on the same concept as FSF where a rotating tool plunges into the work material, generates frictional heat, and stirs material under and around the tool.

1.3. Literature Review

Joining dissimilar metals has been attempted; however, it is difficult to achieve a sound steel/aluminum joint by using fusion welding processes [Sun and Khaleel, 2007; Sun and Karppi, 1996; Pasic et al., 2007, Martinsen et al., 20015]. It is possible to weld dissimilar metals by diffusion bonding with significant shortcomings of high cost, time, and temperature [Kalpakjian and Schmid, 2008]. FSW of dissimilar materials has been studied, yet the problem of fusion and bonding between dissimilar materials perseveres [Murr et al., 2000; Chen and Kovacevic, 2004; Tanaka et al., 2009; Watanabe et al., 2005; Choi et al., 2011; Fazel-Najafabadi et al., 2010; Jana et al., 2010]. The major challenge in welding dissimilar metals is the fusion and bonding, which could be circumvented with the FSF joining technique. The research indicates that joining materials by fusion or stir welding becomes more difficult as they become more dissimilar, i.e., their composition, thermal and mechanical properties diverge; the preliminary results for FSF joining suggests that this process becomes easier as the materials become increasingly different, and a mechanical interlocking joint can be formed with relatively simple machinery and techniques. Therefore, this is one of the major strengths of the new technology.

The potential of the FSF joining method was experimentally validated by using mild steel and aluminum [Lazarevic et al., 2013; 2015]. In the study, it was determined that the effect of key process parameters on the resulting joint strength quantify the effects of tool diameter, tool plunge depth into the aluminum work material, and anvil cavity depth on lap shear joint strength. This was accompanied with the profile of the axial force and torque, elementary stages, material progression, zinc/brazed layer characteristics, optimal tool set, an optimal design, elements of the joint, and principal challenges. The interface between the work materials aluminum and steel (coated with zinc) in a FSF joint was also investigated.

The FEA approach has been used for a variety of friction processes, because the technique improves the information of the process that otherwise cannot be done in an experimental way. FSW is the first friction stir process that was invented in 1991 by The Welding Institute, UK. In this process, the first primary stage contains a rotating tool that is plunged into two clamped workpieces. The friction heat causes a plasticized zone to form around the tool. Then, in the second stage, the rotating tool moves along the joint side, and the plasticized zone follows the tool. There is in-depth knowledge of the fundamental science that underlies the process, and that reflects the modeling aspect. The central part of the modeling has been thermal prediction since the earliest days of the method. There are numerous models developed that use ABAQUS/Explicit software package, and that addresses different aspects of the joining technology. For example, a model was developed that matches the heat generation experimental data well [Veljić et al., 2013]. For the experimental part, the researcher used an infrared camera to gather data for joining aluminum alloy 2024-T3. For the modeling part, ABAQUS/Explicit software was used to predict heat generation during the plunge stage. The model contained the Johnson-Cook material law and Coulomb's law of friction. Next, a Johnson-Cook model was used in the same FEA software to validate the experimental results of the friction stir welding process for the 4340 steel and mild steel combinations [Akbari et al., 2008]. As FSW comprises complex phenomena involving many interrelated mechanisms and thermal processes, it is clear that a complete characterization of joint behavior is impossible. Accurate and reliable numerical analysis of the FSW is still a very difficult task as the behavior of the FSW joints is influenced by different factors in combination [Hea et al., 2014].

Friction stir spot welding is the next solid state joining technology in line. In this technology, the rotating pin of the tool plunges into the top workpiece. After the pin has plunged completely into the workpiece, the tool continues to spin and apply pressure to the joint. At this period of time, the materials around the pin are stirred together, and the two lapped plates are joined in the area surrounding the pin. For this purpose, a thermo-mechanical modeling of the process was developed [Awang et al., 2005]. In the model, the tool and the flat backing anvil are modeled as isothermal analytical rigid domains. The workpieces were meshed with C3D8RT element, which is a thermo-mechanical 8-node tri-linear displacement element type with reduced integration and glass control. The material of the workpieces was aluminum 6061-T6 and the thickness was 1 mm. The model also assumed Coulomb's friction law and temperature dependent friction coefficient.

Next in the invention line is friction stir drilling. This method is used to create a bushing on sheet metal, tubing, or thin walled profiles for joining devices in a simple and efficient way. The heat generated from friction between a rotating conical tool and the workpiece is used to soften the work material while the conical tool penetrates the workpiece. As a result, a hole was made in a simple and efficient way. There is a successful model that demonstrated distribution of plastic strain, temperature, and von-Mises stress of the friction drilling process by using adaptive meshing, element deletion, and mass scaling in ABAQUS/Explicit [Miller et al., 2007]. The material used in the study was also aluminum 6061-T6.

There are other important instances for friction welding. For example, the same software package was used to model friction welding of aluminum to mild steel rods with use of an Al6061 sheet [Seli et al., 2012]. The Arbitrary Lagrangian-Eulerian approach was applied together with a Johnson-Cook plasticity model and adaptive meshing. All three domains had a C3D8RT mesh element type incorporated.

Other researchers have successfully used other software packages for modeling friction stir processes as well. ANSYS is a commercial software package that is well suited for the predictions. This software was used to calculate temperature evolution in 304 L stainless steel during FSW [Prasanna et al., 2010]. A thermal model was developed with COMSOL Multiphysics commercial software package to predict the temperatures during FSW of 5083-H116 aluminum alloy and pure copper [Roubaiy et al., 2015]. Another thermo-mechanical model was developed in order to understand the variation of coefficient of friction between a high strength steel tool with a base metal of 6061-T6 aluminum alloy in FSW. This was done with COMSOL Multiphysics software as well [Tanmoy et al., 2015]. During FSW, the edge between the shoulder and the pin of the tool develops a large amount of stress that can lead to tool defects or failure. A simulation was developed to ensure that the tool is able to withstand tremendous load during the process. This task was carried out using CATIA V5 software [Jaffarullah et al., 2015]. DEFORM 3D is another software package that is used for the FSW process. In Gök and Aydin's 2013 study, the software was used for simulating the FSW process on AZ31 magnesium alloy. The simulation performed with different rotational and traverse speeds, and it has been validated against experimental data.

1.4. Research Issues

This study aims to provide a deeper understanding of the FSF process that is currently missing. The major issues anticipated in the realization of research goals can be separated into two different categories: experimental and modeling issues.

1.4.1. Experimental Analysis Challenges

The research issues addressed by the experimental part are that FSF parameters are not well known, and there is a lack of fundamental understanding of the process and any correlation to intrinsic material characteristics. The deformation and material flow during the process are significant and they need to be fully characterized. Experiments have been conducted to measure different forces, temperature, and the nature of deformation for better understanding of the process. This was partially conducted at General Motors and the rest has been done at the University of Hawaii at Manoa, Mechanical Engineering department. The goal of the experimental part of the research was to maximize the knowledge of the process as a precursor for the simulation step.

1.4.2. Modeling Challenges

The hypothesis is that FEA will give an accurate theoretical prediction of the materials behavior during the FSF process. The ultimate goal for the modeling part of this research is to develop an FEA model that can accurately describe and predict the material behavior during the FSF procedure. However, it is difficult to develop an accurate FSF numerical model primarily because large work-material deformations cause problems with simulation convergence and completion. As can be seen in the experimental data that was gathered for the simulation, discussed in Chapter 4, prior knowledge about the fundamentals of the process such as appropriate tool size and design, optimal dimensions of the workpieces, and temperature distribution is not currently available. Another piece of important information that is currently missing is the most appropriate design for a given set of materials. That includes the design of FSF equipment, tools, and design of the through-hole in the bottom workpiece. When it comes to the design of the hole, the information that is needed is about the position in relation to the tool and anvil axes, number, appropriate size a.k.a. diameter of the hole, and shape i.e. conical or cylindrical. With proper modeling techniques, the situation can be profoundly changed. Some of the major obstacles to that goal are shortly described in the following paragraph.

The quality of the mesh is critically important for any model since the accuracy of the model depends on the reliability of the mesh. This is especially the case in FSF because of the huge plastic deformation rate. This reliability of the mesh frequently depends on the quality of the partitioning as well. Some of the key components of mesh that needs to be carefully chosen are mesh element, size of the elements, orientation, curvature control, distortion control, etc. A mesh element type is based on what kind of a process is needed to be simulated. For a nonlinear simulation, an appropriate plasticity model needs to be incorporated so the simulation of the material progression follows the experimental outcomes. Contact between two or more domains is a discontinuous form of nonlinearity, and requires special algorithms such as contact pairs and general contact to couple stress, temperature, pressure, and friction. Boundary conditions have to be correctly specified for the values such as displacements, rotations, and temperatures at a particular set of nodes. Since this is a large nonlinear simulation, the work material undergoes enormous deformations, and these deformations distort the finite element mesh to the point where the mesh is unable to provide accurate results and the analysis terminates for numerous reasons. It is necessary to use adaptive meshing or a distortion control tool to minimize the mesh distortion. Computational time is an important factor that deeply affects modeling since there is a constant need to lower the cost. There are many other important challenges such as transferring the results between the modeling steps and the effects of material bonding.

In the modeling chapters, Chapter 5 and 6, there is a description of a finite element model developed by using ABAQUS/Explicit software.

2. FSF Joints Elements and Experimental Setup

The purpose of this study was to develop a basic understanding of the process-structure property relationship by first investigating various tool designs complimented by subsequent process parameter investigations. Then, the temperature-profiling test and depth tests were done. These were accomplished in order to grasp the necessary understanding of the materials transformation that is needed for the modeling segment of the research. The FSF procedure steps sequence is represented in **Figure 1**. The concept of this process is stir heating one material and forming it into a prefabricated hole within the second material.

Figure 1 a) shows the setup at the beginning of the process with the tool rotating and the workpieces in an overlapping position above the backing anvil, which contains a cavity for the eventual head of the interlocking joint. Then, as shown in **Figure 1** b), the rotating tool plunges into the top workpiece, which generates frictional heat, thereby lowering the work material yield strength. This facilitates extrusion of the aluminum through the prefabricated hole in the steel workpiece forming the neck and the head of the mechanically interlocking joint. **Figure 1** c) shows the last step, which is the tool and anvil dissociation from the joined materials.

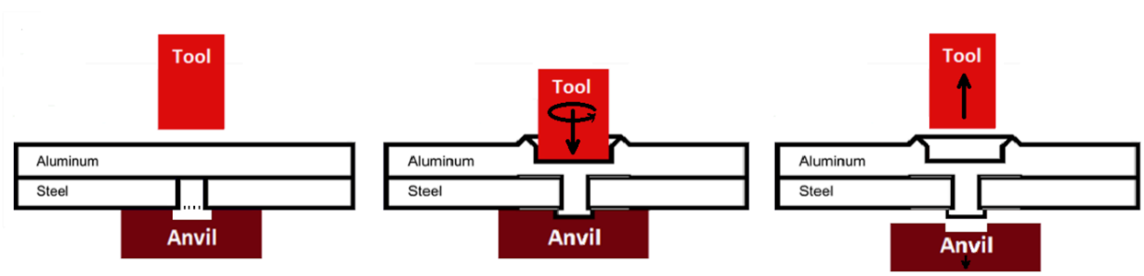

(a) Preparation (b) Tooling (c) Retracting

Figure 1: The FSF single pin stages

This is a schematic representation of the preparation, the stirring, and the final stage of the joining procedure.

2.1. Joint Design

One goal of this research is to find a joint design that yields the highest strength possible. At this time, there are two designs represented: single pin and clinching design. Single pin is the most explored design and is the design that the FEA model was based on. The other design is the alternative design. This alternative design shows some advantages and they will be described in the experimental part of the manuscript.

2.1.1. Single Pin Design

The most explored design is a sample having a single neck i.e. pin which is the material within the pre-fabricated hole in the bottom sheet and connecting the top sheet to the newly formed head on the opposite of the pin. The goal is to optimize the joint toughness through the geometrical and design parameters.

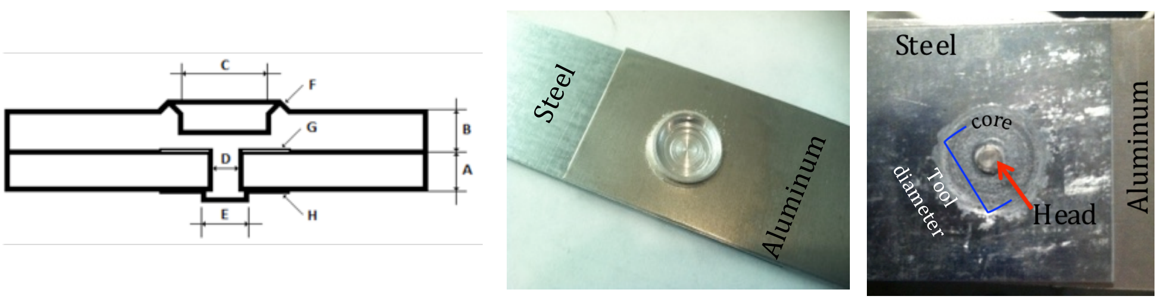

(a) Schematic view of a sample (b) Top view (c) Bottom view

Figure 2: FSF joint elements

This is a schematic view of a sample joint cross-section where A - steel coupon, B - aluminum coupon, C - shoulder diameter, D - neck diameter, E - head diameter, F – flash i.e. upsetting of top surface, G – brazed joint, and H – core i.e. bottom surface of joint. (b) It is a top view of the joint exhibiting the indention made by the tool shoulder surrounded by a thin ring of flash. (c) The bottom view of a sample with core and head exposed. The red arrow shows the aluminum head and the blue parenthesis show the diameter of the tool.

Every specimen made by the FSF process contains the elements presented in **Figure 2** a). The following is a detailed description of these elements starting from the top surface. When the shoulder of the rotating tool contacts the upper sheet surface, friction generates heat, thereby raising the temperature of the upper sheet and reducing the force level required to form the material. This frictional heat is also a significant factor affecting the temperature at the interface and consequently, the formation of any intermetallic interlayer.

As the tool advances into the upper sheet, the bottom surface of the upper sheet begins to fill the prefabricated hole with a neck diameter on the bottom sheet. Since there is a limited constraint on the top surface of the upper sheet adjacent to the rotating tool, flash will form as the tool advances into the top sheet, which is an undesirable vertical upsetting of the top work material.

Continued advance of the rotating tool will forge the upper sheet into the cavity machined into the anvil beneath the bottom sheet. There is frictional interaction of the deforming upper sheet as it is being "extruded" into the anvil cavity thereby forming the head. The aluminum material is pushed through the pre-fabricated hole in the bottom steel sheet to make a mechanically interlocking joint. The neck should carry as much of the load as possible in the interlocked specimens. Therefore, increasing the diameter potentially would increase the joint strength.

During the procedure, the steel hole might deform and the deformation negatively affects the joint quality. This can be seen in many samples under an optical microscope since the deformation is usually too small for the naked eye. That can be minimized if the diameter of the hole in the steel to anvil cavity diameter ratio is correct. Ultimately, a good FEA model should give the optimal diameter ratio. In addition, since an improved design is needed, ultimately FEA should deliver the better design.

Figure 2 a) also shows the core and the fraying interface, H and G respectively. They both have the same diameter as the tool. If the steel is zinc coated, the applied force and frictional heat will melt the low melting point zinc, forming a brazed joint (G) at the fraying interface. The higher temperature causes the zinc from the protection layer to become more mobile, by providing the activation energy needed for zinc atomic diffusion. Furthermore, the applied force of the tool will act to "coin" the bottom surface of the steel sheet against the bottom die leaving a circular mark of diameter H, i.e. core, in the area directly beneath the upper rotating tool. This may also cause some of the zinc on the bottom surface of the steel to stick to the anvil. Surrounding the core is a heat-affected zone called the corona. Since the corona highly depends on the temperature, this phenomenon is not present in all samples. Thus, this is another potential FEA opportunity for improvement.

2.1.2. Clinching Design

A different FSF design is the clinching design. The name is usually associated with a mechanical joining method for sheet metal parts. This simple method is based on only the accurate movement of a punch into a die. Therefore, the worksheets are plastically deformed into a mechanical interlock. In FSF clinching, instead of the punching, the friction stir method is applied. The graphical representation of the process is shown in **Figure 3**. Contrary to the single pin design, the bottom workpiece for the clinching joint has a hole with a bigger diameter. Moreover, it is slightly bigger than the diameter of the tool. The anvil's design is different from the FSF anvil as well.

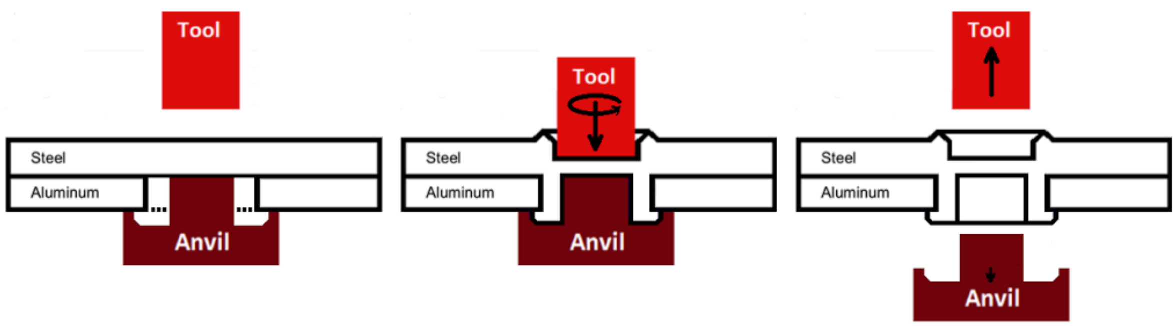

(a) Preparation (b) Tooling (c) Retracting

Figure 3: The FSF clinching stages.

This is a schematic representation of the preparation, the stirring, and the final stage of the joining procedure for the clinching design.

The top of the anvil has a circular canal that shapes the head. The middle of the anvil, the anvil pin, is elevated compared to the rest of the anvil. The difference between the top of the pin and the top of the anvil is equal to the bottom workpiece thickness. For the same size of the hole in the bottom workpiece, there will be a different value of the anvil pin diameter for different materials, and the following is an example when steel and aluminum alternates as the top workpiece material. When aluminum is the top workpiece, steel as the bottom, the aluminum makes the mechanical interlocking, and it is the weaker material. Therefore, there should be an appropriate amount of aluminum in the neck region so the top workpiece can overcome the weakness. On the other hand, when steel is on the top, as the tool moves down, steel as the stronger material will go towards the bottom of the anvil's canal. However, in that case, steel will also deform the aluminum laterally, and the hole of the bottom workpiece will expand. Consequently, dimensions of the anvil directly correspond to the material properties of the workpieces. The purpose for developing the new joint design is to improve the strength of the joint.

For a comparison, the following is a description of the strength of the single pin with an assumption that the head properly formed, including proper steel hole/anvil hole diameter ratio. Strength of the single pin design relies on the brazed joint and the neck diameter, or on the neck diameter if it is a bare steel worksheet. If the neck has a bigger diameter, the mechanical interlock between the two coupons will have higher maximum strength and higher toughness. In the clinching design, the neck diameter is already bigger, and the area that the brazed joint occurs in the clinching design is minuscule at best.

It is important to mention material flexibility that comes with the clinching design. As was described so far, the single pin is a valuable solution when aluminum is the top work material, since the material is malleable. However, if a reverse of the materials were needed in an application, the single pin design would lead to a significantly higher heat generation because the steel requires a higher temperature for the process. This would lead to aluminum degradation, and ultimately to low joining quality or complete joint failure. The situation is different with the clinching design. The heat is still higher, but the degradation is avoidable.

3. Experimental Setup

This chapter gives a description of the machines and work materials used for the research. Components such as tool, anvil, thermocouples, and infrared camera are described in detail. Techniques and procedures of the material sample preparation are described as well.

3.1. Machine Setup

There were two different machines used for the experimentation. First, a CNC machining center was used (model: Bridgeport Discovery 308) with a max spindle speed of 6000 rpm. This CNC system is a position and speed-controlled machine. The spindle speed (2250 rpm) was kept constant. This machine can be seen on **Figure 4**.

(a) UHM CNC machine (b) A closer look of the set-up

Figure 4: Set-up of FSF experiments

In order to explore and adapt the FSF process that was developed on the CNC machine at the University of Hawai'i at Manoa, a second machine was used and that is the Tool-o-matic Friction Stir Spot Welding System at General Motors Technical Center, Warren MI. This machine is shown in **Figure 5**.

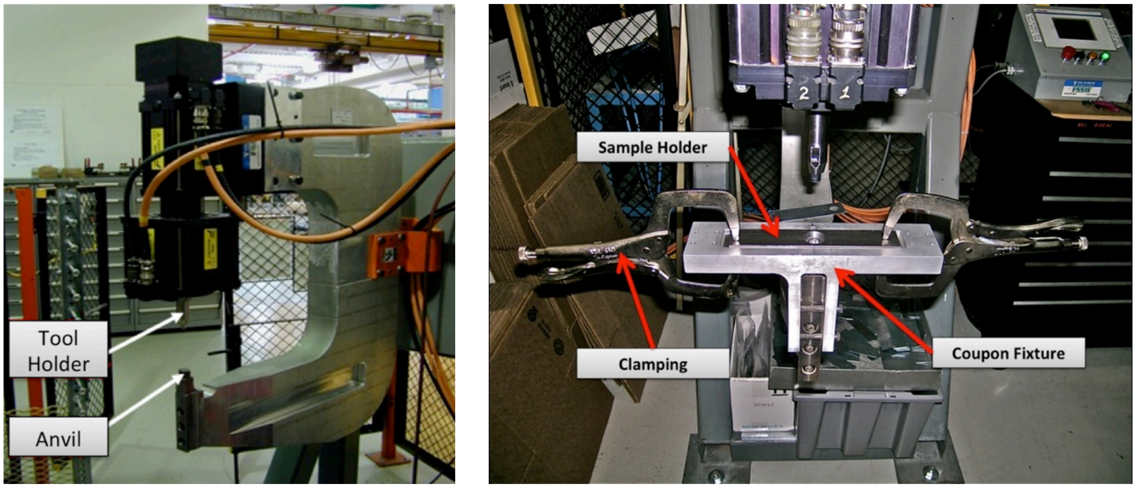

(a) A side view of the machine (b) The machine with workpiece in place for joining

Figure 5: The friction stir spot welding machine

3.2. Tool and Anvil

The non-consumable rotating tool is forced into the workpiece, and simultaneously creates frictional heat by stirring, softening the top work material, and directing the material flow. This thermo-mechanical input from the tool into a joint is supported by an anvil. The tool that was used for the procedure had a cylindrical shape. The tool was a pin-less tool (flat tool).

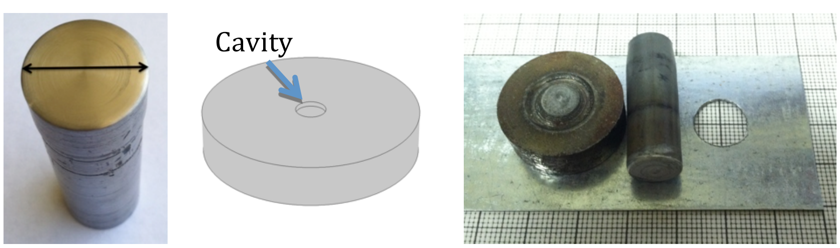

(a) Tool (b) Anvil (c) Tool, anvil, and bottom coupon

Figure 6: FSF components

On the left is the pinless tool that was used for the experimentation. The black arrows are placed on the face that touches the top piece, and they show the diameter of the tool. In the middle is a representation of the anvil for a single pin joint. The center of the topside of the part is the anvil's cavity. On the right is a clinching set. The anvil and the tool place are placed on the top of a steel workpiece with a pre-drilled hole.

The simple cylindrical shape has proven to work the best [Lazarevic et al., 2013]. Besides ultimately accepting all the force, torque, and heat that comes from the tool, the anvil and its cavity shapes the head. Both of the two parts of the equipment were made of A2 air hardening tool steel, and their shapes can be seen on **Figure 6**.

3.3. Thermocouples Temperature Measurement Setup

This part of the experiment had unique challenges such as the presence of the thermocouples in between the two worksheets increased the stickup and they could move with ease during the stirring. In addition, the thermocouples could be easily damaged or destroyed. For this experimentation, the Design of Experiment approach was used with three repetitions and three locations. There were measurements that needed to be redone since the thermocouples were damaged during the testing.

The first point, T1, was in the core of the joint. The second point, T2, was located on the edge of the core. The final third point, T3, was located on the edge of the corona as was presented on **Figure 7**. The distance between the two neighboring points was 2.5 mm, and they are all placed in a line on one side of the joint and between the top and bottom sheet.

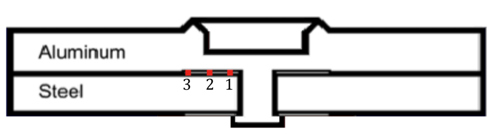

(a) Schematic representation of the locations (b) Optical view

Figure 7: Three points for the thermal experimentation

On the left is a schematic representation of a cross-section with the numbered red dots that are representing the three temperature examination points. On the right is an actual sample (only steel with the aluminum neck in-situ since the aluminum workpiece was peeled off for the examination).

The type K thermocouples were connected to DBK84, (14-channel low-noise, high-accuracy, thermocouple module) which was connected to a laptop. The data collected by the laptop was analyzed by Matlab, Microsoft Excel, and Minitab16 (the Design of Experiments software).

For the experiment, the following machine parameters were constant: flat tool with the diameter of 14 mm, spindle speed of 2000 rpm, and plunge speed of 1.0 mm/s. The parameters that were not constant through the thermal analysis part of the research were the aluminum 5182 coupon thickness (1.0 and 1.4 mm), and the plunge depth (0.5, 0.7, and 0.9 mm). This aluminum alloy, as all other member of 5000 series, contain magnesium as alloying element for solute hardening. It has a good combination of strength and formability in addition to good corrosion resistance.

3.4. Infrared Camera Temperature Measurement Setup

In order to get more temperature information of the process a FLIR A655sc infrared camera was used. This thermal infrared imaging camera has a uncooled microbolometer, field of view of 25° x 18.8°, and spatial resolution 0.69 mrad that produce a visual representation of the infrared energy emitted and reflected by all the objects in the setup. The temperature range of the instrument is 0°C to 650°C. The camera has an accuracy of ± 2°C or ± 2 % of reading.

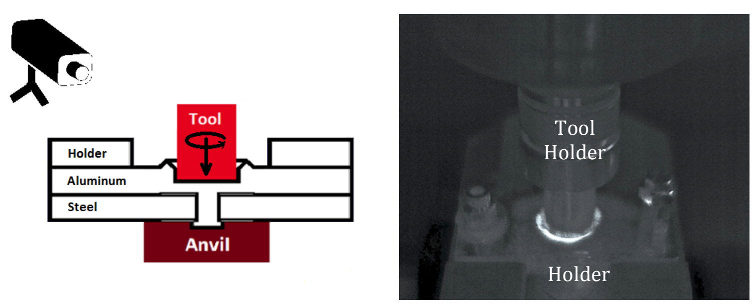

(a) Schematic representation (b) A fixed look through the IR camera

Figure 8: Infrared camera setup

On the left is a schematic representation of the camera setup. On the right is the view of the setup through the camera. At that moment, the tool was stirring and glow comes from the aluminum workpiece through the tool/holder gap.

For this experiment, 1.4 mm thick aluminum 6061 was used. The anvil had a cavity 0.6 mm deep and 3.8 mm in diameter. The machine parameters were the following: spindle speed of 2250 rpm, plunge speed 100 mm/min (1.67 mm/s), and the maximum plunge depth was 0.9 mm. The flat tool had a diameter of 10 mm. The room temperature during the experiment was 25°C.

All the coupons were 38 x 127 mm (1.5" x 5"). Throughout the entire experimentation, GMW2 0.7 mm thick steel was used. This steel is usually used in research and it has a zinc layer that provides a hardwearing surface and a good anticorrosive property. The zinc coating was made by the Hot Dipped Galvanizing process. These mild-steel coupons had a 3.0 mm hole drilled after the galvanization.

3.5. Sample Preparation

To study the experimental specimens, metallurgical samples were prepared in the standard metallurgical procedure. For the microscopic analyses the sample was cross-sectioned with a diamond saw. The cross-sectioning was done in such a way that the final polished side of the specimens would show the exact center of the joint. After they were mounted in epoxy and cured, the samples were ground and polished using silicon-carbide papers and emulsions of alumina with 1.0, 0.3, and 0.05 micron particle sizes. In order to reveal grain boundaries, structure, and flow patterns, the samples were etched and viewed under an optical microscope. Etching was accomplished using Keller's reagent (500 mL solution that was 2.5% HNO3, 1.5% HCl, and 1% HF), the standard for etching aluminum and aluminum alloys. The etched samples can be seen on **Figure 10**.

Scanning electron microscopy was also done. For that, the samples were also prepared in the standard metallurgical procedure. However, after the alumina polishing step, the samples were ultrasonically cleaned, oven dried, and carbon coated. Prior to the coating a single sided adhesive copper conducting tape was also applied on the surface in order to ensure a proper discharge from the specimens. The carbon coating was applied using a vacuum evaporator at pressures of less than 13.3 mPa ($1.33 \cdot 10^{-7}$ Bar). Carbon coating is used to improve imaging of samples and prevents charging on the specimens. In addition, there would not be any analytical confusion between carbon from the coating and any element from the specimens. Then, the samples were analyzed with the electron probe micro analyzer (EPMA). The accelerating voltage on the electron gun for the pictures was 20 kV.

3.6. Clinching design and materials

As was discussed in Section 2.1.2, this anvil design involved a pin protruding at the top and a circular cavity around the pin, and a schematic representation of the design can be seen on **Figure 9** as well. The height from the bottom of the cavity to the top of the pin was 2 mm and from the bottom of the cavity to the anvil surface was 0.6 mm. The pin protruded 1.4 mm because the thickness of the bottom aluminum sheet used in these experiments was 1.4 mm as well. The top of the pin had a diameter of 8 mm. The outer diameter of the circular canal was 14 mm. The machine parameters can be seen in **Table 1**. For this experiment, aluminum 5182 was used.

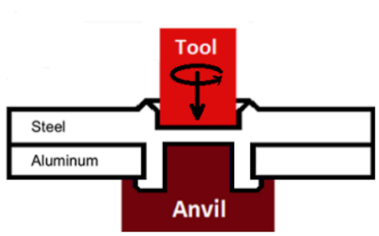

Figure 9: Clinching Design

Table 1: Parameters for Friction Stir Clinching Process

Parameter	Spindale Speed	Plunge Speed	Plunge Depth	Tool Diameter	Al Hole Diameter
Value	3000 rpm	5 mm/min	1.9 mm	11.074 mm	11.1125 mm

4. Experimental Outcomes

In order to develop a simulation, there is a necessary amount of data that needs to be collected beforehand. In this section, the data that was experimentally collected prior to the simulation step and the their significance are explained.

Here is an example of the contact property importance between the tool and the top workpiece. When the tool arrives at the surface of the top workpiece, the device starts to deliver mechanical energy into the system. One part of the energy is responsible for the deformation of the components, especially the top workpiece. The other part of the mechanical energy will be transformed into heat, and it will affect all the components of the system. In other words, the heat from the aluminum workpiece will be conducted to the holder, the steel coupon, the anvil, and into the surrounding environment. Therefore, in order to accurately capture the transformations, it is very important that all these contacts are defined in a proper way.

The experiments were focused to reveal the maximum possible information about the procedure and that includes aluminum and zinc progression, temperature, and steel deformation. In order to capture all the critical progressions, information was gathered on all the elements of the system: the steel coupon, the aluminum coupon, the pinless tool, and the anvil. The aluminum coupon is especially interesting, because the material undergoes major thermo-mechanical changes. For this reason, the research was focused on six special areas of interest, and section 4.3 describes the areas (head, neck, aluminum detachment, coin, tool rim, and flash). The information from the areas was especially directed and forced into the FEA model, so the model captures the material changes and the material progression in the most accurate way. Most of the information about the special interest area was gathered from the depth test, which is explained in the following text.

4.1. Single Pin Depth Test

The main purpose of the depth test was to characterize the material behavior under the friction stir conditions. For this experiment, the tool had a 20 mm diameter operated at 2250 rpm and with plunging speed of 2.54 mm/s. The thickness of the aluminum was 3 mm. The steel sheet had a thickness of 0.7 mm, and it had a 3.0 mm diameter punched out hole. The anvil had a circular cavity of 4 mm diameter and the cavity had a 0.7 mm depth. The top workpiece was made of aluminum 6014, and the bottom was GM2W. The following is the description of the test and **Figure 10**, which shows the outcome of the experiment.

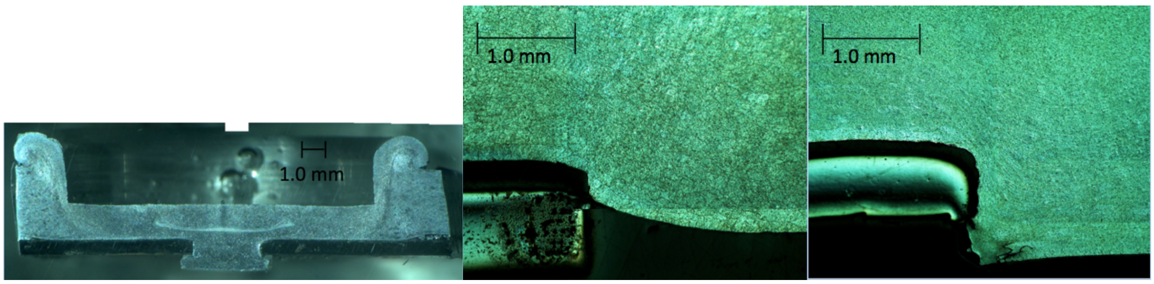

a) Finished sample: 1.6 mm (only Al) b) Plunge depth: 0.4 mm c) Plunge depth: 0.6 mm

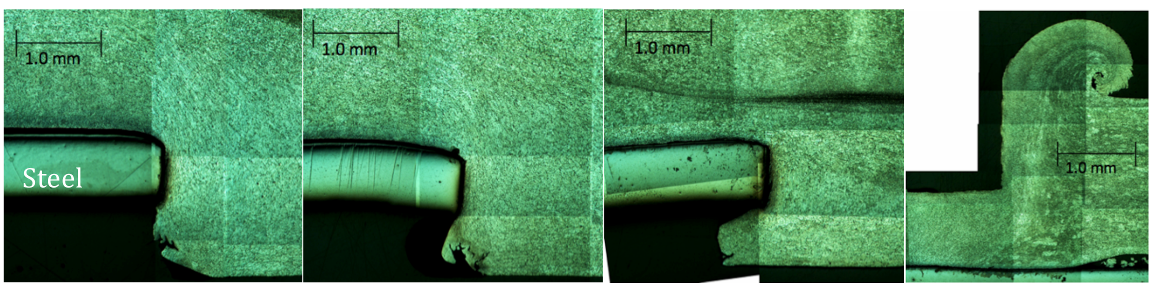

d) Plunge depth: 0.8 mm e) Plunge depth: 1.0 mm d) Plunge depth: 1.6 mm e) Flash at 1.6 mm

Figure 10: Material progression at the different depts.

During the FSF procedure, the tool was stopped at certain points along the plunging trajectory (0.4, 0.6, 0.8, 1.0, and 1.6 mm). The points were chosen because they are a fine representation of the material progression, and that includes the neck, head, and flash. After the first stop, the sample was taken away. Then, the preparation for the second sample, that will experience a deeper plunging depth, was on the way. This approach was continued until the last point.

On **Figure 10** a) shows the cross-section of a fully developed sample. **Figure 10** (b-d) shows the progressions of aluminum on five different plunge depths. In addition, the head shows some material degradation. **Figure 10** e) shows flash at the final plunge depth and aluminum detachment from the steel in the lower right corner of the figure.

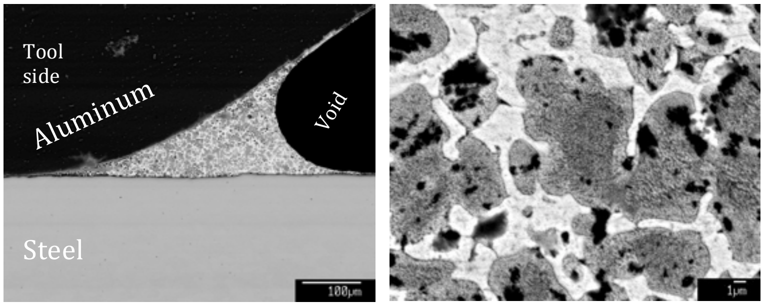

(a) Detachment (b) Zinc accumulation

Figure 11: Aluminum detachment from the bottom workpiece and zinc accumulation (BSE images)

The FSF samples also needed appropriate spectroscopy analyses as well. **Figure 11** shows zinc accumulation in the beginning of the separation and shape of the separation. This is the same part of the joint as was presented in the lower right corner of **Figure 10** e). **Figure 11** a) is a picture that was done in backscattered electron mode (BSE) and it shows the beginning of the aluminum separation. As the aluminum moves under the pressure of the tool, it also pushes the zinc away from the area that is under the tool. Where the aluminum separates from the steel, zinc accumulates. This causes zinc to accumulate on that end of the separation. **Figure 11** b) shows a closer look of the zinc accumulation from **Figure 11** a). The accumulation has a significant amount of aluminum in it. Since this was captured with a back-scattered electron detector, the darker phase has more aluminum, while the whiter has more zinc.

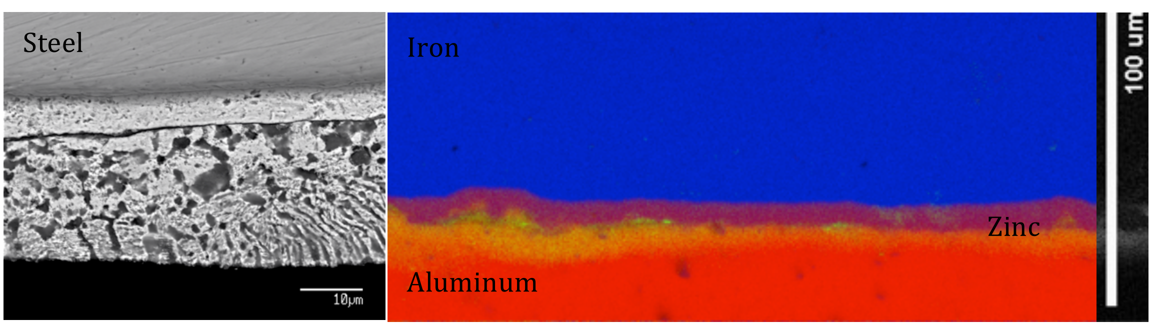

a) Zinc layer b) Zinc diffusion

Figure 12: Zinc and the steel-aluminum contact in a single pin sample

Figure 12 a) is showing the zinc coating of the 0.7 mm thick GMW2 steel before the joining procedure. **Figure 12** b) is showing the brazing layer of a single pin sample. This element map was done by Electron Microprobe Analysis and it shows the elemental distribution of iron (blue), zinc (green), and aluminum (red). It was taken right next to the aluminum neck area. Thus, this would be the most heated area between the two workpieces. Yet, there is no formation of the intermetallics, only brazing if the steel is zinc coated.

This paragraph aims to explain the significance of the zinc diffusion (brazing) and zinc accumulations. The zinc has bonding properties, and that has an influence on the behavior of the joints. As the tool approaches the final plunge depth, zinc in the buildup is molten (localized melting). The buildup also contains some amount of aluminum. When the tool finishes the plunging stage, it immediately starts retracting. This has a profound influence on the buildup. Right at that moment, there is no more heat generation due to stirring and there is no pressure due to plunging. All of the devices such as holder, anvil, and clamping devices act as heat sinks. Some of the heat will be taken away by the air as well. As a result, the temperature drastically drops. That causes grains nucleation and they have to grow faster along energetically more favorable crystallographic directions. Therefore, the build up has a dendritic structure. Zinc that is in the area that is under the tool behaves differently as **Figure 12** shows. Based on atomic radii, crystal structure, electronegativity, and valence difference, zinc is fully soluble into aluminum. Therefore, zinc diffuses into the aluminum. Since diffusion depends on the temperature and time, and that there is a rapid cooling rate when tool retracts, the zinc diffusion rate slows down as well. Since the zinc diffusion into the aluminum coupon occurs together with the buildup in the end of that area, the strength of the joint is significantly higher than in a situation where aluminum and bare steel were joined. In addition, this bonding fails catastrophically.

4.2. Clinching Experimental Results

In the single pin design, the top workpiece was made of aluminum, but in the clinching joint the situation is quite different. The aluminum workpiece can be placed on top or bottom. The following is an example when a steel coupon was the top workpiece. In that case, there would be formation of the intermetalic compounds, and that is shown on **Figure 13**. The BSE images are limited to the grayscale range since the coloring represents the average atomic number. Thus, the white phase on the left on the **Figure 13** b) and c) represent iron (steel), while the huge darker face on the right of those BSE represents aluminum. To convey more information, especially about the middle cracked layer, a line-scan was performed by an energy dispersive spectrum detector from steel to aluminum over the layer (**Figure 14**). The semi-quantitative result of the analysis suggests that the layer in the middle is Al_5Fe_2. Further analysis would find $FeAl_2$ and $FeAl_3$ on the right side of the intermetallic layer, or iron rich intermetallics FeAl and Fe_3Al on the left.

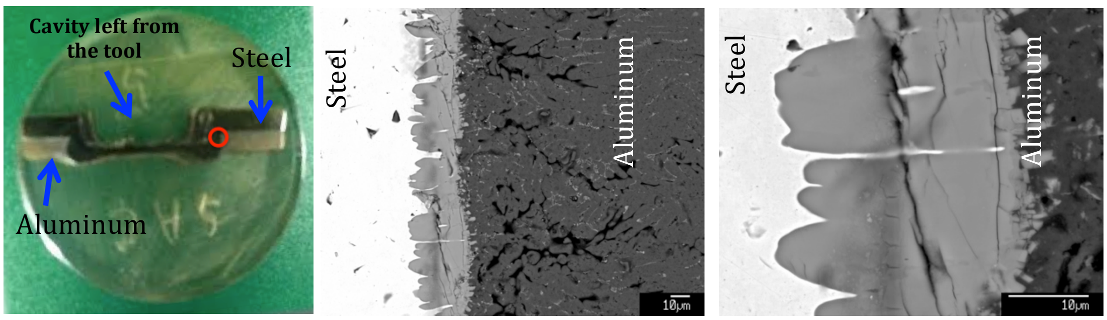

(a) Optical (b) Steel/Aluminum interface (c) Closer view

Figure 13: Optical and SEM pictures of a FSF sample that has steel as top material

Accelerating voltage used for the spectroscopy was 20 kV.

In this case, by using the steel instead of the aluminum as the top workpiece, the FSF tool generates more heat than would be otherwise. The result of the higher heat generation caused the formation of the intermetallic compounds, which are absent when the aluminum is the top.

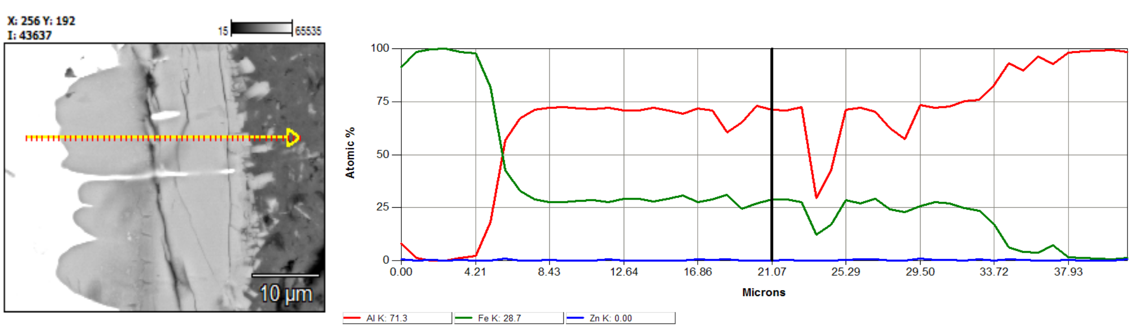

Figure 14: A line-scan result of the middle layer

The arrow on the left figure represents the direction of the scan. On the left is the outcome of the scan. Accelerating voltage used for the scan was 20 kV, and magnification of the picture above was 2500.

It can be seen from the last two figures that when steel is the top worksheet material that intermetallic compounds are occurring. The compounds are unwanted because of their brittle nature.

4.3. Special Interest Areas

During the examination and preparation for the modeling, there were six areas of special interests. The areas can be seen on **Figure 15**, and the following is the list of the areas and justification for the choice.

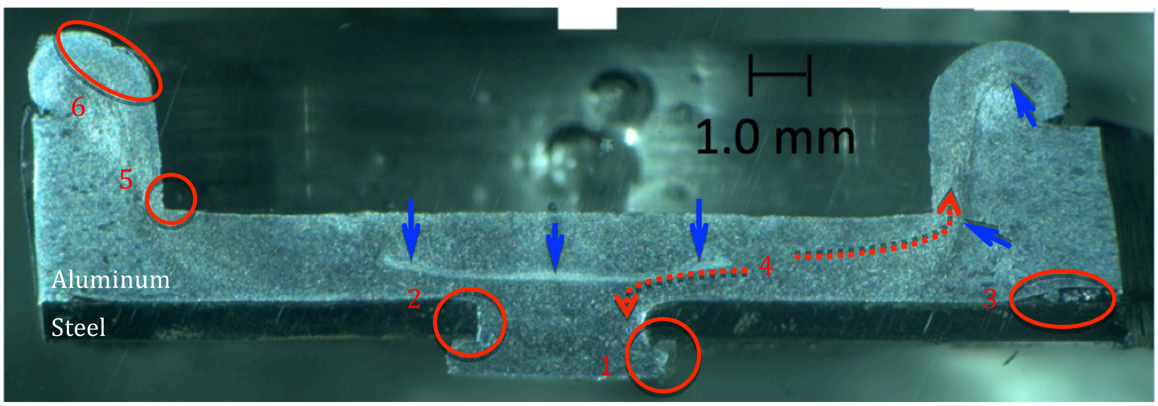

Figure 15: Modeling special interest areas

There are six area of interest: 1) head, 2) neck, 3) aluminum detachment, 4) coin, 5) tool rim, and 6) flash.

4.3.1. Head

This area is focused on the head, and that includes: formation, shape, progression, and completeness. This area has a higher importance since the characteristics of the head influences the strength of the joint. Therefore, it is important to determine the fundamental characteristics of the region. When it comes to the possible simulation challenge, the region that is most acceptable to the development of simulation inconsistencies is located on the upper edge of that part, the edge that touches steel. This is problematic because the aluminum first moves through the steel hole, which is 90° from the original position. Then, when it reaches into the space of the anvil's cavity, the material changes direction for another 90° (180° change form the initial direction). It was observed in experimental conditions that the upper corner has material deterioration as well as zinc accumulation, **Figure 10**.

4.3.2. Neck

This region describes the progression of aluminum, possible steel deformation, and diminishing of the zinc layer. As the tool progresses, the top material becomes plasticized, and it fills the steel hole and the cavity of the anvil. As this filling process advances, the aluminum passes over the upper and lower edge of the steel hole. This represents special interests for modeling personnel since the plastic deformation and the temperature are higher on those edges. This is important to capture; however, the model is highly likely to develop inconsistencies in the area, and fail. Mesh and contact properties have to be defined in a way that the inconsistencies have a lower chance for development.

For the material that was used in the experimentation, it was found that the diameter of the bottom coupon hole of 3.0 mm, in combination with the 3.6 mm anvil's cavity diameter, yields good results. If the bottom coupon has a bigger hole in respect to the same anvil cavity diameter, the joint will have a weaker head. In the opposite situation, the steel will not be able to resist the pressure, and it will collapse into the cavity. The collapse prohibits the appropriate head formation, and that leads to weaker joints [Lazarevic et al., 2013].

4.3.3. Aluminum Separation and Brazed Joint

Aluminum separation from the steel occurs around the edge of the cavity left from the tooling procedure, and it is representing the edge of the brazed joint. As the tool progresses, the aluminum starts to move in the directions that is represented with the red arrows (**Figure 15**). This movement influences the zinc layer that is on the surface of the steel worksheet, and due to the pressure and temperature increase, the zinc starts to form a brazed joint by diffusion into aluminum, **Figure 12** b). In addition, an amount is scrapped towards the separation and towards the head (area 1).

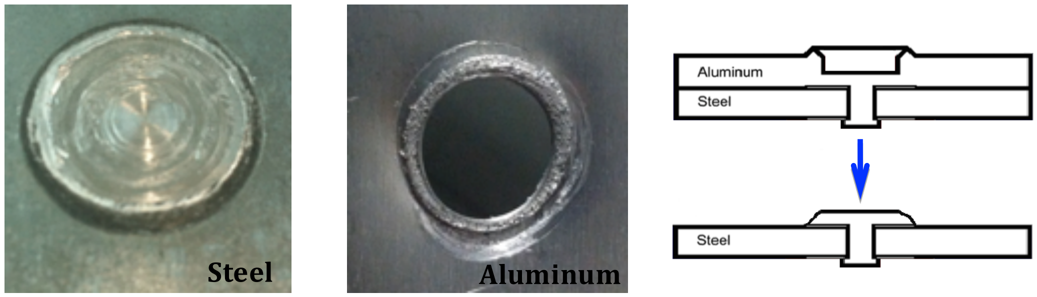

(a) Peeled aluminum (b) detached Al coupon (c) Aluminum peeling

Figure 16: Aluminum peeling failure

On the left is aluminum peeled off from a steel coupon. In the middle is a view of the top of the aluminum coupon. The steel part of the specimen is shown in the previous picture. The walking mark and the sample holder mark can be seen here as well. The holder mark shows because swelling occurred. The flash is elongated from the lap joint shear test. On the right is a schematic representation of what is shown in the left picture. The blue arrow shows the transformation between an intact sample and a joint that experienced aluminum peeling.

As for the brazed joint, this area covers aluminum that is under the tool and it is between areas two and five (**Figure 15**). There are two reasons why this is important. First, the tool is stirring on top of the aluminum and the model needs to accurately capture the heat generation from the stirring and from the plastic deformation. Second, as the tool plunges, aluminum tends to follow the stirring and moves in two possible directions: towards the flash or towards the steel hole. This location changes over the plunging time. For example, after the aluminum completely fills the steel hole and the anvil cavity, the aluminum volume will start to resist any incoming aluminum.

The thickness of the coin is an important factor of the joint strength. As the tool progresses, it also weakens the top work material. One type of FSF joint failure is failure of the top work material along the edge of the rim that was left by the tool, which is area five. The crack nucleation happens on the edge of the separation and as the force increases, the crack will propagate through aluminum and along the separation edge. This aluminum sheet peeling is a ductile type of failure, and this happens because the brazing is stronger than the surrounding aluminum part. This is shown on **Figure 16**. The FEA model should give a clear vision of what is happening in the region and it should give clear recommendations for the plunge depth that is needed.

In the next figure, **Figure 17**, the pictures were taken with a secondary electron detector. Magnification of the pictures is 40x, and the acceleration voltage was 20.00 kV. The figure shows an aluminum surface that was separated from the joint (only the brazed part). There are three distinguishing surfaces. The first surface is marked by the aluminum moving towards the steel hole, while the third surface is marked by the aluminum going away from the steel hole (away from the center of the tool). The direction and orientation of the marks is influenced by the direction of the stirring tool, and the marks in the second region follow the rotation most correctly. The third region ends with the detachment, and the aluminum that was passing through moved outwards. The figure also shows cracks along the detachment and next to the neck. The nucleation and the crack propagation happened because the sample was put through a lap shear test [Lazarevic et al., 2013]. Close to the end of the third surface, there is zinc buildup, which is the white phase. In that area, there are two parallel cracks. The blue arrow shows the maximum of detachment. The marks that reach the maximum from the side that was not under the tool, on the right side on the picture, have an angle that is slightly larger than 45°. Marks that reach the maximum from the inside of the joint have a much steeper angle.

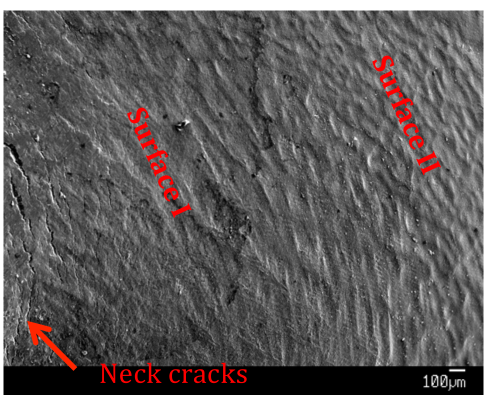

(a) Brazed joint (Aluminum side close to the neck)

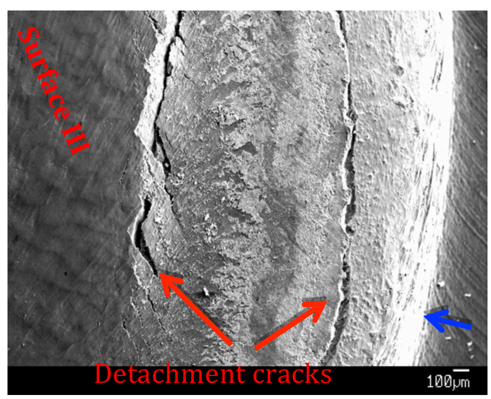

(b) End of brazed joint

Figure 17: Bottom coin surface (the brazed joint)

4.3.4. Thermo-mechanically affected zone

The five blue arrows on **Figure 15** show a distinct boundary between two different microstructures, the material that was directly under the tool and material that formed in the cavity. This boundary is an indication that the material that was under the stirring tool was following the rotation, and is commonly termed the thermo-mechanically affected zone. Material that was forming into the cavity did not follow the rotation, which is characterized as the heat affected deformation zone. The tool plastically deforms material into two different ways: plastic deformation due to stirring and plastic deformation due to plunging. The thermo-mechanically affected zone experienced both plastic deformations, while the heat-affected deformation zone is plastically deformed due to plunging only. Simulation of the boundary between the two zones is very difficult with the current ideation of the FEA software.

4.3.5. Aluminum Cavity Edge

Aluminum that is on the rim of the tool undergoes significant plastic deformation as well as high temperatures due to stirring and the frictional heating. Cross sectioning of the samples reveals that the angle between the aluminum that was under and on the side of the plunged tool has an angle of 90° or slightly greater, as shown on **Figure 15**. This is important information for a simulation developer since the model has to follow the criteria and the model has a higher chance to develop inconsistencies in this region. In the other words, this region would most likely cause the simulation to fail.

4.3.6. Flash

While flash does not affect the strength of the specimen or any other critical value, it detracts from the perceived joint quality. Flash can be removed by grinding, but at an additional process cost. A simulation should accurately portray the geometrical as well as temperature and stress profiles. As can be seen in section 3.4, the flash temperature was measured and that gives important information, as well as a constraint to the model. Simulation outcomes should suggest the appropriate dimensions of the holder and the plunge depth, which would lead to a less prominent flash (smaller height).

4.4. Temperature Analysis

The tool has a crucial importance during the joining procedure. The tooling generates heat due to stirring and plastic deformation. There are different ways to measure temperature profiles of the system, but every approach has its own shortcomings and advantages. As was stated before, in this research, two different approaches were taken: thermocouples for gathering basic temperature data, and an infrared camera for the model validation after the model was developed (Section 6.1). The major shortcoming for thermocouples is that they are a point measuring device. The major shortcoming for infrared cameras is that they measure only surface temperature distributions. These shortcomings could be transcendent with a FEA model.

4.4.1. Thermocouple Temperature Measurement Results

The graphical representation of the results can be seen on **Figure 18**.

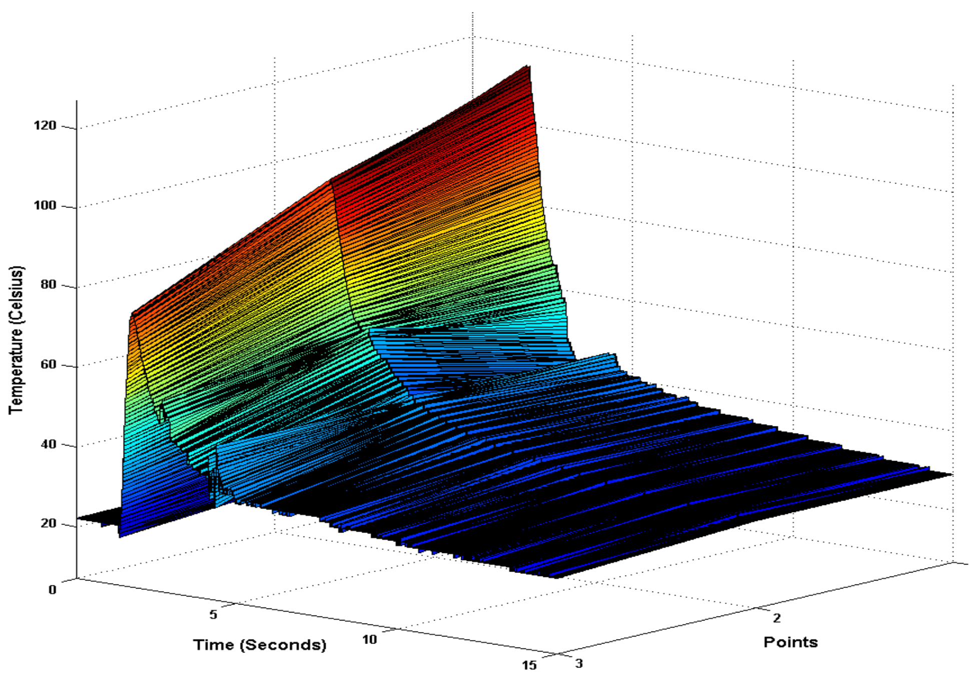

Figure 18: Thermal profile for the 3 points

The parameters for this specimen were: 1.0 mm thickness and 0.9 mm plunge depth. The profile looks the same with different process parameters. Only the value of the maximum temperature is different.

From the thermal analysis, it can be concluded that the temperature radially decreases away from the center of the joint. The temperature rapidly increases with the start of the procedure. It reaches the maximum when the stirring is done. After the tool is removed, the temperature declines slowly. The sample was taken out of the fixture four seconds after the tool stopped. That is shown on **Figure 18** as a noise at that time interval.

The temperature of the zinc layer under the tool during the joining procedure is not the same for the different coupon thicknesses. The temperature is higher in samples with the thinner top coupons since the layer was closer to the stirring tool. The temperature inside of the core is higher than on the edge of the core. The temperature must be higher towards the center of the joint. For some samples, it must reach the melting temperature, since the zinc layer melting was documented on some of the samples. The thickness of the thermocouples introduced a small gap between the two work materials. As a result of that, the measurement had an error because of the gap, and the higher temperatures were not recorded.

During the stirring, the pressure and the temperature are high under the stirring tool. At the moment when the tool starts to retract, the pressure from the tool disappears, but the temperature lags behind. Depending on the machine parameters, this may force zinc to cross the phase boundary (decompression melting).

5. Finite Element Analysis

This chapter gives an explanation of the background information that is needed for a FEA model development of the FSF process, as well as the outcomes of the current model.

5.1. Background Information

This section gives an explanation of the modeling prerequisites, including all the necessary data for a simulation that accurately portrays thermal profiles and material progression as a response to the forming. The ultimate goal for the modeling part of the research is to accurately describe and predict the material behavior during the FSF procedure.

However, it is difficult to develop an accurate FSF numerical model primarily because large work-material deformations cause problems with simulation convergence and completion. As can be seen from Chapter 2, prior knowledge about the fundamentals of the process such as appropriate tool size and design, optimal dimensions of the workpieces, temperature distribution, etc. is not fully available. FEA can be used to test new tool designs and experimental configurations. When it comes to the design of the hole, information is needed about the position in relation to the tool and anvil axes, number, appropriate size a.k.a. diameter of the hole, and shape i.e. conical or cylindrical. With proper modeling techniques, the situation can be profoundly changed. Some of the major obstacles to that goal are associated with selection of the appropriate mesh element, mesh size and partitions, plasticity model, contact pairs, boundary conditions, distortion control, computational time cost, transfer of the results between modeling steps, and effects of material bonding. For this study, ABAQUS/Explicit was chosen based on its ability to solve complex contact conditions. It is an explicit dynamics finite element program. A two dimensional model was created to minimize computational time by symmetry boundary condition and reduced number of elements. Then, a more complex three-dimensional model was created to more accurately simulate the experiments with the spinning tool and frictional contact condition in the process. COMSOL Muliphysics software was also explored, but it was less successful.

5.1.1. Johnson-Cook Plasticity Model and Heat Generation

For this study, the Johnson-Cook model was used to describe simultaneously the flow stress as a function of strain, strain rate, and temperature. This empirical material model is particularly suitable for high-strain-rate deformation of metals, since it is considering a large range of strain rates and temperature changes due to thermal softening by large plastic deformation [Abaqus Analysis User's Manual]. This model is a particular type of von Mises plasticity that includes analytical forms of the hardening law and rate dependence. The model is described with Equation 1. This equation has three different terms: elasto-plastic, $A + B\left(\bar{\varepsilon}^{pl}\right)^{n}$ viscosity, $1 + C\ln(\dot{\bar{\varepsilon}}_0/\dot{\varepsilon}_0)$; and softening term, 1- $\hat{T}^m$.

$$\sigma = [A + B\ (\bar{\varepsilon}^{pl})^n]\,[1 + C\ln(\dot{\bar{\varepsilon}}^{pl}/\dot{\varepsilon}_0)]\left(1 - \hat{T}^m\right). \quad \text{Equation 1}$$

$$\text{Where: } \hat{\boldsymbol{T}} = \begin{cases} \mathbf{0} & \Rightarrow \boldsymbol{T} < \boldsymbol{T_{transition}} \\ (\boldsymbol{T} - \boldsymbol{T_{transition}})/(\boldsymbol{T_{melt}} - \boldsymbol{T_{transition}}) & \Rightarrow \boldsymbol{T_{transition}} \le \boldsymbol{T} \le \boldsymbol{T_{melt}} \\ \mathbf{1} & \Rightarrow \boldsymbol{T} > \boldsymbol{T_{transition}} \end{cases}$$

In the equation, σ is the equivalent stress, A is the initial yield stress (MPa), B is the hardening modulus (MPa), C is the strain rate dependency, m is the thermal softening coefficient, n is the work-hardening exponent, $\bar{\varepsilon}^{pl}$ is the equivalent plastic strain, $\dot{\bar{\varepsilon}}^{pl}$ is the plastic strain rate, and $\dot{\varepsilon}_0$ is the reference strain rate with the usual value of 1.0 s^{-1}.

When it comes to the softening term, T_{melt} is the melting temperature of the material, and $T_{transition}$ is a transition temperature. The transition temperature is usually chosen to be the room temperature, 293.15 K (20°C), so the software calculates changes in the material at all times. When $T \geq T_{melt}$, the material is melted and it behaves like a fluid; thus, there will be no shear resistance since $\sigma = 0$. The hardening memory will be removed by setting the equivalent plastic strain to zero. All of the used Johnson-Cook values for the aluminum domain can be seen in **Table 2**.

Table 2: Johnson-Cook parameters for AA6061-T6 [Seli 2012]

Symbol [Unit]	A [MPa]	B [MPa]	n	m	T_{melt} [K]	$T_{transition}$ [K]	C	$\dot{\varepsilon}_0 [s^{-1}]$
Value	324	114	0.42	1.34	952	293.15	0.0083	1

The work material is Al 6061-T6 because the information is readily available. The material properties used in this study can be seen in **Table 3**. The ABAQUS code has no built-in system of units. For this project, the International System of Units (SI system) based units were only used, and all other units were derived from them.

Table 3: Temperature-dependent material properties for AA 6061-T6 [Soundararajan 2005]

Temperature [K]	310.95	366.45	422.15	477.15	533.15	589.15	644.13	700.15
Thermal conductivity [W/m•K]	162	177	184	192	201	207	217	223
Heat capacity [J/Kg•K]	945	978	1000	1030	1052	1080	1100	1130
Density [Kg/m^3]	2690	2690	2670	2660	2660	2630	2630	2600
Young's modulus [GPa]	68.5	66.2	63.1	59.2	54	47.5	40.3	31.7
Thermal expansion [1/ K]•10^{-6}	23.5	24.6	25.7	26.6	27.6	28.5	29.6	30.7

The model assumes that Fourier's law of heat conduction is valid, so the governing equation for heat generation rate, $\acute{Q}$, with the moving tool is expressed as:

$$\acute{Q} = \rho c \frac{\partial T}{\partial t} - k\left(\frac{\partial^2 T}{\partial x^2} + \frac{\partial^2 T}{\partial y^2} + \frac{\partial^2 T}{\partial z^2}\right). \qquad \text{Equation 2}$$

The elements of the equation are the following: T, temperature; $\rho = \rho(T)$, density; $c = c(T)$, specific heat; $k = k(T)$, heat conductivity; t, time; and (x, y, z) as domain coordinates. The heat generation consists of frictional heat generation from tool/workpiece contact that follows Coulomb's friction law, q_f, and plastic deformation heat rate, q_{pl}.

$$q_f = 2\pi r \omega \mu F_n \qquad \text{Equation 3}$$

$$q_{pl} = \eta \sigma \dot{\varepsilon}^{pl} \qquad \text{Equation 4}$$

Frictional heat generation depends on two components. The first component, $2\pi r\omega$, is directly proportional to the trajectory, $2\pi r$, and the angular frequency, ω. At the tool center, the radius is zero, $r = 0$. Therefore, there is no frictional heating at the point. This demonstrates that a tool with a bigger diameter would generate more heat, and that the heat generated will be concentrated away from the tool center at the surface of the top workpiece. The second component is the frictional force, μF_n. As the tool pushes down on the workpiece, the force will be progressively transformed into heat. The controlling factor is the friction coefficient since it depends on slip rate, contact pressure, and average surface temperature at the contact point. In other words, friction coefficient is directly defined as $\mu = \mu(\dot{\gamma}_{eq}, P, \overline{\mathrm{T}})$ where $\dot{\gamma}_{eq}$ is the equivalent slip rate, P is the contact pressure, and $\bar{T}$ is the average temperature at the contact point, $\bar{T} = (T_{\mathrm{A}} + T_{\mathrm{B}})/2$. T_A and T_B are temperature at points A and B on the surfaces. Point A is a node on the surface, and point B corresponds to the closest point on the opposing surface.

As the temperature increases due to the tool stirring, the friction coefficient decreases, which makes the heat generation slowdown. In addition, the temperature increase causes Young's modulus to decrease, i.e., the softening helps the work material to be forged. At the melting point, Young's modulus and friction coefficient are zero, i.e., the work material stops being heated, and it is in the liquid state. It is important to mention that heat from plastic deformation will be higher with higher plunge speed. However, the heat contribution from the friction is significantly higher than from the plastic deformation. On the other hand, plastic deformation heat rate, q_{pl}, depends also on inelastic heat fraction, η. It is usually assumed constant with a value of 0.9. That means that 90% of the mechanical energy is converted into heat, and the remaining percentage is stored energy.

Interactions between domains are setup with frictional contact described by Coulomb's frictional law, as was previously described. The frictional contact is temperature dependent since the friction coefficient, μ, is different with different temperatures. The values used for the coefficient for the aluminum/steel contact are represented in **Table 4**.

Table 4: Coefficient of friction dependency on temperature [Seli 2012]

Temperature [K]	295.15	307.85	366.15	420.65	483.75	533.15	588.75	644.25	699.85	952
Friction coefficient, μ	0.61	0.545	0.259	0.115	0.064	0.047	0.035	0.02	0.007	0

It is crucially important that the model has fully coupled thermal stress analysis, since the stress solution and temperature distribution are interdependent. There is significant heating due to stirring and inelastic deformation of the aluminum, which changes the material properties. Contact algorithms between all domains in the system correspond to all these changes. The heat conducted between surfaces may depend strongly on parameters such as the separation of the surfaces, the pressure transmitted across the surfaces, average temperature of the interface, geometry of the contacting surface, yield strength, and roughness of the materials. Assigning the values of the thermal contact conductance is a challenging task because its dependence of all those factors.

The software simultaneously obtains the thermal and the mechanical solutions. ABAQUS/Explicit allows only clearance dependent data and/or pressure dependent data input. This model uses only the clearance dependency, and it assumes that at a distance of 0.1 mm conductance goes to zero. This is important for all the contacts, but the most sensitive space would be the aluminum/mild steel contact in the area of the aluminum detachment. Most authors, such as Park et al., [2008] use value of thermal contact conductance between the aluminum and the steel in a range between 3 to 13 $KW/m^2 \cdot K$. In the current FSF model the value was 10 $KW/m^2 \cdot K$. However, just for a comparison, value of 1.1 $MW/m^2 \cdot K$ was also used. Obviously, the second value is drastically different and inaccurate. This was chosen in order to make certain outcomes more obvious.

5.1.2. Stick - Slip Condition

It is assumed that the contact pressure stress will become very large in the model, and the shear stress at the interface will exceed the yield stress in the aluminum beneath the contact surface of the tool. This phenomenon is known as sticking, and during this time, some incremental slip between the surfaces may occur. The friction model defines the critical value; and after that, the two surfaces have total sliding. In other words, in the Coulomb friction model, two contacting surfaces can conduct shear stresses up to a certain value, and then they are sliding relative to each other. Usually, the maximum shear stress, $\bar{\tau}_{max}$ for this is calculated in the following way: $\bar{\tau}_{max} = \sigma_y/\sqrt{3}$. Thus, the maximum shear stress for the simulation was chosen to be 200 MPa. In ABAQUS/Explicit, the Penalty permits the relative motion of the surfaces when they should be sticking, and this is defined by elastic slip. At this time, elastic slip had the same value of 200 MPa.

Maximum shear stress and elastic slip values are critical, and they define the accuracy of the model since they directly affect the heat generation and the mesh. The best source for the values is coming from the empirical data, and that could represent a challenge. After the development of the model, the last final tuning of the simulation is about accurately defining the two values. This is especially the case with the elastic slip value.

5.2. Two Dimensional Model and Submodels

The primary reason for developing a 2D model is to lower time and need for higher computation resources. An axisymmetric approach provides expediency and less computational cost on the hardware.

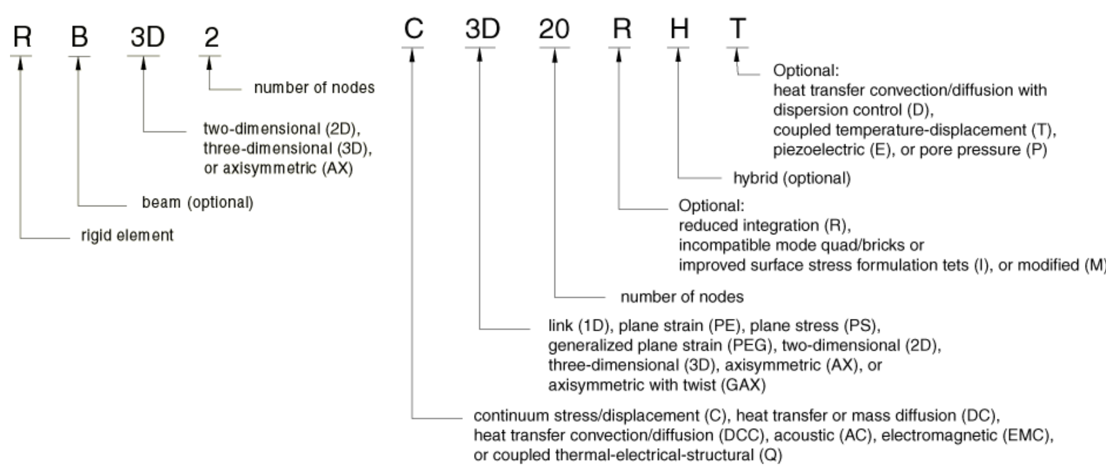

(a) Convention for rigid elements (b) Convention for non-rigid elements

Figure 19: Abaqus naming convention

There are two appropriate meshing element types for the 2D approach: CAX4RT for the deformable domains, in our case only aluminum, and RAX2 for all the ridged domains (wires in this case). CAX4RT is a-4-node thermally coupled axisymmetric quadrilateral element type with bilinear displacement that incorporates temperature. The element has reduced integration and hourglass control. For the ridged domains, wires, RAX2 has to be used (a 2-node linear axisymmetric rigid link). The Abaqus conventional naming method is represented on **Figure 19**. There are other elements and their names, but the figure shows only what is needed for the project.

In nonlinear simulations, such as this one, the top coupon material undergoes very large deformations, and that can cause inaccurate results or the analysis terminates due to numerical inconsistencies. A successful model has to accordantly correspond to the material progression. The solutions for this challenge are adaptive meshing and distortion control. The controls are designed to prevent negative element volumes and other excessive distortions from occurring during an analysis. In contrast to the adaptive meshing technique, distortion control does not attempt to preserve a high-quality mesh throughout an analysis. These two methods are mutually exclusive on a same section of a domain; therefore, distortion control was chosen for the task on the entire aluminum domain. The main reasons for the selection were that distortion control performed better and the computational time was smaller.

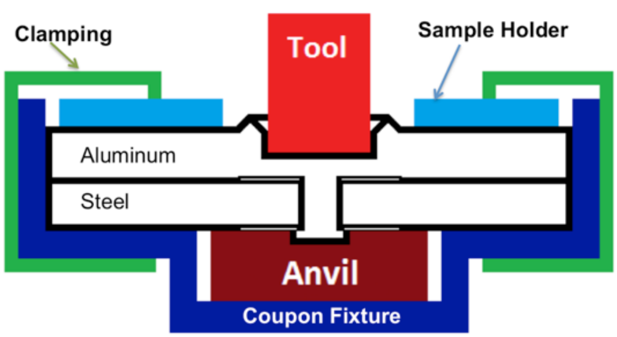

Figure 20: Schematics of a single pin FSF sample

Figure 20 shows a schematic representation of a FSF setup. For the simulation, clamping and coupon fixture are not essential. Their contribution is purely mechanical and there is no essential thermal influence on then the joint. Instead of the two devices, a model should have appropriate boundary conditions that are effectively represent them. Domains that are used in the simulations together with their dimensions can be seen in **Table 5** and **Table 6**.

Table 5: 2D Domains and their dimensions

Dimension\Domain	Tool	Aluminum	Steel	Anvil	Holder
Length [mm]	5.0	6.5	4.9125	6.5	0.4
Height [mm]	1.4	1.0	0.7	0.6	0.5

Table 6: 3D Domains and their dimensions

Dimension\Domain	Tool	Aluminum	Steel	Anvil
Radius [mm]	5.0	6.5	6.5	6.5
Height [mm]	0.5	1.0	0.7	1.0

The anvil has a circular cavity at the center 0.6 mm deep and with a radius of 1.8 mm.

In the next table, **Table 7**, the properties of the ridged bodies were displayed.

Table 7: Steel properties

Parameter	Density	Young' Modulus	Poisson Ratio	Heat Capacitance
Value	7750 Kg/m^3	210GPa	0.3	490 J/Kg•K

As can be seen from section 4.3, there are special areas of interest such as the edges of the steel hole, the tool, and of bottom of the anvil cavity. Those edges where rounded in this model, and the round up radius is 0.1 mm. This was the smallest allowable value that could have been used. The rounding technique makes the model more realistic; and furthermore, since the model is more likely to fail in those areas more than anywhere else, this is necessary so the model can be completed. Since the rigid parts are not fully analyzed, no deformation, the only information that is dictating meshing size is the round up areas. There should be at least five elements per a round up edge, and this is important for the quality of the aluminum mesh that is passing around the round up areas. The ridged parts have an element size of $3 \cdot 10^{-2}$ mm to satisfy this constraint.

In order to apply boundary conditions on an assembled rigid part, the domains need to have reference points (one reference point per a ridged domain). The tool and the anvil domain have reference points on the axisymmetric axis, while the other domains have it on the side that is away from the axis. All the reference points can be see on **Figure 21**. At this time, the plunge speed for the tool reference point was 10 mm/s, and all other reference points were fixed.

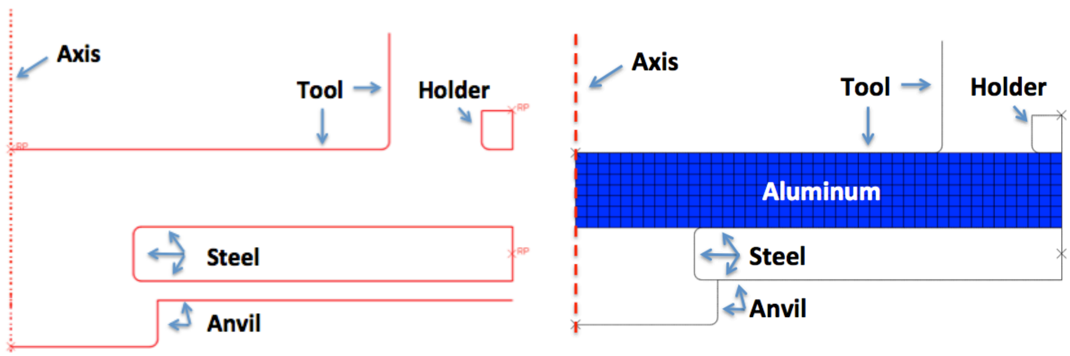

(a) All the rigid domains before assembly (b) All the domains are assembled.

Figure 21: 2D model

There are four domains in the model: tool on top, holder on the right upper corner, aluminum, steel, and anvil on the bottom. Aluminum is the meshed domain in blue, while the rest of the domains are wires and they are in red (grey on the figure on the right). The dashed red line is the symmetry axis. There are four X's on the figure (two on the axis and to on the far right). Those X signs represent reference points.

ABAQUS/Explicit provides two algorithms for modeling contacts that are not mutually exclusive: general and contact pairs. The FSF model requires the contact pairs approach because of its complexity. The contact pair algorithm requires careful contact definition since the interactions must be defined by specifying each of the individual surface pairs that can interact with each other. In addition, this algorithm allows penalty friction formulation that is necessary for the FSF samples. Parameters such as thermal conductance, friction behavior, and heat generation can be appropriately defined with this algorithm. Specific attention was placed on the tool/aluminum contact because of the pressure and heat generation input from the tool.

It is important to mention that the software does not automatically apply boundary conditions to nodes that are located on the symmetry axis in axisymmetric models. For the FSF simulation, aluminum nodes along the symmetry axis should be free to move as the tool is plunging. Therefore, the model has a boundary condition on the axis that prohibits those nodes to move horizontally, but they are free to move vertically. The boundary condition can be seen on **Figure 22** as they are represented as pink signs along the axis on the aluminum part. If this boundary condition is not applied, as the tooling progresses and the aluminum approaching the bottom of the cavity, the aluminum nodes will start to shift away from the axis, which yield inaccurate results.

One of the major challenges is the heat generation since tool rotation cannot be modeled in the 2D FEA. An appropriate surface heat flux that corresponds to Equation 3 was added into the tool/aluminum contact. The surface heat flux was radially distributed. This is represented in **Figure 22** as green arrows that are pointing downwards towards the aluminum. The distribution had to be offset and the offset value was $1 \cdot 10^{-9}$ mm. The reason for incorporating the offset is that zero value at the center produced errors and prevented the computation. Therefore, adding the miniscule positive value solved the problem and did not introduce a significant error.

However, since the surface heat flux approach did not yield appropriate results, the next option was to assume that the steel contact layer has maximum energy of the system (melting temperature of aluminum). Therefore, the tool had a predefined temperature of the molten aluminum. All of the other domains in the model had the room temperature of 293.15 K (20°C) as the predefine temperature. If the tool were a deformable entity, the surface heat flux approach would have a better chance to work because there are more degrees of freedom to constrain the temperature. That is not the case with wires.

The contact property between the tool and aluminum was setup so that separation after the contact is not allowed. This relationship can be specified only for pure master-slave contact pairs and cannot be used with adaptive meshing or with the general contact algorithm, which was satisfied in the model. If the model allows separation after the contact, the model yields inaccurate results in the center of the neck region. This error is significantly higher if aluminum is the only deformable part. **Figure 41** shows an example of a 3D model that allows the separation and the situation is the same for the 2D model.

After examining the model, it was concluded that there were two areas that needed to be more carefully analyzed. The submodeling technique was used to improve accuracy. This technique is based on interpolation of the solution from the global model with the coarser mesh onto the nodes on the aluminum domain of the boundary of the two submodels. Therefore, two different submodels were made with a much finer mesh in order to obtain more accurate and detailed solutions in those two local regions. Finer mesh is a priority since it increases mesh quality, which it determines the precision of the computational outcome.

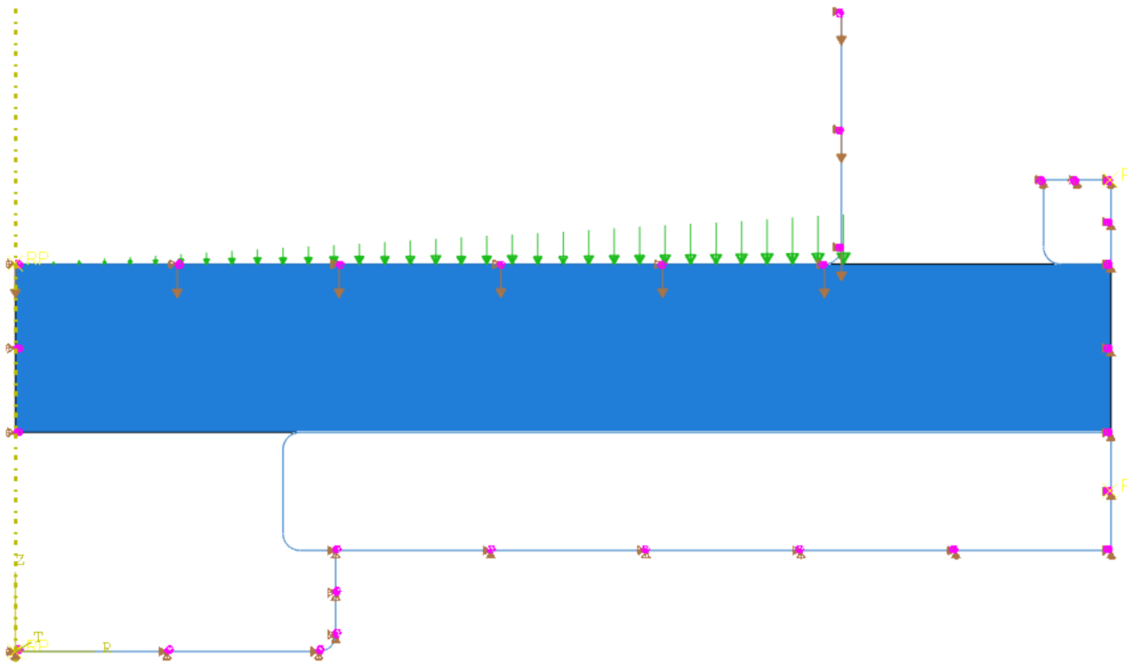

Figure 22: Assembled 2D global model with boundary conditions and surface heat flux

The brown arrows show domain movement (plunge speed), which is applied only to the tool. On the holder, steel, and anvil the arrowheads are placed on top of the pink circles, which means that those sides are fixed. The green arrows show the attempted surface heat flux. The yellow dashed line represents the vertical axis.

On the axis, in the aluminum region, the brown arrowheads and pin circles show that this side of the domain is fixed in the horizontal direction.

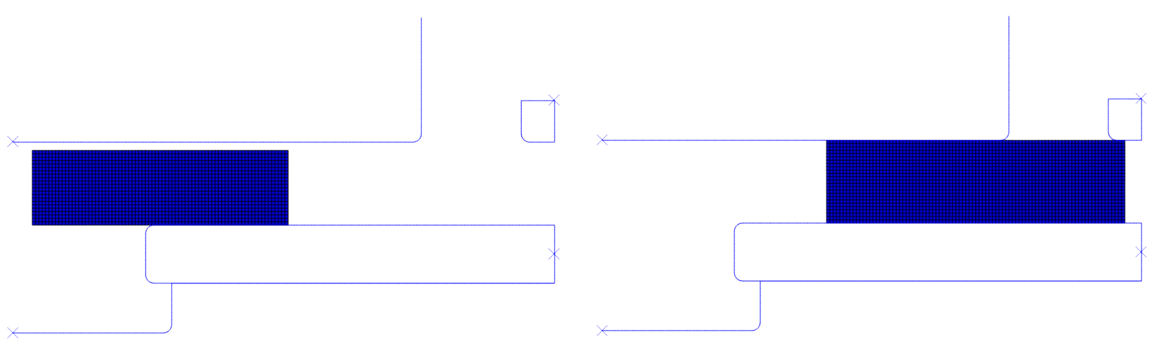

(a) First submodel (neck and head formation area) (b) Second submodel (aluminum swelling region).

Figure 23: 2D Submodels

The two regions are represented in **Figure 23**. The submodel domains had the distortion control and every other boundary condition that the global model had. In the left of **Figure 23** is the first submodel. This submodel is concentrated on the neck and head region. On the right is the second submodel that is focused on the area that is between the tool and the holder.

5.3. 2D Results

These results are split into two different sections: global model, and the submodel results. In global results temperature, heat flux, and stress are discussed. Then temperature, stress, detachment, and thermo-mechanical zone are discussed in the submodel results.

5.3.1. Global Model Results

From the laboratory experiments, it can be concluded that there should be an optimal plunge depth. If the plunge depth is smaller than the optimal value, the head will not be a fully formed, and the joint strength will be lower. The sample will fail at a lower force because the mechanical interlocking is not formed properly. The strength will also be lower if the tool moves deeper the optimal plunge depth. In this case, the remaining aluminum, the coin, would be too small. The failure mechanism is different in those two scenarios. If the plunge depth is too small, the brazed joint will nucleate a crack in the zinc buildup region. Then, the crack will propagate through the entire brazed joint and the neck. On the other hand, if the plunge depth is bigger than the optimal value, a crack will nucleate on the edge of the brazed joint, and it will propagate through aluminum to the edge of the cavity that was left by the tooling. After that point, the crack will follow that circular pathway of the cavity and the aluminum part will peel off. This is represented on **Figure 16** c). One goal of the research is to maximize the joint strength. Therefore, it is important to find out the optimal plunge depth. Three points are chosen to be appropriate to report the 2D global model outcome. They are 0.3, 06, and 0.9 mm plunge depth. At 0.3 mm, the neck is almost fully developed and the head formation is about to start. If the tool stopped at this value or before, the process would not achieve mechanical interlocking. At 0.6 mm, the global model implies that the head is almost fully developed. If the tool is stopped at this value, the model suggests that joint strength would be at the maximum. At 0.9 mm, the head was full formed, but the remaining depth of aluminum is 0.1 mm. This is suggesting that this sample will fail due to aluminum peeling.

5.3.1.1. Temperature

It is important to have a clear understanding of temperature distribution during the process in order to appropriately choose tools size, process parameters, and joint design. In the next figure, **Figure 24**, the temperature profiles given by the global model is represented. From the figure, it can be concluded that as the tool plunges, the heat generated from the joining procedure is stored in the entire joint. The distribution of the energy is suggesting that the neck/head as well as the region between the tool and the holder are getting a significant amount of the energy. Although aluminum in the neck/head region has enormous plastic deformation, aluminum on the side of the aluminum cavity receives more heat, and the thermo-mechanically affected and heat-affected deformation zones are different in those named two regions.

These two zones are different in the two regions. The reason for that is that aluminum that is under the tool is thermo-mechanically affected due to stirring and the volume that is close to the tool rim receives the most of it. Because the tool is constantly moving downwards, the pressure enfolds some amount on the side of the tool where the treatment continues but the pressure is dissipating. In the other region, the side of the aluminum cavity that is close to the tool is experiencing constant and lower heat generation rate. There are some major differences in the heat-affected deformation zones as well. There is less effect of stirring right above the neck region since it is closer to the center of the tool. The aluminum that flows into the head/neck region touches the steel and the anvil. Those sides act as a heat sink. After the head is fully formed, the pressure continues and the heat is still delivered to the heat-affected deformation zone. The model also is suggesting that the aluminum detachment begins at the same time that the head is nearly formed. All the temperatures are in kelvin.

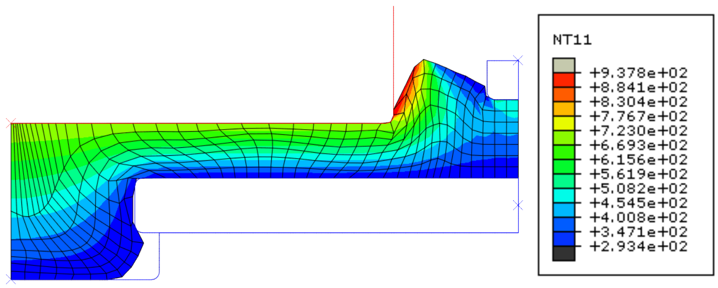

(a) 0.3 mm plunge depth

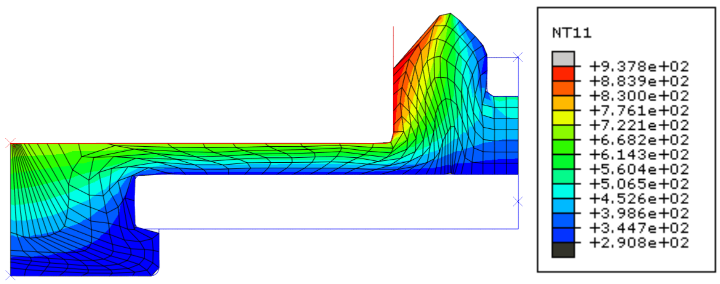

(b) 0.6 mm plunge depth

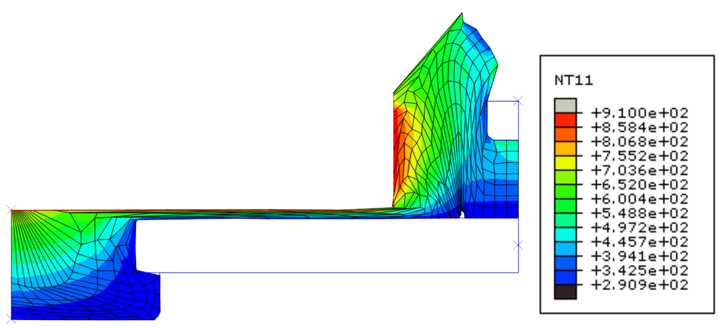

(c) 0.9 mm plunge depth

Figure 24: Temperature distribution of the global 2D model

The three points are 0.3, 06, 0.9, and they represent the beginning of aluminum's progression towards the area that is below the steel, aluminum filling the maximum volume of the anvil's cavity, and the end of the process.

5.3.1.2. Heat Flux

Heat flux is an important parameter to be characterized since steel, aluminum, and especially zinc layer properties are highly affected by the temperature increase. From **Figure 25** we can see that the flux is higher towards the steel work material as the tool progresses, which is expected and experimentally validated.

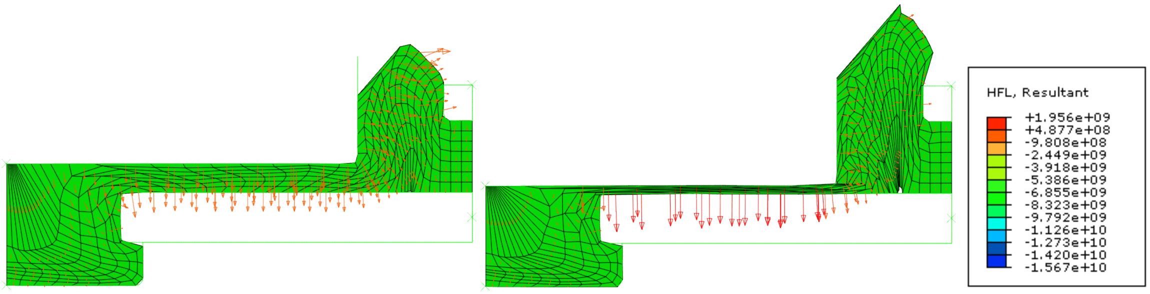

(a) 0.6 mm plunge depth (b) 0.9 mm plunge depth

Figure 25: Heat flux vectors

As the tool moves from 0.6 to 0.9 mm plunge depth, the heat flux is directed more downwards, and less towards the side of the tool. This happens for two reasons: 1) Friction heating is the dominating way of heat generation, and it is caused by stirring of the bottom of the tool rather then the side of the tool, 2) The remaining aluminum at the higher depth is being heated from stirring and plastic deformation is higher.

5.3.1.3. Stress

The initial yield stress for aluminum 6061 is 324 MPa at room temperature. The values for the von Mises stress will exceed the yield stress of the material, which means plastic deformation. Unfortunately, since this is a two-dimensional simulation, the results did not take into account the tool rotation where the material orientations vary.

From **Figure 26** it can be concluded that the von Mises stress distribution is higher in aluminum where it is in contact with the other domains: steel, anvil, and holder. Unfortunately, at this time, the simulation gives information about only what is happening in the aluminum. Therefore, it cannot be observed what is the stress concentration in the steel and the anvil, or between the two domains. The contact with the steel is very important. The steel domain in this case is rigid, and there are no stress analyses from the domain. If the steel were a deformable domain, the region of the workpiece that is above the anvil's cavity would be especially interesting. From the simulation it can be concluded that steel is possibly experiencing high stress throughout the entire surface contact with aluminum. That situation changes radially away after the aluminum detachment. However, it can be concluded that the aluminum in the anvil's cavity is also experiencing a uniform stress during the procedure, and the aluminum head is always under high stress.

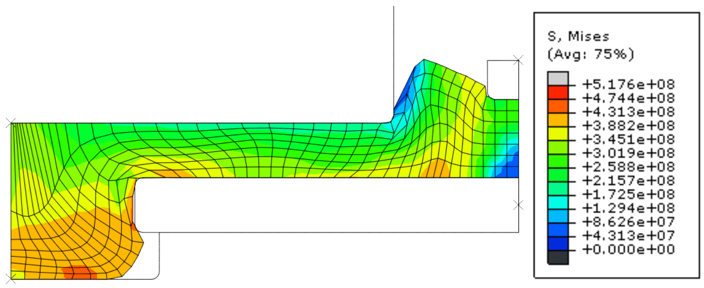

(a) 0.3 mm plunge depth

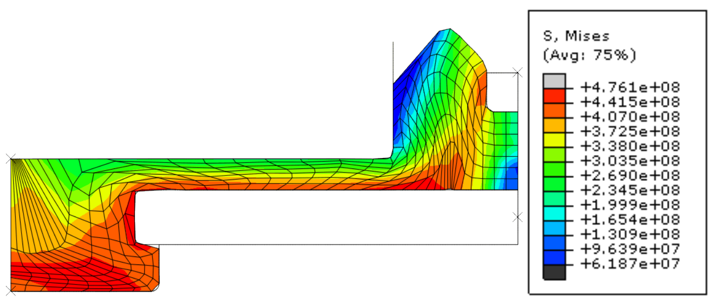

(b) 0.6 mm plunge depth

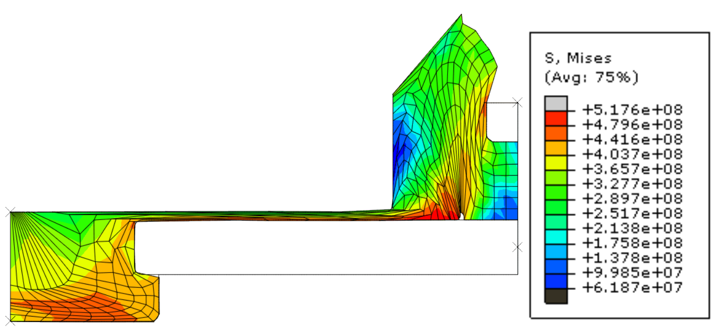

(c) 0.9 mm plunge depth

Figure 26: Stress distribution in the global 2D model.

5.3.2. Submodels

The first submodel is focused on the neck/head region. It is important to characterize the material progression in this area since the joint quality depends on it (quality of the mechanical interlocking). The second submodel is focused on the region that covers the aluminum cavity, the aluminum detachment, and the flash. The submodels have the approximate element size of $4 \cdot 10^{-2}$ mm in arrangement with a maximum geometric deviation factor of 0.2 (the default value). The deviation factor is a quantifier of how much an element edge deviates from the original geometry, and is defined as the ratio of the distance between the distorted and undistorted element's edge and the length of the same element edge. The default value for the factor is 0.2. The minimum size factor as a fraction of the global element size was chosen to be 0.99. This curvature control factor prevents ABAQUS/CAE from creating very fine meshes in areas of high curvature that are less important for the model such as kinks or fillets with a very small radius. The default minimum size that ABAQUS/CAE uses for the factor is 0.1 (10%). The reason for choosing the maximum value for the curvature control factor is that the model can maximize the head formation, but this value did not have a significant influence on the outcome.

5.3.2.1. Aluminum Detachment

Figure 27 a) shows a closer look at the aluminum detachment. The distance between the tool and the holder is 1.1 mm. As the tool progresses, the detachment from the steel starts at a 0.61 plunge depth and is located 0.8 mm away from the rim of the tool. The peak of the detachment has a height of 0.15 mm and a width of 0.55 mm. The maximum height of the flash at 0.6 and 0.9 mm is 1.1 and 1.5 mm, respectively.

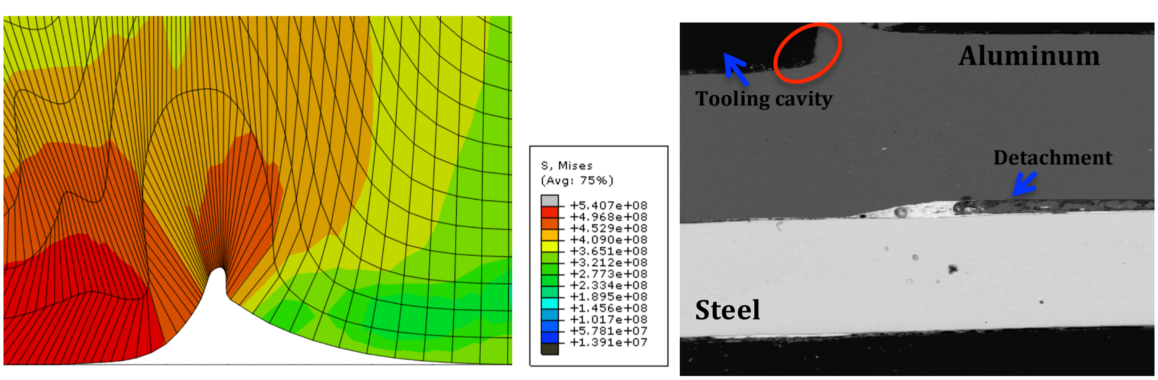

(a) FEA outcome (b) An experimental result

Figure 27: Aluminum Detachment

Contrary to **Figure 11**, **Figure 27** b) shows a BSE picture of a sample with the same dimensions and materials, but there is a quite long detachment. This is a product of the fact that the sample holder was not firmly fastened. The same situation can be seen on **Figure 28** c). The maximum detachment of **Figure 27** b) is slightly smaller than 0.1mm. The different detachment outcomes can be easily simulated by changing the holder's boundary conditions. This figure, **Figure 27** b), also shows that the aluminum cavity walls have more than 90° angle, and it is highlighted by the red ellipse.

5.3.2.2. Thermo-Mechanically Affected Zone and Heat-Affected Deformation Zone

The thermo-mechanically affected zone experienced both plastic deformations (plastic deformation due to stirring and plastic deformation due to plunging), while the heat-affected deformation zone is plastically deformed due to plunging only. The assumption was made that the part of the aluminum that experiences temperature above approximately 725K (452°C) is sufficiently close to the tool, the thermo-mechanically affected zone. This is represented on **Figure 28** b) with the elements that are colored in red. The line on the meshed part that is highlighted in **Figure 28** a) is placed manually on 1/3 of the thickness of the aluminum. The right end of the line is half of the distance between the tool and the holder. By this estimation, the thermo-mechanically affected zone has an approximate volume of 32 mm^3 (radius of 5.55 mm, height 1/3 mm). Everything under and aside the red line would not be considered as thermo-mechanically affected zone.

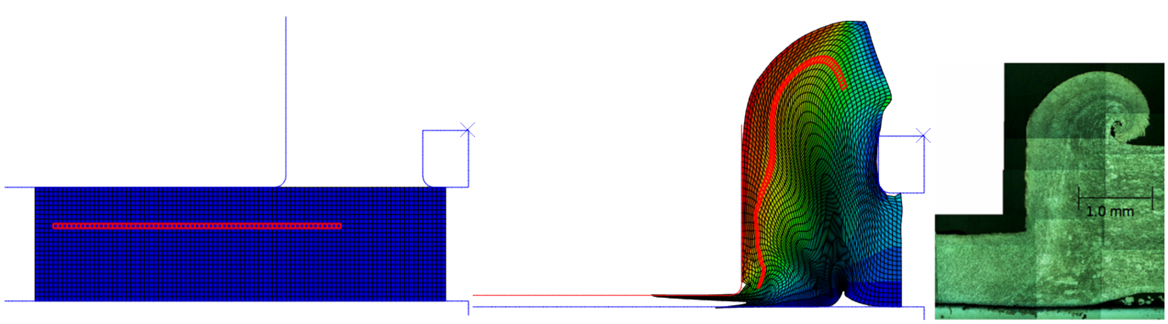

(a) Starting position (b) 0.9 plunge depth (c) Optical image

Figure 28: Thermo-mechanically affected zone prediction

5.3.2.3. Temperature Results from the Submodels

Figure 29 represents the temperature profile of the first submodel at the same plunge depths that were used for presenting all the results of the global model (0.3, 06, and 0.9 mm). **Figure 15** shows a borderline between the thermo-mechanically affected zone and the heat-affected deformation zone. It is desirable that the model encompasses appropriately this microstructure phenomenon.

The reason that 0.6 mm plunge depth is appropriate, according to the model, is that the upper corner of the head usually contains material degradation as was previously shown on **Figure 10**, and zinc accumulation.

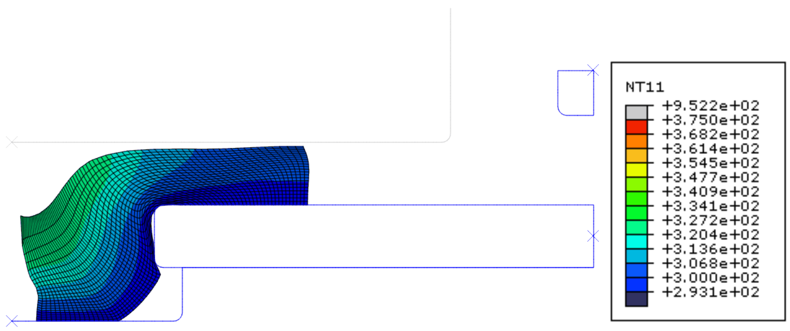

(a) 0.3 mm plunge depth

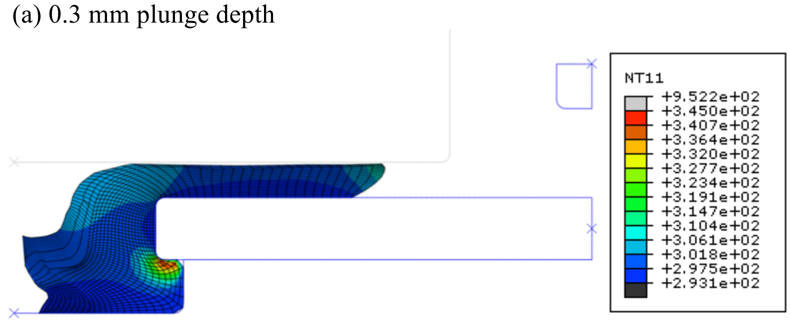

(b) 0.6 mm plunge depth

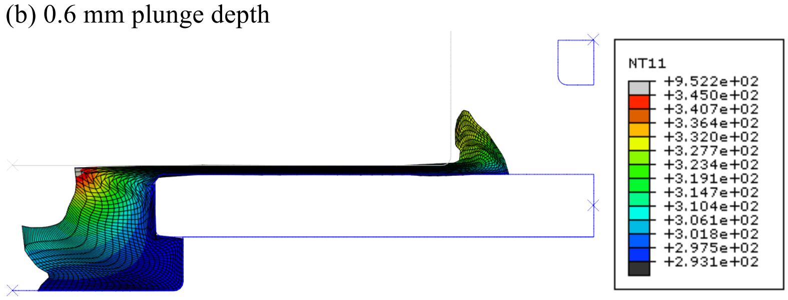

(c) 0.9 mm plunge depth

Figure 29: Temperature profile for the first submodel

The figure shows temperature distribution at 0.3, 0.6, and 0.9 mm of plunge depth.

Regardless of the mesh quality and the element size, the head edge will always lack full formation. This would be more obvious if the other domains are deformable in the model, especially steel since it can be deformed during FSF.

The submodel shows that on these depths, the aluminum has higher temperature, and that is especially true for the neck/head and region between the tool and holder. The aluminum has higher temperatures towards the center and the rim of the tool. As the tool progresses, the neck area continues to increase in temperature, but the temperature of aluminum between the tool rim and steel hole is leveled out.

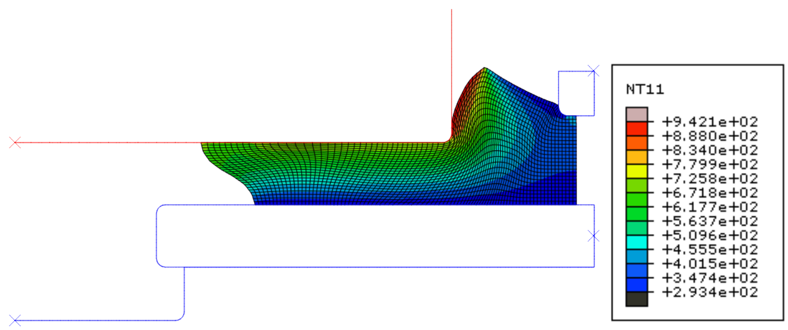

(a) 0.3 mm plunge depth

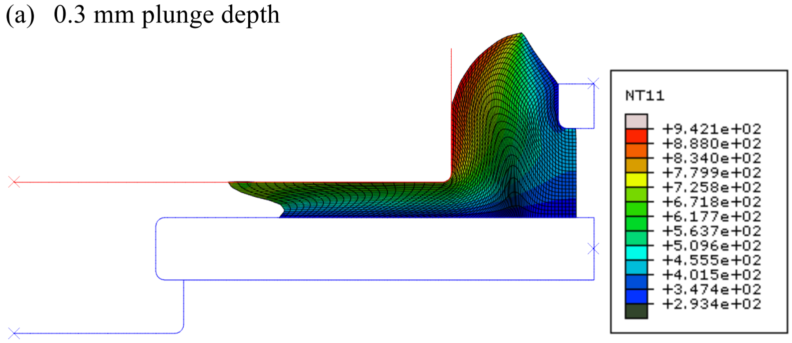

(b) 0.6 mm plunge depth

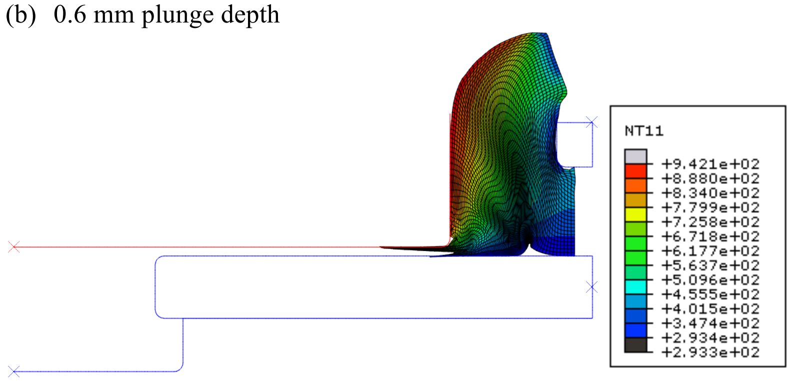

(c) 0.9 mm plunge depth

Figure 30: Temperature profile for the first submodel

The figure shows temperature distribution at 0.3, 0.6, and 0.9 mm of plunge depth in the second submodel.

As the tool progresses downward into the top work material, the material under and on the side of the tool gets heated. The second submodel shows that there is lot of heat transmitted to the flash. In addition, it is important to mention the aluminum progression, because of the plunging and the heat generation, the tool squeezes out all the aluminum in the second submodel. The second submodel started with an aluminum part that is 2.85 mm under the tool. At 0.3 mm plunge depth, the aluminum that is in contact with the tool moves in two directions. At 0.6 mm, since the neck/head cavity is full, the entire aluminum moves away from the center of the tool. In the end, at a 0.9 mm plunge depth, almost the entire aluminum amount is out.

5.3.2.4. Stress

The next two figures show the stress outcomes of the submodels.

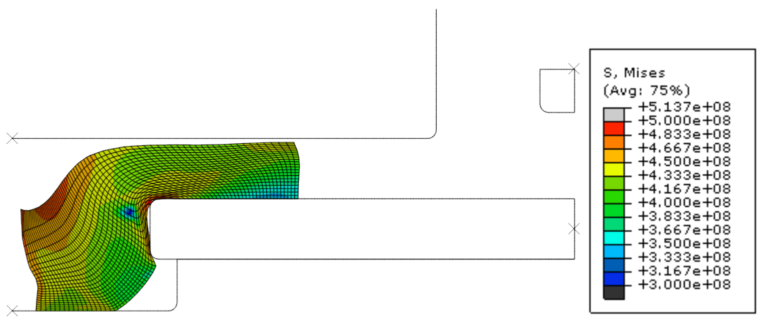

(a) 0.3 mm plunge depth

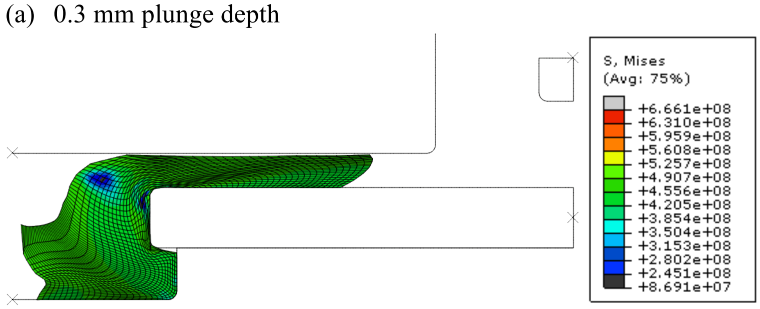

(b) 0.6 mm plunge depth

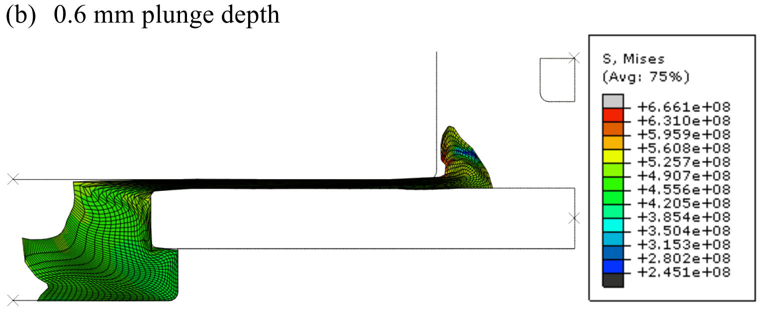

(c) 0.9 mm plunge depth

Figure 31: Stress profile for the first submodel at 0.3, 0.6, and 0.9 mm of plunge depth

The maximum stress that both the aluminum submodel domains have is on the side of the tool (closes point to the tool), and the value is 658 MPa. In the second submodel, the maximum stress was found on aluminum's contact with the steel between the tool rim and the detachment. The same area was forecasted in the global model as well.

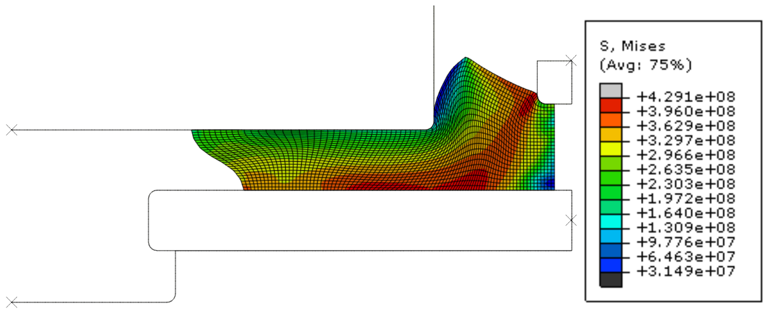

(a) 0.3 mm plunge depth

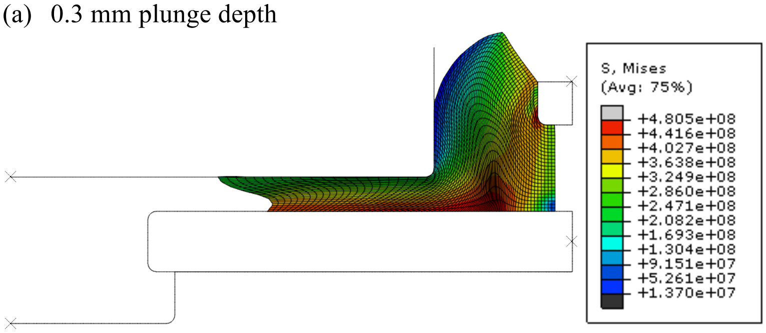

(b) 0.6 mm plunge depth

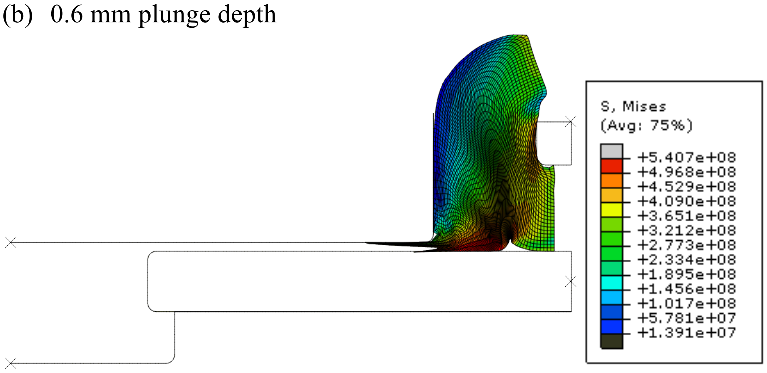

(c) 0.9 mm plunge depth

Figure 32: Stress profile for the second submodel at 0.3, 0.6, and 0.9 mm of plunge depth

5.3.3. Conclusions

From the global model, the following can be concluded. First, at 0.3 mm plunge depth, the aluminum went through the steel hole, touched the bottom of the anvil, and it is ready to form the rest of the mechanical interlocking, head. Second, the formation of the mechanical interlocking is finished at 0.6 mm. In addition, the aluminum detachment under the flash is started at that depth. At 0.9 mm, the head was fully formed. The friction and the plastic deformation increased the temperature in the neck and flash area. **Figure 25** shows magnitude and components of the heat flux vectors, and it can be concluded from the figure that the heat flux in aluminum part under the tool is stronger as the tool progresses. This conclusion is in agreement with the experimental results (thermocouple test). At a 0.6 mm plunge depth, heat flux is directed away from the tool through aluminum towards the holder and the steel under the tool. However, at a 0.9 mm plunge depth, the heat flux is stronger under the tool area. In addition, the distance between the final plunge depth and the steel has critical importance for the quality of the joint. It is desirable that the distance is as big as possible since the strength of the joint relies on it. Thus, the 0.9 plunge depth is not desirable. The second factor that controls the strength of a joint is the quality of the head and that is the focus of the first submodel. When it come to the stress distribution, it is higher in the aluminum contact with the holder, the steel, and the aluminum. The stress concentration in the aluminum work material lowers after the detachment.

The two dimensional model has a critical shortcoming because it is unable to incorporate the tool rotation. Angular velocity has a critical importance for heat generation, since it will yield different outcomes for different values. However, the model represents a quick and a rough estimation of a given design and a set of materials.

From the submodels, for the given conditions, regardless of the mesh quality and the element size, the anvil cavity was not completely filled with aluminum. The entire surface of the topside of aluminum that touches the tool was transformed into the thermo-mechanically affected zone and the depth of the zone is 1/3 of the worksheet thickness. A smaller area of aluminum that was not under the tool was also transformed into the thermo-mechanically affected zone. The total radius of the area is 5.55 mm. In a laboratory or production line, this value will be bigger since the tool also experiences some unwanted vibrations. The aluminum detachment formed closer to the holder and was determined by the head progression, plunge depth, and conditions of the holder. In other words, the detachment formed after the head formed, and it formed closer to the holder. If the holder is not firmly fixed, the detachment will be bigger and longer.

5.4. 3D Model

Modeling the FSF process includes heat transfer generation, large deformations, large strain rates, etc. The two dimensional simulation is a starting point, but it has a serious shortcoming in the friction heat generation aspect since the tool rotation requires an additional dimension to portray the situation accurately. More accurate FEA is possible with a three-dimensional model with the trade off of more computation resources, better hardware and/or more time.

A model of a FSF sample has five domains: a tool, a sample holder, a top workpiece, a bottom workpiece with a hole, and an anvil with a cavity. At this time, for purely computational time frugality, only the top and bottom workpiece were considered deformable. The schematic representation with a cross-section of the model can be seen on **Figure 33**.

For 3D modeling the following elements are appropriate: R3D3 and R3D4 for rigid and C3D8RT for deformable domains (a 3-dimensional 10-nodes modified thermal analysis element). C3D8RT tends not to be stiff enough in bending. Stresses and strains are most accurate in the integration points. The integration point of the element is located in the middle of the element. The reduction integration suffers from numerical difficulty called hourglassing (excessive flexibility). This happens because the element has only one integration point. This can lead to a situation where a distorted element still has zero calculated strain at the integration. This uncontrolled distortion of the mesh, known as the hourglass effect, needs to be corrected. This challenge is especially true for the first order element; thus, multiple layers have to be applied. Second order elements rarely suffer from hourglassing when a second layer is applied. Since C3D8RT is a first order element, the deformable domain was meshed with at least four layers with reasonably fine mesh, and an hourglass control was always applied. ABAQUS provides different types of hourglass control and the appropriate one for this type of model is the relaxed stiffness hourglass control.

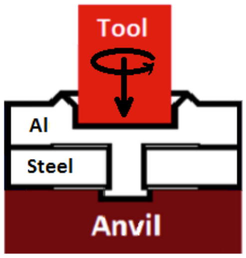

(a) Schematic representation

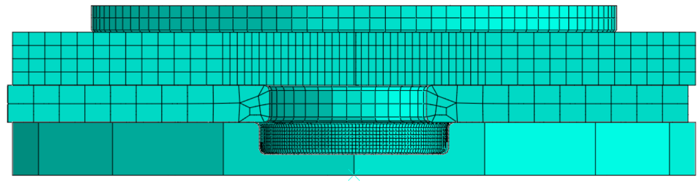

(b) FEA cross-section of the assembly

Figure 33: 3D Model (a schematic representation and a cross-section)

Figure 33 shows a schematic representation of the model as well as a cross-section of the model. The tool, aluminum, steel, and anvil domains are assembled on top of each other respectively. In the model, the steel domain was shifted 0.085 mm from the central axis. This was done to make the model more realistic, since even in the well-controlled laboratory conditions, the domains' alignment will never be perfect.

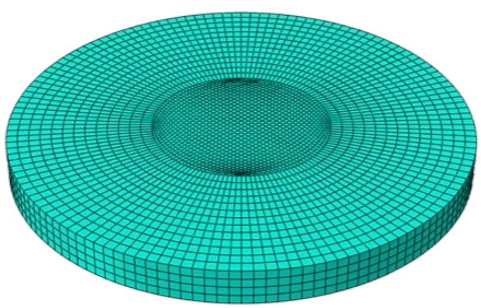

Figure 34: Aluminum domain meshing

The figure shows the aluminum domain. The domain has a partition in the center with a higher mesh density.

As can be seen from

Figure 34, the aluminum domain was partitioned, and the partitioning diameter was 5.0 mm (the dimensions of all four domains are represented in **Table 6**). The quality of the mesh, including the partitioning, is critically important because the generated aluminum mesh needs to follow the cylindrical steel hole and the anvil cavity contour well. A better model would preferably have another partitioning (annulus partitioning cells) such as on **Figure 60**. The result of this approach is that the mesh is much smoother in the neck/head region. The outside edges have the seed size of 0.3 mm, while seeds of the partition are $1.5 \cdot 10^{-4}$ m.

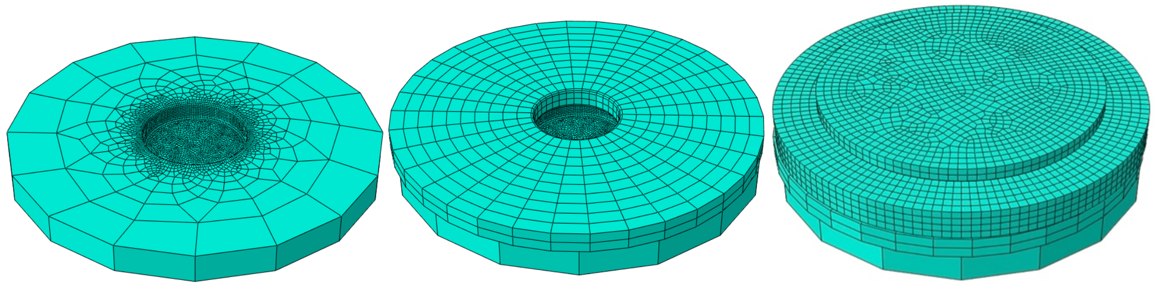

(a) Anvil (b) Steel and anvil (c) Complete Assembly

Figure 35: Meshing of the domains

As with the 2D model, the edges of the steel hole, the tool, and the edges of the anvil cavity were also rounded. The roundup radius for the tool is $4 \cdot 10^{-2}$ mm. For all other edges, the radius is 0.1 mm. **Table 8** shows the mesh characteristics of the entire model. The anvil domain has a higher mesh density around the cavity in order to represent the circular shapes in the most correct way possible. However, the mesh roughness is increasing radially away from that part of the domain. This was done since the outer area of the rigid domain is less important. By increasing the roughness of the mesh, the computation time was shortened and nothing would be lost from the precision of the model.

Table 8: Mesh characteristics of the 3D model

	Nodes	Elements	R3D4	R3D3	C3D8RT
Tool	2663	2680	2642	38	na
Aluminum	15645	12240	na	na	12240
Steel	1428	918	na	na	918
Anvil	4092	4144	4036	108	Na
Total	23828	19982	6678	146	13158

na – non applicable

Table 9: Mesh characteristics of the 3D submodel

	Nodes	Elements
Submodel I	8680	10424
Submodel II	7672	6370

*submodels computed only a part of the aluminum domain. No other domains were considered at this time.

The following table, **Table 10**, displays the values for the mild steel. Unfortunately, at this time, the domain did not contain a plasticity model. In the future, this can be easily improved by adding this information. The Poisson ratio is kept at 0.28, and coefficient of friction between the mild steel and the anvil is 0.57.

Table 10: Mild steel properties used in the 3D simulation [Mousavi 2008]

Temperature [K]	273.15	371.15	474.15	589.15	701.15	844.15	923.15
Thermal conductivity [W/m•K]	34.5	34.5	33.8	31	28.5	26.5	25.8
Heat capacity [J/Kg•K]	470	485	520	560	620	700	760
Density [Kg/m^3]	7800						
Young's modulus [GPa]	207						
Thermal expansion [1/ K]•10^{-5}	1.17						

The Poisson ratio was kept constant at 0.28, and coefficient of friction between the mild steel and the anvil is 0.57.

5.5. Boundary Conditions and Interactions of the 3D Model

The reference points of the two rigid parts were placed on the global vertical axis, which goes through the centers of the model. For the tool, the reference point was on the top, and anvil had it on the bottom. In contrary to the 2D model, the position of the reference points are important, especially for the tool since the reference point has a full kinematic coupling constraint. In other words, the reference point contains the information about the trajectory, time, and the dynamics of the domain. The tool has to follow the boundary conditions of the reference point (2250 RPM and 10 mm/s straight downwards).

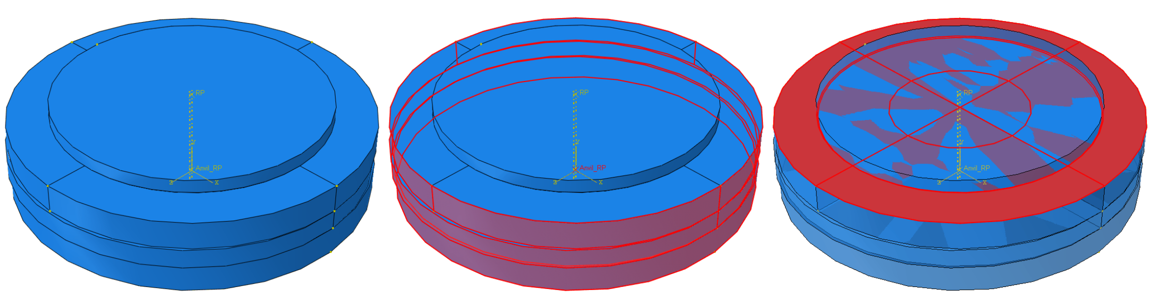

(a) Complete assembly (b) Fixed boundary conditions (c) Aluminum/steel contact surface

Figure 36: Boundary conditions and a couple of contact pairs

Figure 36 shows the 3D assembly with all the domains. The yellow dashed lines that are placed through the assembly are representing the axes. Since the steel is offset, the dashed line on the left represents the vertical axis of the mild steel. The second axis contains the two reference points for the rigid domains. The bottom reference point is also called "Datum csys", which is the beginning of the global cylindrical coordinate system. In the middle of the figure is the assembly with highlighted sides of the aluminum, the steel, and the anvil together with the bottom of the anvil and the anvil's reference point. Those sides and the reference point are fully fixed (no rotations and no translations). The rest of the boundary conditions were kept the same as in the 2D model. The interaction properties between the domains are the same as they are described in section 5.1.1 and 5.1.2. The 3D model has eight defined separate contact surfaces. Those contact surfaces are:

1. Tool, which includes the entire bottom surface of the tool together with the surface of the rounded edge.
2. Top of the Aluminum (outside annulus)
3. Top of the Aluminum (center partition)
4. Bottom of Aluminum, which contains the entire bottom surface of the domain
5. Mild Steel (Bottom), which includes the bottom of the mild steel and the surface of the bottom rounded edge of the steel hole.
6. Anvil (top), which includes the topside of the domain, the top of the cavity, and the surface of the top and bottom rounded edges of the cavity.
7. Aluminum Contact with Anvil, which includes the side of the anvil cavity, the bottom of the cavity, and the rounded edges of the cavity.
8. Aluminum Contact with Steel, which includes the top and the bottom sides of the mild steel domain together with the sides of the steel hole and the surfaces of the rounded edges of the steel hole.

These surfaces were used for defining the interactions between the domains. Since contact pairs are the interaction type that was used in the model, every possible surface-to-surface contact had to be well defined. Otherwise, the software would not compute the missing contact or contacts. For example, if the contact between the aluminum and the anvil is not defined, after the aluminum passes through the steel hole, it will continue through the cavity as well as through the anvil. The software will put both domains in the same space, and disregard the fact that this is physically impossible.

There are six interactions in the model. Every interaction has to define only two surfaces. The following list shows their names. The two numbers that every interaction has corresponds to the contact surface from the previous list.

1. Tool to Aluminum (partition in the center) – contact surfaces: 1 and 3.
2. Tool to Aluminum (outside partition) – contact surfaces: 1 and 2.
3. Aluminum to steel – contact surfaces: 4 and 8.
4. Aluminum to anvil – contact surfaces: 4 and 7.
5. Steel to Anvil – contact surfaces: 5 and 6.
6. Surface film, Aluminum top (only)

The last interaction was explored, but did not yield different results. Potentially, this would be one of the ways to improve the model. At this time, the surface film interaction was suspended. The film condition interactions define heating or cooling, in this case cooling, due to convection by surrounding fluids (air that surround the tool at the top of the aluminum). There are at least two parameters that are needed for this interaction to be fully defined. Those parameters are the sink temperature and the film coefficient. The sink temperature was chosen to be the room temperature, and the film coefficient was kept constant at 30 $W/m^2 \cdot K$. The convection condition was applied to the mesh elements that belong to the faces of the aluminum topside, and only the outside partition since those elements are the only one that will not stay under the tool at any time of the process. The highlighted surfaces in red on the right on **Figure 36** are interactions 1, 2, and 3. In order to have a central partition of the aluminum, the domain had to be initially partitioned in four equal sectors. This is represented by the red cross on the same figure.

5.6. 3D Results

This section reveals the results of the three-dimensional simulation as well as the results of two 3D submodels.

5.6.1. Global Model Results

The following is the description of those special areas of interest and some important facts about the global 3D model such as steel deformation, followed by temperature and strain results. All the temperatures are in kelvin.

5.6.1.1. Head and Neck

As the aluminum progresses through the steel hole, the mild steel and the anvil have thermal influence on the aluminum.

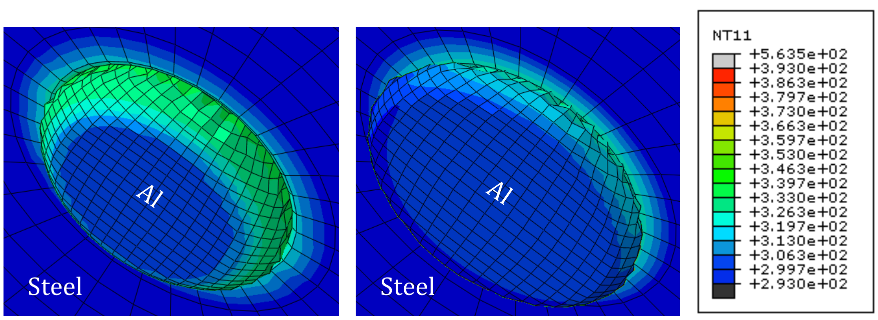

(a) 0.6 mm plunge depth (b) 0.84 mm plunge depth

Figure 37: Head progression

The picture shows the temperature distribution of the steel and the Al head at 0.6 and 0.84 mm plunge depth.

They are performing as heat sinks. This is important, and it will be even more important if a more conductive material was used instead of steel for the anvil (such as copper). This also shows what kind of influence a deeper cavity would have on the aluminum that is going through the space. **Figure 37** shows the aluminum progression through the steel hole and touching the bottom of the anvil cavity. For this outcome specifically, in order to make the result more obvious, the anvil had the increased value of the heat capacitance.

Figure 38 shows that there is a significant aluminum mesh distortion, which led to inaccuracies and inconsistencies and divergence of the computation. This can be avoided and the description of that can be seen in section 5.7.1. The upper edge of the steel hole is particularly problematic when it comes to the development of the mesh inconsistencies.

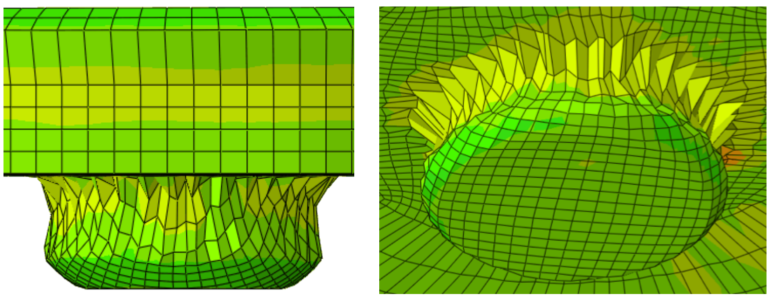

(a) Aluminum neck (b) Another view of the neck

Figure 38: Distortion of the mesh in the neck region

The picture shows temperature distribution of the aluminum head at 0.5 and 0.84 mm plunge depth. The legend is the same as in **Figure 39**

5.6.1.2. Flash and Aluminum Detachment

The maximum flash height is 1.13 mm (measured from the top of the aluminum to the top of the flash at 0.8 plunge depth). The following figure represents a cross section through the center of the joint where the shape, size, and the temperature distribution of the flash and the aluminum detachment can be seen.

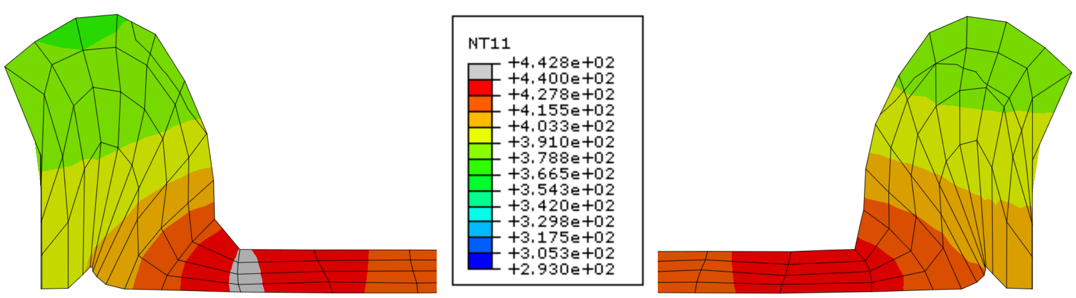

Figure 39: Aluminum detachment and flash at 0.8 mm plunge depth

The next figure, **Figure 40**, shows the aluminum detachments. The height on the plunge depth of 0.80 is in the range of 0.177 to 0.2 mm. The detachment formed around the joint at the distance of 6.1 mm from the center of the joint. This value was measured at the maximum height of the detachment (the peak).

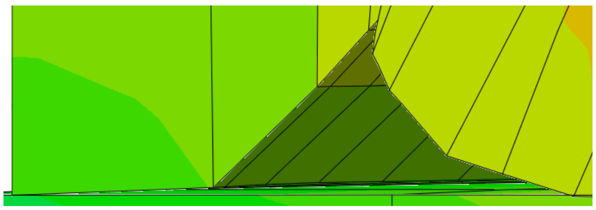

(a) Aluminum detachment on the left

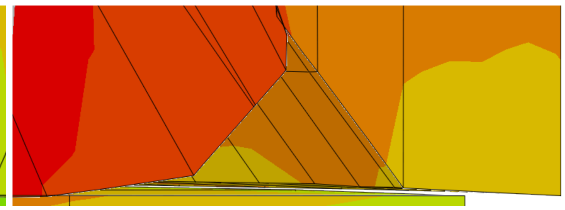

(b) Aluminum detachment on the right

Figure 40: Shape of the aluminum detachment

The picture shows the temperature distribution of the steel at 0.80 mm plunge depth. The legend is the same as in **Figure 39**. The steel axis is shifted to the left, and that has an influence on the temperature distribution of the aluminum detachment.

5.6.1.3. Separation after the Contact

As was described in Chapter 5.2, the contact property between the tool and the central aluminum partition was setup so the "separation after the contact" is not allowed. If the separation is allowed, the model yields inaccurate results in the center of the topside of the aluminum, and this is represented with **Figure 41**. For this simulation, the steel work material was rigid (the mild steel and the anvil was one joined domain). The final plunge depth was 0.9 mm.

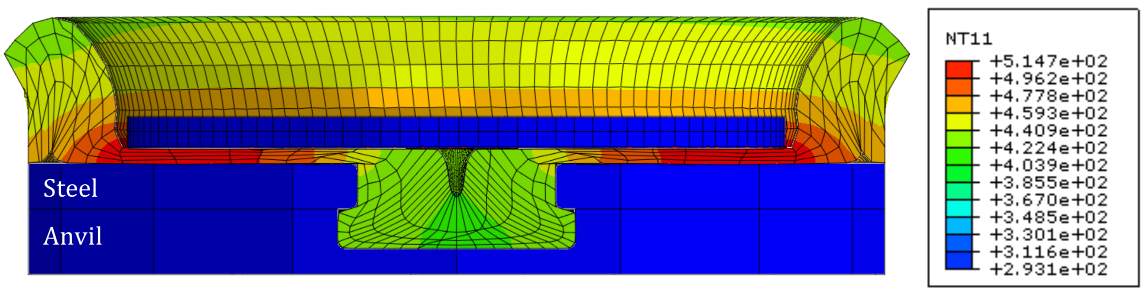

Figure 41: Temperature distribution (no separation after the contact)
The tool and the mild steel/anvil are rigid domains, and their color is blue.

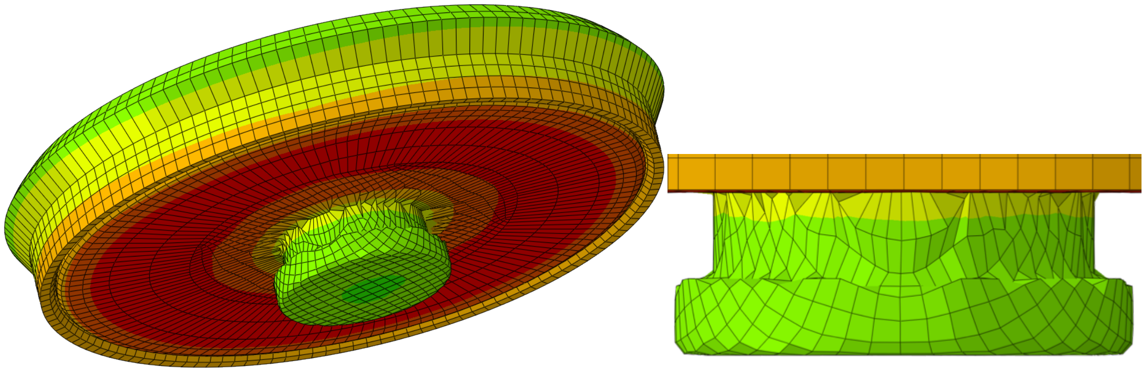

(a) Bottom Look on the Aluminum (b) Head and Neck (aluminum only)

Figure 42: Neck and head (with no contact after the separation)

Closer looks of the head/neck part of the sample on 0.9 mm plunge depth that could detach itself from the tool.

With the separation option, the model develops fewer inconsistencies around the steel-hole edges and the head and the neck formation are significantly better. The computation went further and with less mesh distortion. The 2D and 3D model have different approaches to the "No separation after contact" option. In the 2D model, since it is an axisymmetric model, the option has to be applied on the tool/aluminum contact surfaces. The model also must have a boundary condition on the axis that prohibits aluminum nodes from moving horizontally (freely moving vertically only). In the 3D model, which is not an axisymmetric model, the separation option is applied only between the tool and the central partition of the aluminum domain. **Figure 43** shows the neck/head area in the 3D model. There is no void in the middle of the neck but the outside shape suffers greatly, and the error type is different.

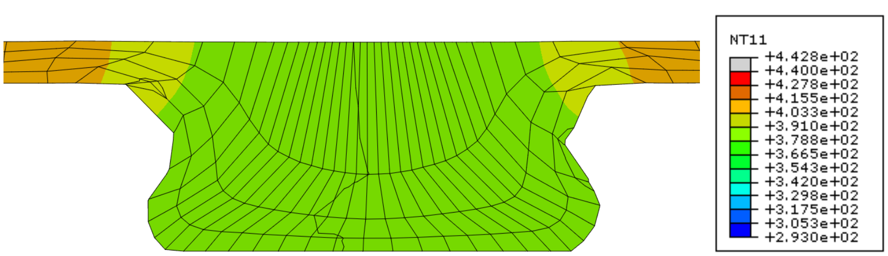

Figure 43: Neck and head at 0.8 mm plunge depth (with "separation after the contact")

5.6.1.4. Steel Behavior

It was empirically observed that the bottom work material could be deformed above the edge of the anvil cavity. This highly depends on the design and materials used. Here is an example of a simulation that contained Johnson-Cook plasticity model information for mild steel that shows that behavior. The Johnson-Cook information is shown in **Table 11**. For this simulation, the steel domain had to be better meshed (a higher mesh density). This simulation was explored during the model development, "separation after the contact" option was not used, and the thermal conductivity had the enlarged value.

Table 11: Johnson-Cook constrains for mild steel [Mousavi 2008]

Symbol [Unit]	A [MPa]	B [MPa]	n	m	T_{melt} [K]	$T_{transition}$ [K]	C	$\dot{\varepsilon}_0[s^{-1}]$
Value	310	350	0.3	0.5	1803.15	293.15	0.02	1

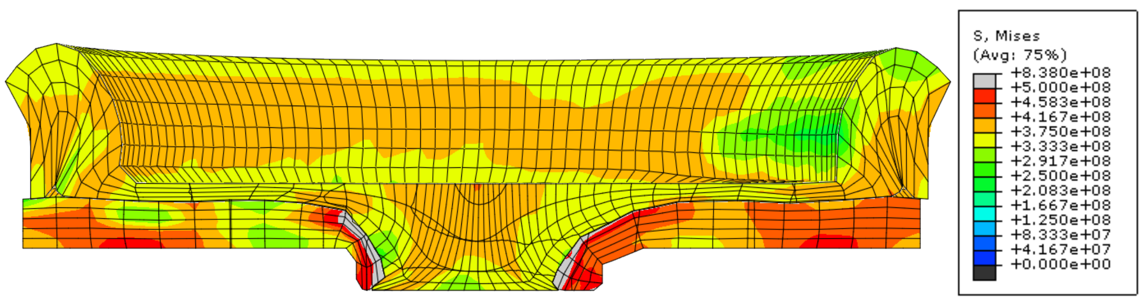

Figure 44: Steel Deformation and Stress Distribution at 0.9 mm Plunge Depth

The figure shows stress distribution of both deformable domains.

Figure 44 shows aluminum and steel after the tool went 0.9 mm deep into the workpiece. As before, the mild steel domain is shifted to the left from the global vertical axis. The steel collapsed into the cavity and it prevented the proper aluminum head and neck formation. The steel domain also has a partition with a radius of 2 mm. However, since an axial shift was performed, the mesh did not correspond properly and equally on the entire edge of the cavity of the anvil. The error was more severe on the right side of the steel hole (**Figure 44**). The error was relatively small since it affected only 14% of the parameter that touched the edge of the cavity. This can be easily be corrected by meshing the partition with smaller elements (a higher mesh density). In **Figure 45** the pressure profile for the two deformable domains can be seen.

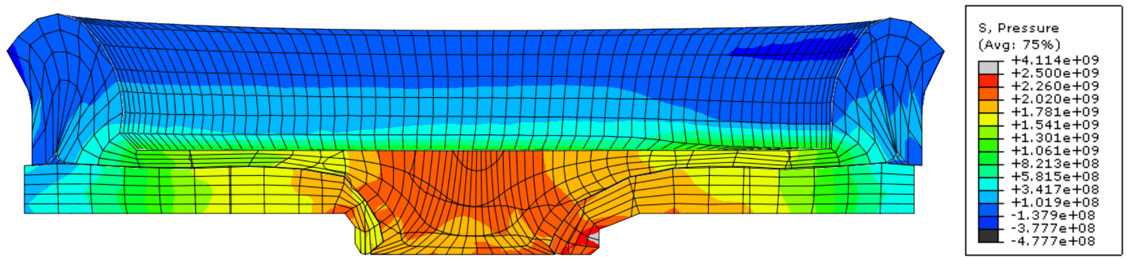

Figure 45: Pressure profile for aluminum and steel

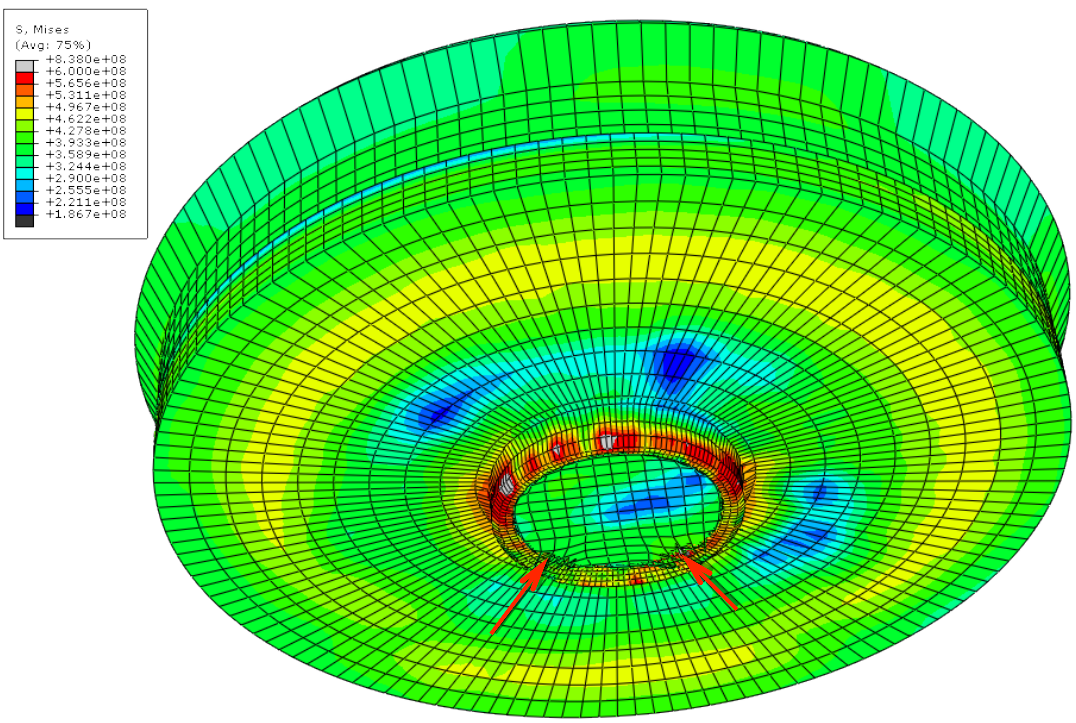

Figure 46: Bottom view of the steel collapse and the aluminum head

The steel domain axis is shifted downwards. The aluminum head has two small distortion areas (red arrows). The distortions did not stop the computation progress. By increasing the mesh element density, the distortions should wane.

Figures 47 and 48 show a closer view of the model without the Johnson-Cook parameters. The thermal contact conductivity was enlarged to make the effect of heating of the steel more obvious.

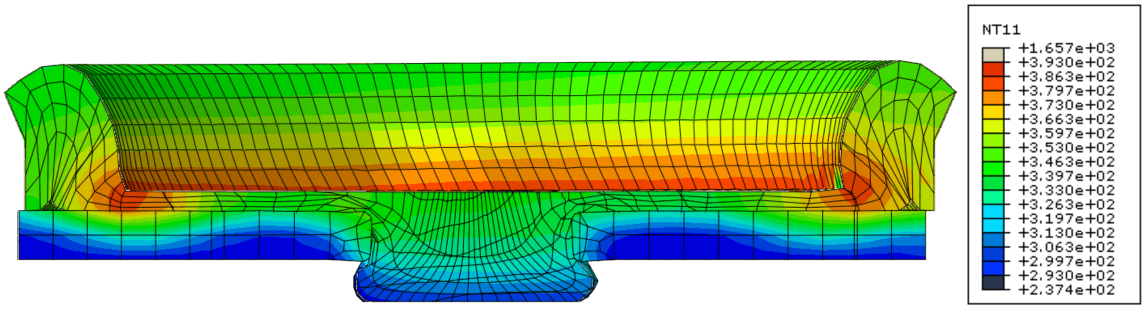

0.84 mm plunge depth

Figure 47: Temperature distribution of the steel and aluminum (enlarged contact conductivity)

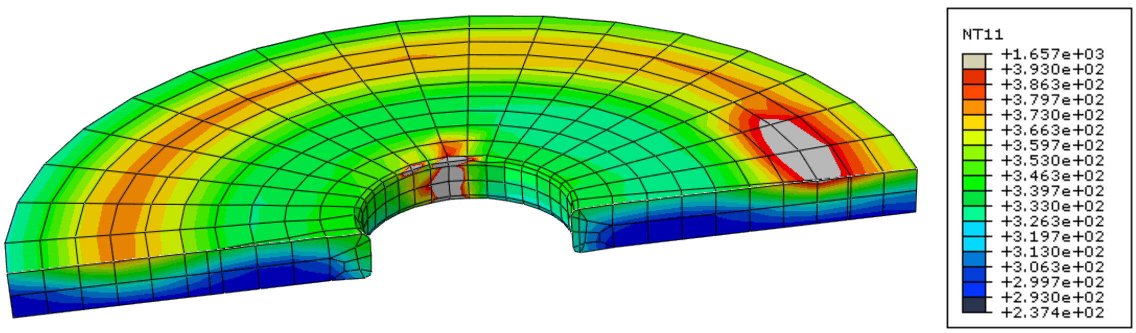

Figure 48: Temperature distribution of steel (enlarged contact conductivity)

This half of the steel domain is the same part as the one in the previous figure. It shows temperature distribution of the domain at 0.84 mm plunge depth.

5.6.1.5. Temperature and Plastic Strain Distribution

Figure 49 and **Figure 50** show the aluminum and the steel domain cross-sectioned at different plunge depth points. At a plunge depth of 0.35 mm, aluminum detachment started to occur. At 0.5 mm, the tool progressed enough so that the neck formation finished and the head formation started.

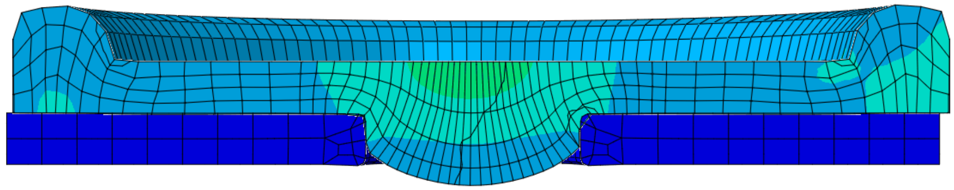

(a) 0.3 mm plunge depth

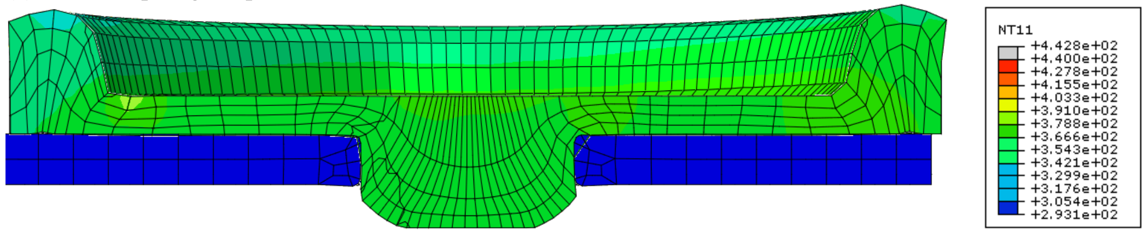

(b) 0.5 mm plunge depth

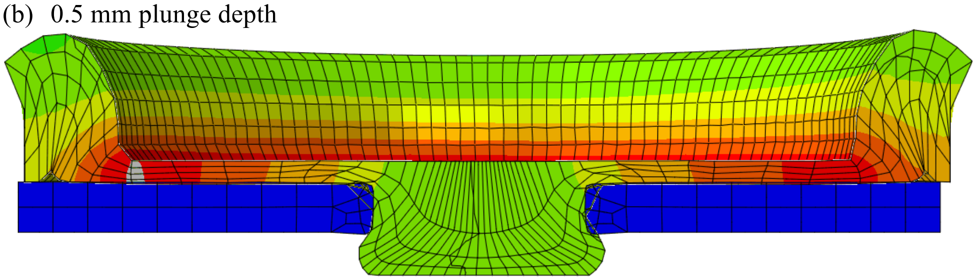

(c) 0.8 mm plunge depth

Figure 49: Temperature distribution of the aluminum and the steel

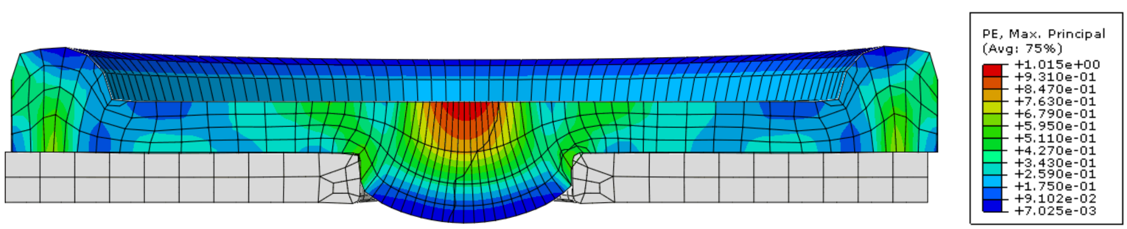

(a) 0.3 mm plunge depth

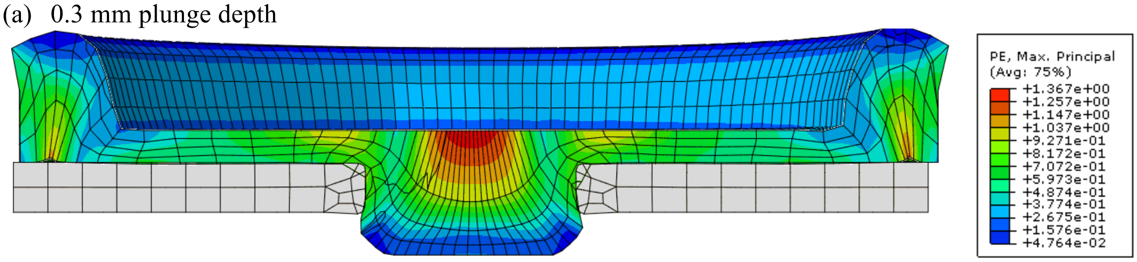

(b) 0.6 mm plunge depth

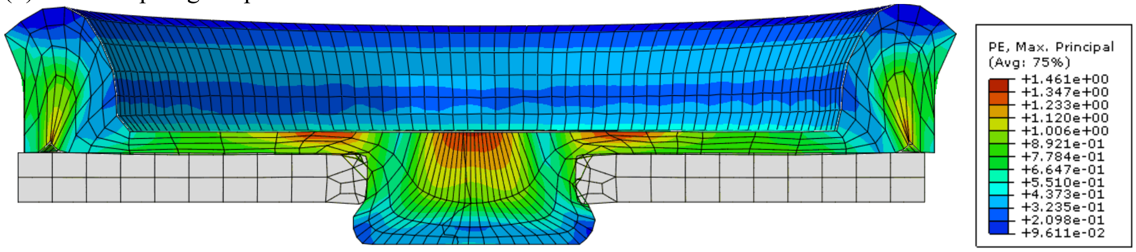

(c) 0.8 mm plunge depth

Figure 50: Plastic Strain of the aluminum and the steel

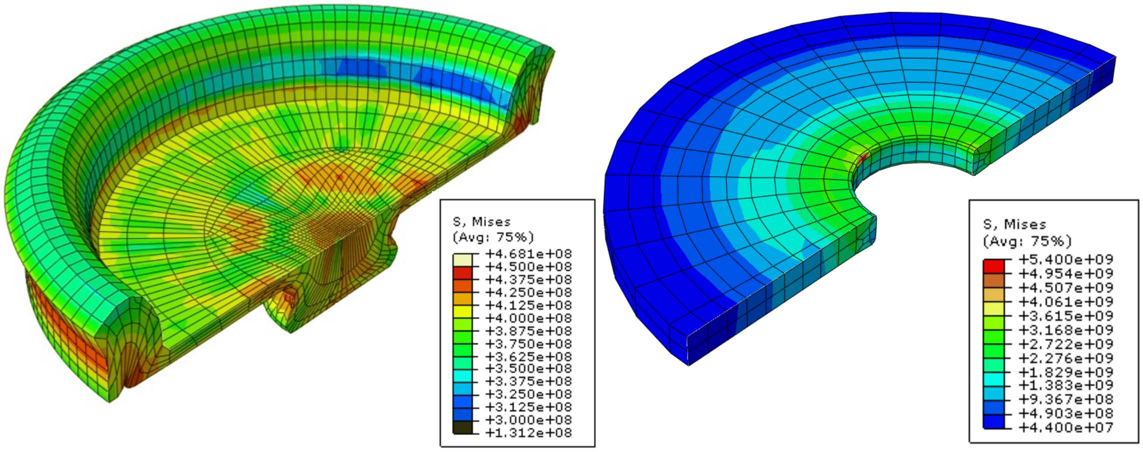

(a) Aluminum (b) Steel

Figure 51: Stress in the work materials at 0.8 mm plunge depth

Figure 51 shows the aluminum and steel domain at plunge depth of 0.8 mm. There is an important difference between the two domains. The steel work material had about a ten times bigger stress due to the positive influence of the temperature on the stress of the aluminum. The highest stress value for the aluminum was on the upper rim of the steel hole.

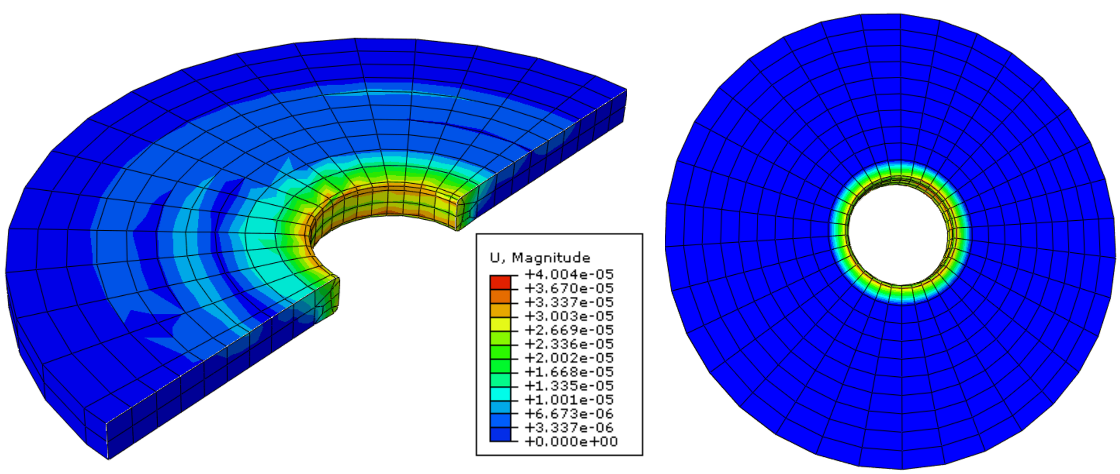

(a) Top side of the steel (b) Bottom view of the steel

Figure 52: Displacement in steel at 0.8 mm plunge depth

Even though the steel did not deform much, there was a small displacement in the material. While the top surface experienced some small but broad displacement, the bottom side experienced the effect only in the part that was not contacting the anvil (**Figure 52**).

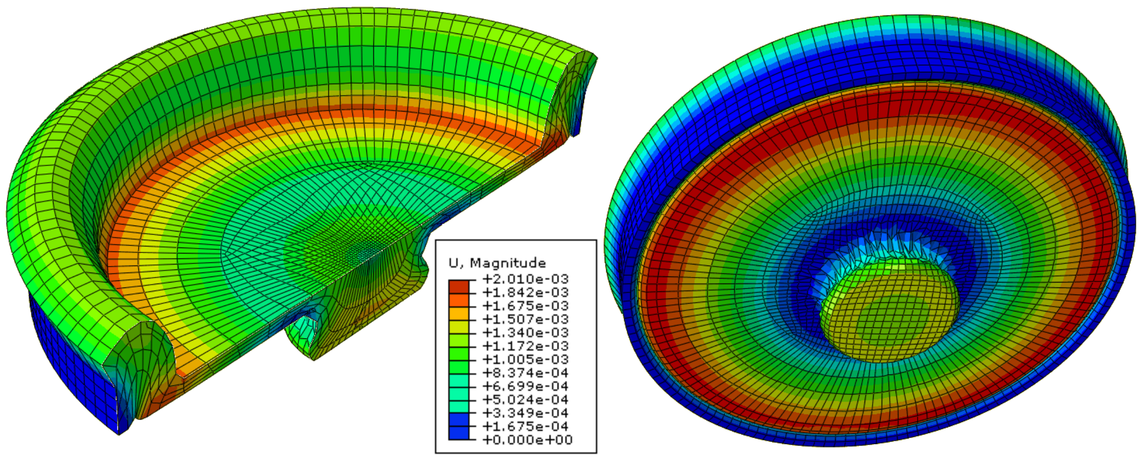

(a) Top side of the aluminum (b) Bottom view of the aluminum

Figure 53: Displacement in aluminum at 0.8 mm plunge depth

An important outcome from **Figure 53** is that the displacement increased radially and declined at the aluminum detachment. There was a lot of displacement in the neck as was expected. However, in the aluminum part that was under the tool, the displacement was the smallest in the bottom part of the domain close to the steel hole.

5.6.2. 3D Submodels

There are two submodels that were computed, and they both considered only aluminum. The first submodel represented only one 45° sector of the aluminum domain, and the second submodel represented only the center part of that domain. The part of the aluminum that was used for the second submodel had a radius of 2.3 mm in a non-deformed state. The mesh characteristics of the submodels can be seen in **Table 9**.

5.6.2.1. 3D Submodel I

The main purpose of the first submodel was to closely examine all the significant elements of the joint with a finer mesh. The next three figures show the simulation outcome.

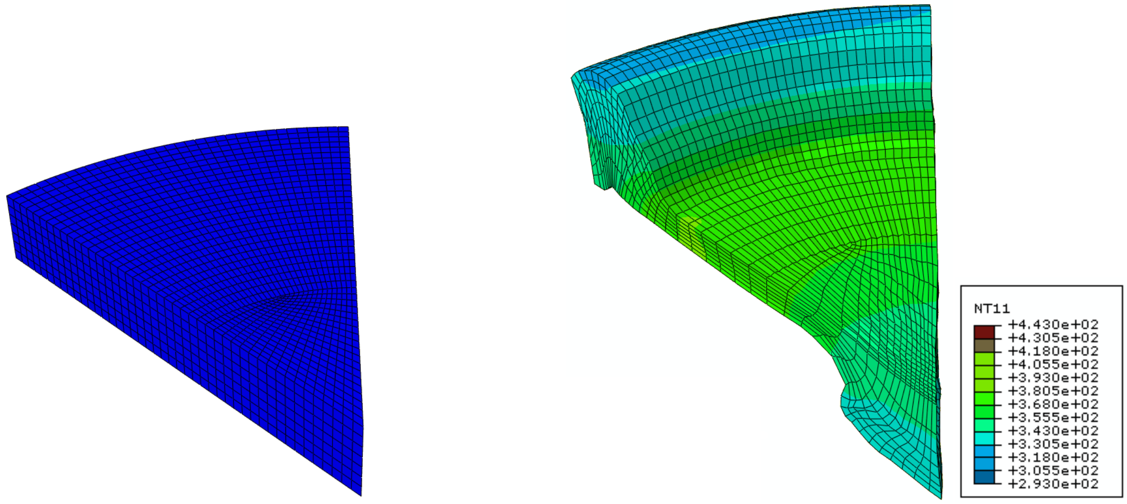

(a) The sector on the beginning (0 mm plunge depth)   (b) End of the simulation (0.8 mm plunge depth).

Figure 54: 3D Submodel I – a top view (material progression and temperature distribution)

Figure 54 shows the sector that is not deformed and the same sector on 0.8 mm plunge depth.

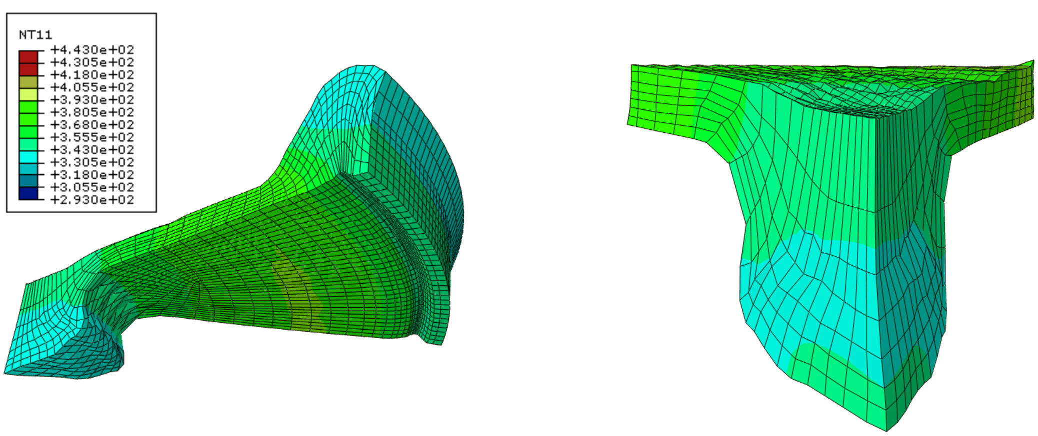

(a) Another look on the bottom of the submodel   b) Closer look on the head and neck area

Figure 55: 3D Submodel I – a bottom view and a view of the head at 0.8 mm plunge depth (Temperature Distribution)

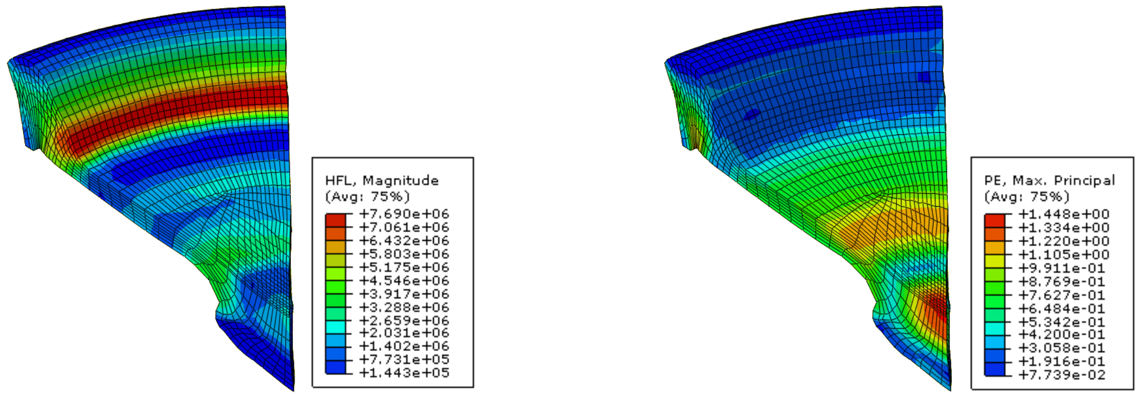

(a) Heat flux (b) Principle Plastic Strain

Figure 56: 3D Submodel I – Cross section at 0.8 mm depth (heat flux and principle plastic strain)

HFL on **Figure 56** a) stands for the current magnitude of the heat flux. Since all the mesh elements had positive values, it indicated that heat was flowing into the elements. Figure 59 b) shows plastic strain, which is high in the coin section and in the aluminum detachment zone. The top of the center of the aluminum domain had a higher error since the material could not detach itself from the tool.

5.6.2.2. 3D Submodel II

The second submodel was focused on the central part of the domain, the neck and the head. The radius of the submodeled part was 2.3 mm, and the radius of the partition in the global model was 2.5 mm. There were two reasons for choosing a smaller part of the partition. The first reason, and the main reason, was to avoid complications due to the differences in property values of the partitions in the global model. The second was that there was enough material for the submodel to achieve the given task.

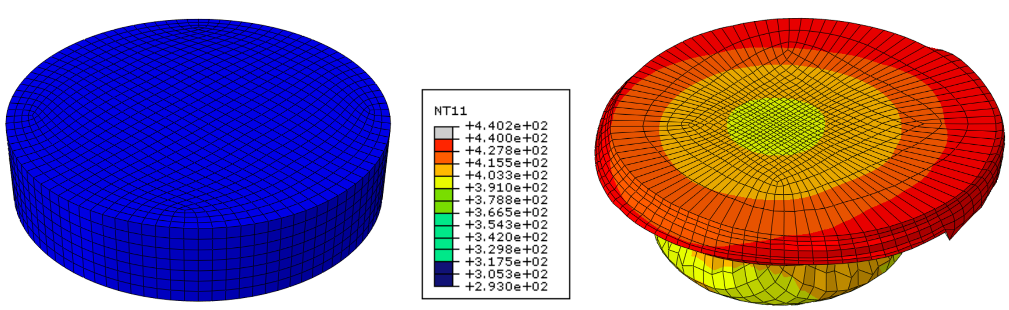

(a) The submodel on the start (0 mm plunge depth) (b) End of the simulation (8 mm plunge depth).

Figure 57: 3D Submodel II – Top Surface (Temperature Distribution)

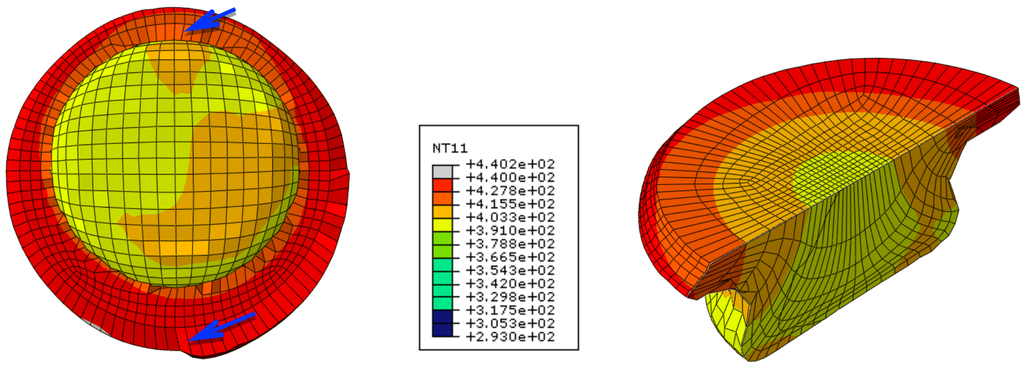

(a) Bottom view of the submodel at 0.8 mm plunge depth (b) Cross-section at 0.8 mm plunge depth

Figure 58: 3D Submodel II – a bottom and a cross-section view (Temperature Distribution)

As in the first submodel, a substantial amount of strain occurred in the top center of the aluminum domain, and it can be seen on **Figure 59** b). It was influenced by the "no separation after the contact" option. The blue arrows on **Figure 58** b) shows inconsistencies in the simulation due to the partitioning technique.

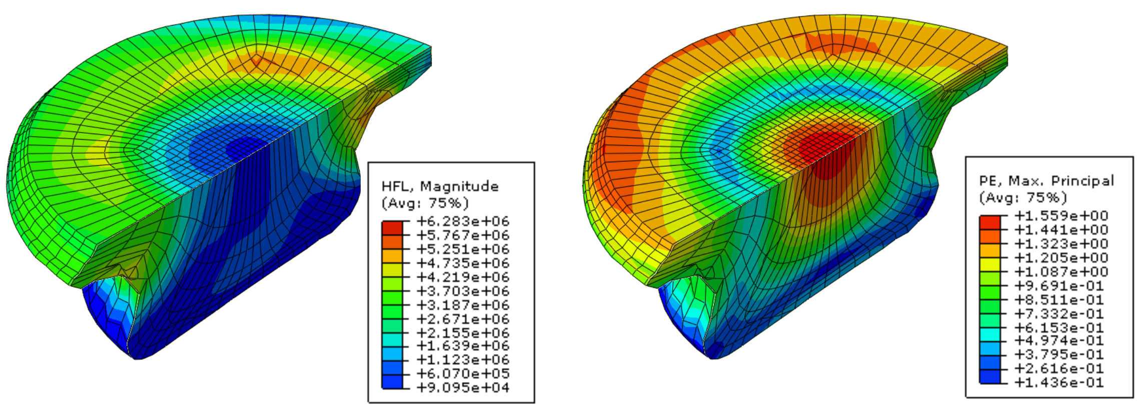

(a) The submodel on the start (0 mm plunge depth) (b) End of the simulation (0.8 mm plunge depth).

Figure 59: 3D Submodel II – cross-section (heat flux and principle plastic strain)

From the submodels, it can be concluded that because the steel was offset, the aluminum did not have a symmetric heat flux and temperature distribution throughout the neck and the head region. The hypothesis was that the steel or the tool offset would affect the material flow into the cavity, which was observed in laboratory conditions. The head shape probably would not have the desirable shape at the end of the stirring.

The second model shows, even in the coin section, there was non-symmetry in the aluminum displacement because the steel domain was not perfectly centered.

5.6.3. 3D Modeling Conclusions

From the 3D global model and the submodels, the following can be concluded. The simulation was most likely to stop prematurely due to a mesh distortion on the corner of the aluminum cavity or the upper corner of the steel hole. The mesh would be highly distorted and the temperature of the distorted area increases to the point that it does not have any physical meaning. The quality of the neck/head region was highly dependent on how the mesh behaves on the upper edge of the steel hole. As a result of that, the edge dictated the mesh characteristics such as size of the element, partition, distortion control, etc.

The upper edge of the steel hole had significant influence on the aluminum displacement. The aluminum in the thermo-mechanically affected zone was easily displaced, and it tended to move in two different directions: towards the neck or away from the neck area. While the aluminum was flowing, the aluminum on the bottom side, especially closer to the steel hole, had the least displacement.

The center of the topside of the aluminum developed an unrealistic cavity. In order to correct that, the “Separation after the contact” option could be applied. This option had a significant influence on the top center of the aluminum domain, the area above the neck. In the 2D model, the option worked correctly. However in the 3D model, the situation was different. Without the option, the aluminum formed an unrealistic deep cavity in that region. With the option, the cavity did not form, but the shape of the head and the neck suffered. In addition, with the option, there was a higher concentration of plastic strain in the central topside of the aluminum domain. Even with the option, there was a very small dip in the area, Figure 55 b), which has realistic characteristics.

The bottom material, steel, experienced significant stress and heat input in the area around the steel hole, especially the part that was not supported by the anvil.

The anvil had an important heat sink characteristics and this was also observed in the laboratory experiments.

The aluminum detachment representation can be improved by increasing the outside diameter of the aluminum and the steel domain. In combination with a holder and the bigger diameter, the model would improve the temperature and the stress profile in the aluminum detachment and in the flash region.

The maximum temperature of the system during the process was in the neck region before the tool reaches 0.45 mm depth. At this point, the temperature of the system was 95°C. After this point, the maximum temperature of the global model was on the rim of the tool, and at a 0.8 mm plunge depth, the maximum temperature was 169°C. The temperature situation was slightly different with the submodels. The first submodel shows that the maximum temperature occured at the entrance of the steel hole. For most of the process, the maximum temperature was in the aluminum detachment zone. At the 0.8 mm plunge depth, the temperature was 192°C.

Since the steel was off-centered, the temperature was not equal around the circumference of the flash. The average temperature of the top of the flash was between 105°C and 115°C (at the 0.8 mm plunge depth). The side of the aluminum domain closer to the axis of the steel hole had a minimum temperature. In other words, if the steel was moved towards the west, the eastern side of the flash would get a slightly more amount of the heat.

From the global model it can be concluded that, because the steel was offset, the aluminum did not have symmetric heat flux and the temperature distribution through the neck and head region was asymmetric as well. The minimum temperature in the entire coin was always in the center, and at a 0.8 mm plunge depth, the temperature was 105°C. “Separation after the contact” dictated the size of the error of the temperature value in that region.

The temperature range on the bottom of the coin, neck excluded, was from 117°C to 173°C according to the global model at a 0.8 mm plunge depth. However, the temperature range was different in the first submodel. The submodel had a higher mesh density, and that resulted in more precise outcomes. The temperature minimum was 82°C, and it increased radially away from the center. The maximum temperature on the bottom of the aluminum coin was 113°C.

The coin temperature was not very different between the top and the bottom surfaces. The biggest temperature difference between the two surfaces was about 30°C throughout the tooling time.

From the thermocouple test, one of the conclusions was that the temperature inside of the core was higher than on the edge of the core. Unfortunately, this was not seen in the results of the 3D model.

5.7. Modeling Improvements

A FSF sample experiences extreme nonlinear deformations. The model is most likely to fail in the neck region and at the edge of the tooling cavity. For a plunge depth of 0.9 mm on an aluminum coupon of 1.0 mm, the model has higher chances to develop inconsistencies as the tool progresses in the last quarter of the plunging. The following propositions are valid for 2D as well as for 3D models. In order to improve the situation, the following are suggestions.

5.7.1. Meshing Improvements

Mesh is crucial to the analysis and there could be a few ways to improve the situation. An example of that can be seen on **Figure 60**.

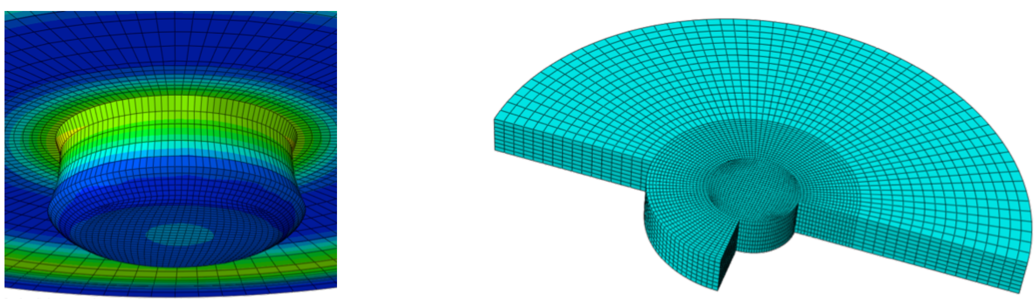

(a) Aluminum neck (b) Aluminum

Figure 60: Aluminum mesh with additional segmentation

On the left, a closer look on the neck and the forming head. On the right, this is an aluminum domain that has an extra annulus partition.

First, the domains could have a higher mesh density. Next, the aluminum mesh can be partitioned in more annulus cells, especially if a deeper plunge depth is needed. The quality of the mesh in the neck/head area is better when compared to the mesh with just a single partitioning. The result of that approach is that the mesh is much smoother in the neck/head region. Another mesh partition of the top workpiece could improve the model if it is placed in the area where the rim of the tool is in contact with the aluminum surface. The disadvantage of the solution is that the computational time cost is higher.

5.7.2. Zinc Layer

Modeling of the zinc layer was explored. The zinc layer had a significant influence on the strength of the joints since it forms a brazed layer. This is important information, and a model should incorporate the layer. The thickness of the coating is significantly different from any other domain thickness. For the case of GMW2 steel, the thickness of the zinc layer is between 30 and 50 μm. For this type of modeling, cohesive elements are appropriate and it can be used for a two-dimensional (COH2D4), a three-dimensional analyses (COH3D8), and for an axisymmetric analyses (COHAX4). These elements are designed to bond two different domains. Frequently, the cohesive elements completely degrade in tension or shear because of the deformation. Subsequently, the components that are initially bonded together by cohesive elements may contact each other. Therefore, the cohesive approach is appropriate for brazing and that includes the failures due to the plunging or a lap shear testing. ABAQUS allows an appropriate response for cohesive failure, which is structural failure of the adhesive. For this type of failure, the adhesive remains on both substrate surfaces, but the two items separate under load.

However, after applying the method into the model, the complexity and computational time was significantly enlarged. In the end, the cohesive approach had to be rejected.

5.7.3. Deformable Domains

In the current model, the tool and the anvil are rigid. Also, there is no holder information added at the moment. Even though these components of the system do not plastically deform, they undergo a small elastic deformation, which ultimately has an influence on the two coupons. A change from rigid to deformable bodies increases the accuracy of the model. This is becoming a more realistic option because of the technological improvement in computation and FEA code.

5.7.4. Parameters to Improve

As was stated before in section 5.1.2, stick and slip conditions are very important for the accuracy of the model since they directly affect the heat generation and the mesh. The empirical data for this is still not complete. Therefore, this is a challenge for the model. After the development of the model, the final adjustment for a set of materials is needed for the two values, especially the elastic slip value.

Another way to improve the model would be to add more detailed data about the conductance. At this time, the value was added for the clearance dependency only. The conductance has two values, where the second value is zero where the surfaces are separated by a distance of 0.1 mm (such as in the aluminum detachment zone). Perhaps, this could be improved by more data points and by adding information about the pressure dependency of the parameter.

Next is the thermal contact conductance. At this time, the heat generation was defined in all the interactions, including the aluminum/tool contact. In this particular interaction, the top of the aluminum is the slave surface, and the friction of converted heat distributed to the slave surface is 0.837. In other words, the heat that is generated by the tool stirring on top of the aluminum is delivered into the two domains differently. The majority of the heat from the stirring, 83.7%, was delivered to the aluminum. The reason why the heat was not separated evenly between the two domains is that the two materials have different values for the thermal conductance. Thus, the heat partition is given by the ratio of the material thermal conductance and the sum of the conductances. Unfortunately, the software allows a single value only, and it has to be a constant during the process. Since the conductance is a variant, this error is unavoidable at the moment. However, perhaps, the value can be adjusted more appropriately in another way. One way to do the adjustments is to divide the plunging step into multiple steps that correspond to the thermal contact conductance changes more appropriately.

6. Experimental Validation

An experiment was conducted to validate the models. The work material, process parameters, and dimensions were the same as was stated in Section 3.4. The experiment was conducted at the University of Hawaii at Manoa. Another test was initially planned as well for the model validation, a depth test. This test would have all the materials, dimensions, conditions, and process parameter as was in the FSF model. The depth test is a good way to compare the aluminum and the steel progression during the tooling stage.

6.1. Infrared Camera Test

Figure 61 a) shows views of the FSF setup through the camera, and the temperature profile of a flash. There are two views of the top of the joint right after the tool retracted.

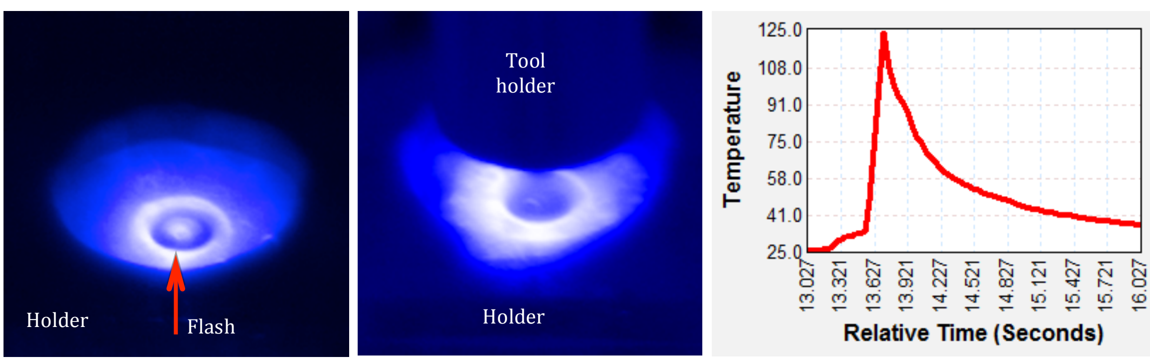

(a) Top of a sample (b) Usual view of a sample (c) Flash temperature

Figure 61: Thermal profile given by the infrared camera

On the left is a view of the stirred region surrounded by the edge of the holder hole after 1.2 seconds of the tool retraction. At this moment, the maximum temperature was the temperature of the flash, and it is 62°C. The red arrow points on the pixel from where the information was collected. In the middle, (b), is the usual view of the top of the joint. The temperature of the bottom of the aluminum cavity is uniformly distributed. On the right is the temperature profile of the flash (the data was taken on the spot that is shown by the red arrow).

The following is the explanation for the graphic on **Figure 61** c). On the 13th second of the procedure, the tool touched the surface of the aluminum (the true beginning of the forming procedure). The first increase in temperature is due to increase of the tool temperature since the tool and the tool holder were blocking the line of sight of the top of the sample. The next increase started 0.6 seconds after the beginning of the forming procedure. At that moment, the tool stopped stirring and it started to retract. As the tool was retracting, the camera was able to record the temperature of the aluminum surface. This is represented as the rapid temperature increase, since the tool started to reveal the top of the joint. The profile recorded the maximum temperature of 123°C, and it was on the top of the flash. It is noteworthy that the center of the joint had an elevated temperature. The temperature profile of the aluminum area that experienced stirring (the aluminum under the tool) had a local minimum in the middle of the radius. The maximum recorded temperature of the center was 88°C. As expected, the maximum temperature decreased radially away from the flash.

Most of the samples did not have the temperature distribution that was shown on **Figure 61** a). **Figure 61** b) shows the typical infrared outcome of a FSF joint. The cavity that was left from the tooling usually had a uniform temperature after the tool retracts.

Table 12: Temperature of the models and submodels at 0.8 mm plunge depth

	Flash	Al. Detachment	Coin	Head (C)	Head (S)	Center	Rim
2D Model	*612	328	318	299	295	299	668
2D Submodel I			310	293	293		
2D Submodel II	367	305	310				
3D Model	378-388	406-416	431-442	380	380-388	378	431-442
3D Submodel I	330	350	340-378	341	341	347	377
3D Submodel II				402	402	402	

All the temperatures are in kelvin. The aluminum detachment temperature was measured on the peak of the feature. The coin temperature was measured between the steel and aluminum, right above the edge of the aluminum cavity. Head (c) refers to the bottom center of the head. Head (s) is the temperature of the side of the head. The temperature of the top center of the aluminum is labeled as center. Rim refers to the rim of the aluminum cavity.

*The mesh element that is on the summit of the flash has a temperature range from 400 to 612.

The CNC machine could not perform the same plunging speed as was entered in the model. The model had a speed of 10 mm/s, and the machine could perform a maximum 1.66 mm/s. This significant difference in the plunging speed is expected to cause a difference in heat generation. The slower speed means that the tool has a longer stirring time, which creates higher temperatures. Unfortunately, the infrared camera reported lower temperatures at the center of the aluminum than the model reported. The heat generation should be higher. **Table 12** shows all the temperature outcomes of the 2D and 3D models. From the table and from the depth test, the conclusion is that the 3D model is the closest temperature representation of the experimental results.

Since at this time there is no other FSF model from other researchers that can be compared with this 3D model, another simulation needs to be used for the assessment from the closest joining process, FSW. In Schmidt and Hattel 2004 study, the researchers revealed a fully coupled thermo-mechanical three-dimensional FEA model that was done in ABAQUS/Explicit by using the arbitrary Lagrangian–Eulerian formulation and the Johnson-Cook plasticity model. The temperature analysis indicates higher temperatures than in the 3D FSF model. This is expected due to longer stirring time of 10 seconds. The FSF model considered only a stirring time of 80 milliseconds. More importantly, the Schmidt and Hattel came to an important conclusion that the heat generation is primarily caused by plastic dissipation.

7. Conclusions and Future Work

7.1. Conclusions

In this research, the numerical modeling of the FSF process was investigated. The FSF joining method demonstrated joining dissimilar materials potential. In order to get better insight into the material progression during the process, a depth test was conducted together with two temperature measurement tests. The temperature measurements demonstrated the temperature gradient on the boundary between the aluminum and the steel, and the infrared camera captured the temperature situation of the top of the joint right after the tool started retracting. The data collected from the tests was used for the FEA simulation development and for the confirmation.

Two different models were developed. The first model was a two dimensional model that can be used for a quick and rough determination of the basic FSF parameters. The model had two submodels focusing on areas that were found particularly important, which were the neck/head for one submodel, and aluminum detachment, flash, and the edge of the aluminum cavity for the second submodel. The next model was a three dimensional model, which also had two submodels. This unique simulation gave a deeper understanding of the material, temperature, and stress progression throughout the joining procedure.

7.1.1. Thermal analysis

From the thermal analysis, it can be concluded that the temperature was decreasing radially away from the neck of the joint between the two workpieces. The temperature was higher with the thinner aluminum coupons since the stirring tool was closer to the steel and the zinc layer. The infrared camera revealed, after the tool retracted, that the highest temperature of the surface of the top workpieces was located on the flash of the joint. The infrared camera also revealed that at that moment the temperature on the bottom of the aluminum cavity is lower than the flash.

7.1.2. Depth Tests

The depth test revealed aluminum progression during the FSF procedure. A special focus was on the area such as the neck and the head development, the thermo-mechanical affected and the heat affected zone, material movement under the tool, shape of the aluminum cavity, and the flash progression. As the tooling progresses, aluminum that was close to the steel hole entered the hole and filled out the neck space. Since the steel-hole setup the boundary conditions for the flow, the aluminum continued in the same manner towards the bottom of the anvil cavity after exiting the steel hole. Once the aluminum made full contact with the anvil, it flowed horizontality in the cavity space. At the optimal plunge depth, the head fully formed and the aluminum stopped flowing into the neck/head area. From that moment, aluminum under the tool flowed away from the center of the joint since the neck/head region was filled out. After passing the tool rim, the aluminum flowed upwards. This caused aluminum detachment and zinc buildup. The detachment happened around the same time that the neck and head filled out. Flash was an aluminum part that escaped the tool stirring located on the side of the aluminum cavity. It was the heat-affected deformation zone that was covered by thermo-mechanically affected zone.

If the steel contained a zinc layer, this component had a significant influence on the strength, failure, and overall outcome of the joining procedure. During the tooling, the zinc followed the aluminum movement and it formed two buildups. One buildup was in the head region and the second was in the aluminum detachment area. In between these two areas, zinc from the protective layer diffused into aluminum and formed a brazed joint.

If the steel is the top work material, the joint design should be different, since the forces and heat generation are higher. The chance for aluminum degradation is higher because of higher temperature from the FSF of steel. The solution for the situation is a different design, the clinching design. In the situation where steel is the top work material, there could be intermetallic formation in the neck region.

7.1.3. 2D Model

At a 0.3 mm plunge depth, the aluminum went through the steel hole and touched the bottom of the anvil. At 0.6 mm, the formation of the mechanical interlocking was finished. At this depth, the aluminum detachment of the steel in the space between the tool and holder started to increase. The friction and the plastic deformation increased the temperature in the neck and in the flash. The generated heat was stored more in the side of the aluminum cavity, including the flash, than in the neck and head. Stress in the aluminum was more concentrated in areas where aluminum contacted other domains. Stress was highly distributed in aluminum along the contact surface with steel and the anvil. However, at the peak of the aluminum detachment, the stress value dropped and it diminished after the detachment.

As the tool increased the depth, the heat flux was directed more downwards, and less towards the side of the tool. This occurred because friction heating was the dominant way of heat generation, and it is caused by stirring from the bottom of the tool. The remaining aluminum under the tool at the higher depth experienced higher plastic deformation. The aluminum that was close to the tool was transformed into the thermo-mechanical zone, and the model results suggested that 1/3 of the original thickness of the aluminum was transformed in the thermo-mechanical zone.

7.1.4. 3D Model

There were significant differences between the 3D and the 2D model. First, there was a disagreement about the material progression and the temperature distribution throughout the joint. The 3D model showed that the aluminum progression towards the neck and the head was slower than was previously suggested by the 2D model.

The simulation was most likely to stop prematurely due to mesh distortion on the corner of the aluminum cavity or upper corner of the steel hole. The quality of the neck/head region was highly dependent on how the mesh behaves on the upper edge of the steel hole. This edge dictated the mesh characteristics such as size of the element, partition, distortion control, etc. The center of the topside of the aluminum developed an unrealistic cavity, and the "separation after contact" option could be applied. This option had a significant influence on the top center of the aluminum domain area above the neck. In the 2D model, the option worked correctly. However in the 3D model with the option, the cavity was eliminated. Nevertheless, the shape of the head and the neck suffered. The upper edge of the steel hole had significant influence on the aluminum displacement. The aluminum in the thermo-mechanically affected zone was easily displaced, and it moved in two different directions: towards the neck or away from the neck area. While the aluminum was flowing, the aluminum that was on the bottom side, especially closer to the steel hole, had the least displacement.

At a plunge depth of 0.35 mm, the aluminum detachment started. At 0.5 mm, the tool progressed enough so that the neck formation finished and the head formation started. The maximum temperature of the system during the stirring is in the neck region before the tool reaches a 0.45 mm depth. At this point, the temperature of the system is 95°C and the aluminum touches the bottom of the anvil cavity. After this point, the maximum temperature of the global model is on the rim of the aluminum cavity, and at 0.8 mm plunge depth the maximum temperature is 169°C. Since the steel is off-centered, the temperature was not equal around the circumference of the flash. If the steel were moved in one way, the opposite side of the flash would get slightly more heat. In addition, the aluminum did not have symmetric heat flux and temperature distribution through the neck and head region as well. The minimum temperature in the entire coin was always in the center. The coin temperature was not very different between the top and the bottom surfaces. The bottom material, steel, would experience significant stress in the area around the hole, especially the part that is not supported by the anvil. The area experienced a significant heat input as well. The stirring was a major heat input into the system, and the steel domain directly experienced heat right under the entire diameter of the tool. From the thermocouple test, one of the conclusions was that the temperature inside of the core is higher than on the edge of the core. Unfortunately, this was not an outcome of the 3D model.

7.1.5. Validation Experiments

In order to get more temperature information of the process an infrared camera was used. The model required additional confirmations. The experiment ran on a lower plunging speed than was entered into the model, which means the specimens experienced a higher heat generation. The slower plunge speed means that the tool had a longer stirring time, which created higher temperatures. Unfortunately, the infrared camera reported lower temperatures at the center of the aluminum than the model reported. The heat generation should be higher. From **Table 12** and from the depth test, the conclusion is that the 3D model is the closest temperature representation of the experimental results. There is a problem with the head and the neck development, and the model requires improvement.

7.2. Future work

The FEA investigation should continue finding the best joint geometry in terms of strength and toughness. It is easier and less expensive to try different geometries in lap shear strength testing in FEA than in the physical experiments. The end goal is a 3D model capable of predicting process forces, strain, stress, and temperature for different combinations of geometries of tools and different work materials. The FEA output is expected to give improved parameters within the work material that otherwise would be impossible to measure.

7.2.1. Modeling Improvements

The previous examination was done on the single pin design. The next step is to improve the design in order to maximize the strength of the joints. A bigger radius of the neck, different shapes of the head, and a bigger hole in the steel are just a few of the potential changes that can be explored in order to accomplish the task. This definitely can be further explored and accomplished in ABAQUS/Explicit. Besides the designs, other materials need to be explored as well. In that way, the model gives complete information of the chosen set of materials and the joint design.

Stick and slip values affect the heat generation and the mesh, and an adjustment of the values for a set of materials would increase accuracy of the heat generation. Another way to improve the model would be to increase the data about the thermal contact conductance.

7.2.2. Tensile test

The final model should also incorporate additional steps: lowering the temperature of the domains to the room temperature, and a lap shear test. For this, steel domain needs to be deformable and all the domains except for the tool need to be squared/rectangular. The lap shear test step requires decoupling contact pairs that are defining interactions between any rigid and non-rigid domains. In that way, the tool and anvil will stop having any influence on the steel and the aluminum. After the decoupling, a new set of boundary conditions has to be applied. One side of one of the domains needs to be fixed, while the opposite end of the other deformable domain needs to experience a certain feeding rate. In this way, the model can simulate a single lap shear test. These results could be easily verifiable by laboratory testing.

7.2.3. Clinching Model

If a material needs to substituted in a model with a different material, the process of changing the material requires just changing the values such as density, Young's Modulus, Poisson ratio, etc. This is a quick step that is followed with the computational stage. If a dimension needs to be changed, such as diameter of the steel hole, there is a simple and quick process of changing the dimension. This might affect other constraints such as diameter of the steel partition. After everything is aligned, the computer can start to perform the simulation task.

However, if the design needs to be drastically changed, then a new model has to be built. The clinching design is the next model that is in the development stage. At this time, all the knowledge that was gathered from the single pin design is fully transferrable to other designs, including the clinching design.

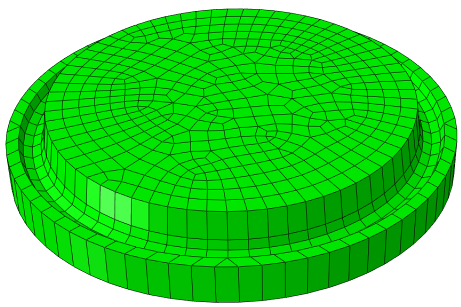

(a) Anvil

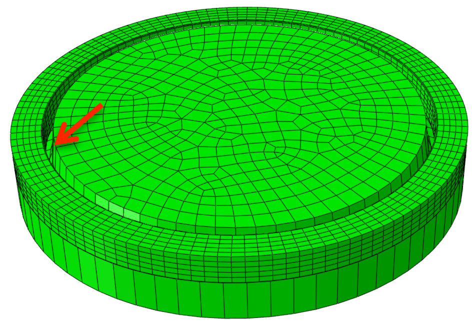

(b) Anvil and the bottom workpiece

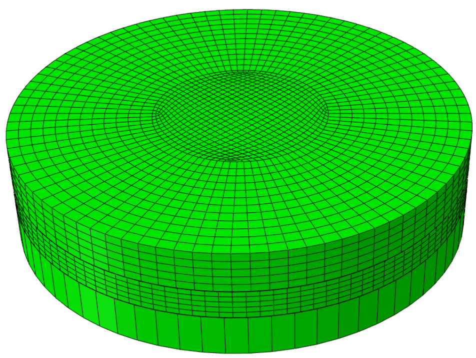

(c) Anvil and the two workpieces

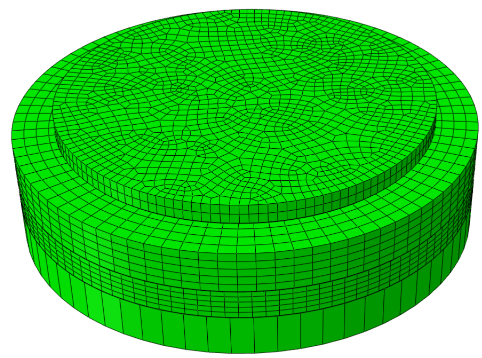

(d) the complete assembly

Figure 62: Clinching joint assembly

Figure 62 shows all the clinching domains and the assembly. The challenge for the model is that the space between the anvil pin and the bottom material is insufficient for the top material to properly progress through the gap, which is the neck of the clinch joint. The red arrow on **Figure 62** b) is highlighting the gap between the pin and the bottom workpiece. All the domains have the exact dimensions from the samples that were described in the previous sections. Because of the geometry of the joint, the plastic deformation of the top work material is greater than in the single pin joint, which represents an engaging challenge. The bottom work material is plastically deforming, and the deformation needs to be accurately represented. Looking forward, the contact between the top surface of the top workpiece and the bottom of the tool would not be a great challenge since the situation is the same as in the single pin 3D model. Contact pairs and boundary conditions are the same and completely transferable. There is an assumption that “separation after the contact” dilemma would not be present in the model because the middle of the joint is the anvil pin. After all, the only major challenge that is left to solve is how to have an appropriate mesh distortion control in the neck region. A higher mesh density would be one of a few possible factors that would improve the situation.

8. Contributions of this research

- FSF process was experimentally validated and that includes basic information for the design, the dimensions, and the materials of the tool, the bottom workpiece hole, the anvil, and the holder.
- The intermetallic compound, the zinc buildup, the aluminum detachment, and the brazing characterization were found in the zinc layer advancement.
- Aluminum progression during the FSF procedure was revealed. As the tool plunged, aluminum entered the steel hole, filled out the neck space, and continued in the same manner towards the bottom of the anvil cavity after exiting the steel hole. Once the aluminum made full contact with the anvil, it flowed horizontally to fill the rest of the cavity space. As the tooling progressed, the aluminum under the tool moved only away from the neck.
- Two-dimensional and three-dimensional models were established for FSF, which provided a deeper understanding of the FSF process. This incorporates appropriate mesh elements, mesh size and partitions, plasticity model, contact pairs, boundary conditions, distortion control, computational time cost, submodeling, and suggestions for transfer of the results between modeling steps, and modeling of brazed joint.
- The three-dimensional model and the submodels highlight the major obstacles, such as the mesh distortion on the corner of the aluminum cavity, the mesh distortion on the upper corner of the steel hole in the single pin model, or the mesh distortion in the narrow neck region in the clinching design. "Separation after the contact" is another fact that has a profound influence on the shape error.
- The temperature distribution in a single pin joint is clearer after the temperature tests and the models. The maximum temperature of the system during the stirring is in the neck region before the head is fully formed. After this point, the maximum temperature is on the rim of the aluminum cavity. Since the steel was off-centered, the temperature distribution was not symmetrical in the joint. If the steel were moved in one way, the opposite side of the joint would get slightly more heat. The bottom material experienced significant stress and heat input in the area around the hole.

9. Acknowledgment

We gratefully acknowledge the support for this work from General Motors Corporation, University of Hawaii at Manoa, and NSF CMMI grant # 1131845.

10. Works Cited

"Abaqus User's Guide 6.13." Dassault Systèmes Simulia Corp. Web. 17 Feb. 2015.

Awang, M., Mucino, V.H., Feng, Z., and David, S.A. "Thermo-Mechanical Modeling of Friction Stir Spot Welding (FSSW) Process: Use of an Explicit Adaptive Meshing Scheme." Technical Paper for the Society of Automotive Engineers 2005 World Congress, Detroit, MI. April 13, 2005.

Balakrishnan KN, Kang HT, Mallick PK. "Joining aluminum to nylon using frictional heat." In: SAE Tech. Paper 2007-01-1701, 2007.

Chen, C.M. and Kovacevic, R. "Joining of Al 6061 alloy to AISI 1018 Steel by Combined Effects of Fusion and Solid State Welding." International Journal of Machine Tools & Manufacture, 44 1205-1214, 2004.

Choi, D.H., Ahn, B.W., Yeon, Y.M., Park, S.C., Sato, Y.S., Kokawa, H., and Jung, S.B., "Microstructural characterizations following friction stir welding of dissimilar alloys of low-and high-carbon steels." Mater. Trans., 52(7), pp. 1500-1505, 2011.

Fazel-Najafabadi, M., Kashani-Bozorg, S.F., and Zarei-Hanzaki, A., "Dissimilar lap joining of 304 stainless steel to CP-Ti employing friction stir welding." Mater. and Des., 32(4), pp. 1824-1832, 2011.

Gök, K., Aydin, M., "Investigations of Friction Stir Welding Process Using Finite Element Method." The International Journal of Advanced Manufacturing Technology Vol. 68, pp. 775–780, 2013.

Hea, X., Gub, F., Ball, A., "A review of numerical analysis of friction stir Welding." Progress in Materials Science 65, 1-66, 2014.

Jaffarullah, M.S., Busu, N., Low, C.Y., Saedon, J.B., Armansyah, Shaari, M.S.B., Jaffar, A., "Finite Element Analysis of Stress-Strain Response at the Tool Pin During Friction Stir Process." Procedia Computer Science, Vol. 76, 522-527, 2015.

Jana, S., Mishra, R.S., Baumann, J.B., and Grant, G. "Effect of Friction Stir Processing on Fatigue Behavior of an Investment Cast Al-7Si-0.6 Mg alloy, Acta Materialia 58 989-1003, 2010.

"Johnson-Cook Plasticity." Abaqus Analysis User's Manual. N.p., Web. 3 Apr.

2015.

Kalpakjian, S. and Schmid, S.R. “Manufacturing Processes for Engineering Materials.” 5th ed., Pearson Education ,771, 2008.

Lazarevic, S., Miller, S.F., Li, J., and Carlson, B.E., “Experimental analysis of friction stir forming for dissimilar material joining application,” Journal of Manufacturing Processes, 15 616-624, 2013.

Lazarevic, S., Ogata, K.A., Miller, S.F., Kruger, G.H., and Carlson, B.E., “Formation and Structure of Work Material in the Friction Stir Forming Process.” Journal of Manufacturing Science and Engineering (In Press), 2015.

Martinsen, K., Hu, S.J., Carlson, B.E., “Joining of Dissimilar Materials.” CIRP Annals Manufacturing Technology, 64 pp. 679-699, 2015.

Miller, S. F., and Shih A. J., “Thermo-Mechanical Finite Element Modeling of the Friction Drilling Process.” J. Manuf. Sci. Eng. 129(3), 531-538,Jan 03, 2007.

Mori, K., Kato, T., Abe, Y., and Ravshanbek, Y., “Plastic Joining of Ultra High Strength Steel and Aluminum Alloy Sheets by Self Piercing Rivet.” Department of Production Systems Engineering, Toyohashi University of Technology, Toyohashi, Japan 2006

Mousavi, A. A. A., and Kelishami, A. R., “Experimental and Numerical Analysis of the Friction Welding Process for the 4340 Steel and Mild Steel Combinations.” American Welding Society, 29 Aug. 2008.

Murr, L.E., Li, Y., Trillo, E.A., and McClure, J.C. “Fundamental Issues and Industrial Applications of Friction-Stir Welding.” Mater. Tech. Adv. Perform. Mater. 15(1) 37–48, 2000.

Nishihara, T. “Development of friction stir forming.” Materials Science Forum 426–432:2971–8, 2003.

Park, K., Kim, B., and Ni, J., “Numerical Simulation of Plunge Force During the Plunge Phase of Friction Stir Welding and Ultrasonic Assisted FSW” N.p., Department of Mechanical Engineering, University of Michigan, Web, Oct.-Nov. 2008.

Pasic, O., Hajro, I., and Hodzic, D., “Welding of Dissimilar Metals – Status, Requirements and Trends of Development." Welding in the World 51(spec. iss) 377-384, 2007.

Prasanna, P., Rao, S., B., G. Rao, K. M., "Finite Element Modeling for Maximum Temperature in Friction Stir Welding and its Validation." The International Journal of Advanced Manufacturing Technology Vol. 51 pp. 925-933, 2010.

Seli, H. (2012) "Evaluation of Properties and FEM Model of the Friction Welded Mild Steel-Al6061-Alumina." SciELO Brasil, Web. 10 Feb. 2015.

Schmidt H., and Hattel, J., "A Local Model for the Thermomechanical Conditions in Friction Stir Welding." Modelling Simul. Mater. Sci. Eng. 13, 77–93, 2005.

Soundararajan, V., Zekovic, S., and Kovacevic, R., "Thermo-Mechanical Model with Adaptive Boundary Conditions for Friction Stir Welding of Al 6061." International Journal of Machine Tools & Manufacture 45,1577-1587, 2005.

Sun, Z. and Karppi, R. "The Application of Electron Beam Welding for the Joining of Dissimilar Metals: An Overview." Journal of Materials Processing Technology 59 257-267, 1996.

Sun, X. and Khaleel, M.A. "Dynamic Strength Evaluations for Self-Piercing Rivets and Resistance Spot Welds Joining Similar and Dissimilar Metals." International Journal of Impact Engineering 34 1668-1682, 2007.

Tanaka, T., Morishige, T., and Hirata, T. "Comprehensive analysis of joint strength for dissimilar friction stir welds of mild steel to aluminum alloys." Scripta Materialia 61 756-759, 2009.

Tanmoy, M., Roy, B.S., Debbarma, S., and Saha, S.C., "Thermal Modelling and Effect of Process Parameters in Friction Stir Welding." Elsevier Ltd, Web, 2015.

Veljić, D.M., Rakin, M.P., Perović, M.M., "Heat Generation During Plunge Stage in Friction Stir Welding." Thermal Science, 17, 489–496, 2013.

Watanabe, T., Takayama, H., Yanagisawa, A., and Konuma, S. "Observation of the Solid State Welded Interface Between Steel and Aluminum Alloy Using a Rotating Pin." Quarterly Journal of the Japan Welding Society 23(4) 603-607, 2005.